OPTICALLY TRIGGERED THYRISTOR FOR CAPACITOR DISCHARGE APPLICATIONS

A Thesis presented to

The Faculty of the Graduate School

University of Missouri-Columbia

In Partial Fulfillment

of the Requirements for the Degree

Master of Science

By

MANASA KOTHA

Dr. Robert M. O'Connell, Thesis Supervisor

DECEMBER 2007

The undersigned, appointed by the dean of the Graduate School, have examined the thesis entitled

OPTICALLY TRIGGERED THYRISTOR FOR CAPACITOR DISCHARGE APPLICATIONS

Presented by **Manasa Kotha**

A candidate for the degree of Master of Science

And hereby certify that, in their opinion, it is worthy of acceptance.

____

Professor Robert M. O'Connell, Dept. of Electrical and Computer Engineering

____

Professor William C. Nunnally, Dept. of Electrical and Computer Engineering

____

Assoc. Professor Yuyi Lin, Dept. of Mechanical and Aerospace Engineering

Dedicated to my parents

Kotha Raja Pratap and Radha Rani

ACKNOWLEDGEMENTS

I sincerely thank my advisor, Dr Robert O'Connell for his immense support and continuous guidance, invaluable suggestions and timely help throughout the duration of this work. His mentorship and help had a great impact on my life and made my past years a very special time.

I would like to thank my committee members, Dr. Bill Nunnally and Dr. Yuyi Lin for their time and consideration in reading my thesis and for their help in defining and completing my thesis.

I would like to thank Jim Fischer, Electrical Engineering Department for his immediate assistance in using the PSPICE remotely.

I acknowledge Armin and Akeed for helping me out on getting started with the Silvaco software. I would also thank my fellow students Brady Smith and Jessica for their help.

I would like to thank Shirley Holdmeier and Susan Wayt for always lending a helpful hand. I express my gratitude to the entire faculty and staff of Electrical Engineering Department, who cooperated a lot during my course of study at Mizzou.

Finally I take this opportunity to thank my friends and family for their love and support. I specially want to thank my sister Smitha , nephew Ajay and my parents for their encouragement, love and support.

TABLE OF CONTENTS

ACKNOWLEDGEMENTS .... **ii**

TABLE OF CONTENTS .... **iii**

LIST OF ILLUSTRATIONS .... **v**

LIST OF TABLES .... **xi**

CHAPTER 1

INTRODUCTION 1

CHAPTER 2

BACKGROUND 5

2.1 Thyristor Switch Basics 5

2.2 Characteristics of the Thyristor 6

2.3 Thyristor Types 9

2.4 Light-Triggered Thyristor 9

CHAPTER 3

DEVICE SIMULATION USING SILVACO ATLAS 17

3.1 About Silvaco 17

3.2 ATLAS 18

3.2.1 ATLAS Inputs and Outputs 19

3.2.2 Deckbuild 20

3.2.3 Devedit 21

3.2.4 Tonyplot 22

3.3 Basic Semiconductor Equations 22

3.4 PSPICE Simulations ... 28

3.4.1 Thyristor as a Switch ... 28

3.4.2 Thyristor in a Capacitor Discharge Circuit ... 31

CHAPTER 4

SILVACO SIMULATION RESULTS ... 37

4.1 Approach to Design ... 37

4.2 ATLAS approach in designing the opto-thyristor ... 41

4.2.1 Structure Specifications ... 41

4.2.2 Material Model Selection ... 44

4.2.3 Numerical Method and Solution Specification and Results analysis ... 45

4.3 Opto-thyristor Dark Current Analysis ... 46

4.4 Optothyristor Turn on Transient ... 55

4.5 Opto-Thyristor in a Capacitive Discharge Circuit ... 64

CHAPTER 5

SUMMARY, FUTURE WORK AND CONCLUSION ... 76

5.1 Summary ... 76

5.2 Future Work ... 77

5.3 Conclusion ... 78

APPENDIX ... 79

REFERENCES ... 82

LIST OF ILLUSTRATIONS

Figure 2.1 Basic Thyristor 6

Figure 2.2 Vertical Cross-section of the Thyristor 6

Figure 2.3 Thyristor Symbol.......... 6

Figure 2.4 I-V Characteristics of the thyristor 6

Figure 2.5 Opto-thyristor 10

Figure 2.6 Impurity concentration profile [8] 11

Figure 2.7 Top view of the opto-thyristor [8] 11

Figure 2.8 Typical off-state and reverse current-.......... 11

Figure 2.9 Typical turn-on waveform.V:500 V/div, I:500A/div t:2μs/div for the Figure 2.6 [8] 11

Figure 2.10 GaAs opto-thyristor structure[15] 12

Figure 2.11 Experimental setup to test the opto-thyristor shown in Figure 2.10 [15]...... 12

Figure 2.12 Typical I-V characteristics of GaAs opto-thyristor [15] 13

Figure 2.13 AlGaAs/GaAs opto-thyristor [10] 14

Figure 2.14 Experimental setup to test the device shown in the Figure 2.13 [10]........... 14

Figure 2.15 Switched-current waveforms with illumination on P side with 2120, 2020, 1940, 1840, 1850, 1780, 1600, 1400 and 950V 14

Figure 2.16 Switched-current waveforms with illumination on N side with 1940, 1850, 1780, 1600, 1400 and 1200V across the device shown in Figure 2.13 [10]............... 14

Figure 2.17 InP opto-thyristor structure[9] 15

Figure 2.18 Test Circuit for the device shown in... 15

Figure 2.19 Switched current as a function of Forward Voltage bias for the Figure 2.17[9] 15

Figure 2.20 di/dt as a function of voltage 15

Figure 3.1 ATLAS Inputs and Output [16].. 20

Figure 3.2 Schematic diagram for analysis of a thyristor as a switch............................. 28

Figure 3.5Thyristor in a capacitive discharge circuit.. 31

Figure 3.6 Circuit to find the resonant frequency 32

Figure 3.7 PSPICE frequency response of the circuit to determine the resonant frequency of the circuit 32

Figure 3.8 Capacitor current and voltage for the circuit shown in Figure 3.5. Initial capacitor voltage is 800 V.. 33

Figure 3.9 Capacitor current and voltage for the circuit shown in Figure 3.5. Initial capacitor voltage is 400 V 34

Figure 4.1 i) Electrically gated thyristor with amplifying gate 39

Figure 4.1 ii)Optically gated thyristor with amplifying gate 40

Figure 4.2 Structure of an opto-thyristor for simulation study 40

Figure 4.3 ATLAS Command Groups with man statements in each group 41

Figure 4.4 Simulation mesh of opto-thyristor 42

Figure 4.5 Structure showing the incidence of light 43

Figure 4.6 Forward characteristics of an Opto-thyristor with drift region concentration $1*10^{-14}$ cm $^{-3}$ and length 60µm 46

Figure 4.7 Reverse characteristics of an Opto-thyristor with drift region concentration $1*10^{-14}$ cm $^{-3}$ and length 60µm 47

Figure 4.8 Forward characteristics of an Opto-thyristor with drift region concentration $1*10^{-13}$ cm $^{-3}$ and length 60µm 48

Figure 4.9 Reverse characteristics of an Opto-thyristor with drift region concentration $1*10^{-13}$ cm $^{-3}$ and length 60µm 48

Figure 4.10 Forward characteristics of an Opto-thyristor with drift region concentration $1*10^{-15}$ cm $^{-3}$ and length 60µm 49

Figure 4.11 Reverse characteristics of an Opto-thyristor with drift region concentration $1*10^{-15}$ cm $^{-3}$ and length 60µm. 49

Figure 4.12 Forward characteristics of an Opto-thyristor with drift region concentration $1*10^{-13}$ cm^{-3} and length 120μm 50

Figure 4.13 Reverse characteristics of an Opto-thyristor with drift region concentration $1*10^{-13}$ cm^{-3} and length 120μm 51

Figure 4.14 Overlay of forward characteristics of an opto-thyristor with drift region concentrations $1*10^{-13}$ cm^{-3}, $1*10^{-14}$ cm^{-3}and $1*10^{-15}$ cm^{-3} and length 120 μm 52

Figure 4.15 Overlay of reverse characteristics of an Opto-thyristor with drift region concentrations $1*10^{-13}$ cm^{-3} , $1*10^{-14}$ cm^{-3}and $1*10^{-15}$ cm^{-3} and length 120 μm 52

Figure 4.16 Breakdown voltages of punch-through diodes and thyristors (dashed-line) 54

Figure 4.17 Optical Absorption depth vs Wavelength is Silicon........ 55

Figure 4.18 General test circuit for the simulation of turn-on transient for the opto-thyristor........ 56

Figure 4.19 Turn-on characteristics of the Model 1 optothyristor......... 57

Figure 4.20 Turn-on characteristics of the Model 2 optothyristor........ 58

Figure 4.21 Turn-on characteristics of the Model 3 optothyristor......... 58

Figure 4.22 Turn-on characteristics of the Model 4 optothyristor......... 59

Figure 4.23 Turn-on characteristics of the Model 5 opto-thyristor 60

Figure 4.24 Turn-on characteristics of the Model 6 opto-thyristor. 60

Figure 4.25 Turn-on characteristics of the Model 2 opto-thyristor with optical power intensities 9, 90, 900 Watts/cm^2........ 62

Figure 4.26 Effect of the on-state resistance on the device performance with respect to third dimension (Model 2) 63

Figure 4.27 Opto-thyristor in capacitive discharge circuit 64

Figure 4.28 Opto-thyristor (Model 2) in capacitive discharge circuit 65

Figure 4.29 Opto-thyristor (Model 5) in capacitor discharge circuit 66

Figure 4.30 Performance of capacitor discharge circuit with initial conditions of 50 V, 100 V, 150 V, 200 V and 250 V on the capacitor (Model 2 opto-thyristor) 66

Figure 4.31 Capacitor current variations in Model 2 opto-thyristor whose width=3.03mm 67

Figure 4.32 Capacitor current variations with inductance in Model 2 opto-thyristor, whose width = 3.03mm 68

Figure 4.33 Effect of resistance in the capacitior discharge circuit (Model2) 69

Figure 4.34 Model 2 opto-thyristor with width=3.03 mm 70

Figure 4.35 Figure 4.34 magnified to observe the ringing 70

Figure 4.36 Capacitor current and Anode voltage for Model 5 opto-thyristor. 71

Figure 4.37 Performance of capacitor discharge circuit with initial conditions of 150 V, 200 V and 250 V on the capacitor (Model 2 opto-thyristor with width 3.03 mm) 72

Figure 4.38 Circuit Current for Model 2 opto-thyristor whose width is 520 µm in a capacitive discharge circuit 73

Figure 4.39 Circuit Current for Model 5 opto-thyristor whose width is 520 μm in a capacitive discharge circuit 74

Figure 4.40 Circuit Current for Model 2 opto-thyristor whose width is 3.03 mm in a capacitive discharge circuit 75

Figure 4.41 Circuit Current for Model 5 opto-thyristor whose width is 3.03 mm in a capacitive discharge circuit 75

LIST OF TABLES

Table 4-1 Breakover voltages of the different opto-thyristors.. 53

Table 4-2 Breakdown voltages of the different opto-thyristors....................................... 53

Table 4-3 Theoritical values of Break down Voltages of the Si- thyristors 53

Table 4-4 On-state resistance of the all the device models.. 61

Table 4-5 Variations of on-state resistances with respect to width (Model 2) 63

CHAPTER 1: INTRODUCTION

The Army Research Laboratory has contributed to the development of a number of large area solid state switches for pulse power applications, including electric guns, high power microwaves, and laser modulators. An early publication [1] described a switch consisting of seven gate turn-off thyristors (GTO), that was capable of closing a 5 kV source at several hundred A peak current. The current turn-on rate was in excess of 200 A/µsec. A 1991 publication [2] presented the results of measurements on five commercially available thyristors for pulsed power applications. All five devices could block at least 2.0 kV and conduct at least 50 kA, with current turn-on rates ranging from 500 to1.4 kA/µsec. In 2000 ARL published articles on two novel thyristors with structural features specifically designed to speed up the spread of the plasma at the forward-biased gate-cathode junction, which is the critical element in determining a device's turn-on di/dt value. The first device, an asymmetric thyristor called the reverse-switching dynistor (RSD) [3], could block up to 3.5 kV, conduct up to 250 kA, and turn on at the rate of 2.8 kA/µsec. The second device was a symmetric thyristor with an involute gate [4]. It could block 2.4 kV, conduct 221 kA, and turn on at 2.0 kA/µsec. In another publication a High Current Thyristor has been designed for closing switch applications. This device has been optimized for low turn-on losses, high forward

blocking voltages and high di/dt. This device was able to block voltages upto 4500V, conduct 150 kA and turn on at 20 kA/ μsec [5].

The use of optical triggering in thyristors has been of interest since the 1970s, primarily to provide low jitter electrical isolation of gate drive circuits in high voltage DC (HVDC) transmission [6]. Probably the first attempt to improve thyristor di/dt ratings was an EPRI-sponsored investigation in 1981 of the physical differences between electrically-triggered and optically-triggered thyristor turn-on [7]. The study showed that in optical triggering there is an additional component of current that allows the anode junction to inject carriers earlier than in the case of conventional, electrical triggering. This led to devices with di/dt ratings close to 800 A/μsec. In 1990, the Fuji Electric Corporation reported the development of an improved light-triggered thyristor for application in high-power converters such as the static var compensator in the electric power industry [8]. The new device was manufactured using implanted aluminum and phosphorus ions to improve doping uniformity, resulting in a thyristor with voltage, current, and di/dt ratings of 6.0 kV, 2.5 kA, and 300 A/μsec, respectively.

Improvements in thyristor di/dt ratings into the kA/μsec range came with the need for switching devices for pulsed-power applications. In 1994, researchers at Rutgers University reported the development of optically-gated thyristors, which they called optothyristors, based on InP and GaAs [9], [10]. Both device structures featured large semi-insulating layers of either InP or GaAs between the basic p-n junctions constituting the thyristor structure to provide large blocking voltages. The maximum voltage, current, and di/dt values of the new devices were 1200 V, 61 A, and 14 kA/μsec, respectively, for the InP-based structure, and 2120 V, 156 A, and 8.5 kA/μsec, respectively, for the GaAs-

based structure. Those devices represented an order of magnitude increase in di/dt capability, but at the expense of the reduction of their current ratings by approximately the same factor. In 2004, OptiSwitch Technology Corporation demonstrated a coupling technique to activate a large area thyristor (3 inch diameter) with a minimum number of fiber optics. Their results included a 6 kV thyristor that can switch 111 kA with an 85 kA/μsec di/dt[11].

The most recent developments in optically-triggered thyristors have been for application in electric gun systems, which use a capacitive discharge circuit. [12], [13]. These reports, by researchers in Germany, describe switches with 10s of kV blocking voltage capability and 10s of kA current carrying capability, but only 10 kA/μsec di/dt ratings.

All of the devices discussed thus far have been large single devices, sometimes referred to as hockey puck structures. The latest development in thyristor technology, the MOS-controlled thyristor, or MCT [14], is different. In applications which require very high turn on about 110 kA/ μsec, an MCT is preferred.

The purpose of this project was to use simulation tools to investigate improvements to optically triggered thyristors for capacitor discharge applications. Chapter Two describes the background of the thyristors, including operational principles and basic terms that are used for these devices. Research that was previously conducted in light-triggered thyristors was also discussed. Chapter Three gives the details of the SILVACO software tool which was used for modeling the opto-thyristor. Also, PSPICE simulation results of a standard thyristor in the capacitor discharge circuit are discussed. Chapter Four discusses the details of the approach to modeling an opto-thyristor using

Silvaco ATLAS, and includes the results of simulation of the resistive and capacitive discharge circuit. Chapter Five gives the summary, conclusion and suggestions for future work.

CHAPTER 2: BACKGROUND

Optically triggered power semiconductor devices are used for high power applications which requires high di/dt, current and voltage ratings. The thyristor is one of the power semiconductor devices which have the capability to meet these requirements. The thyristor is used as a switch in a capacitive discharge circuit, whereby upon triggering the thyristor closes the circuit thus enabling the discharge of the voltage stored in the capacitor through the thyristor switch. These are used in many power applications such as rail guns, electric guns, coil guns and electromagnetic launchers. This chapter provides the basics of the thyristor and the reason for using this for the capacitive discharge application.

2.1 Thyristor Switch Basics

A thyristor is a basic four-layered solid-state semiconductor structure with alternating p-n layers as shown in the Figure 2.1 the vertical cross section of the thyristor is as shown in Figure 2.2.and its symbolic representation is as shown in Figure 2.3.

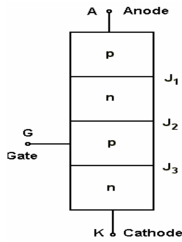

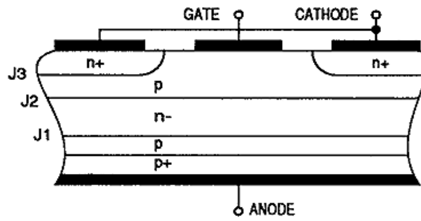

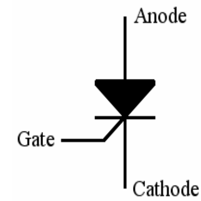

Figure 2.1
Basic thyristor

Figure 2.2
Vertical cross section of thyristor

Figure 2.3
Thyristor symbol

The output circuit terminals are the anode and cathode and the p-type layer which is near the cathode is the control terminal, called the gate.

2.2 Characteristics of the Thyristor

The uniqueness of the thyristor lies in its current and voltage characteristics as shown in Figure 2.4.

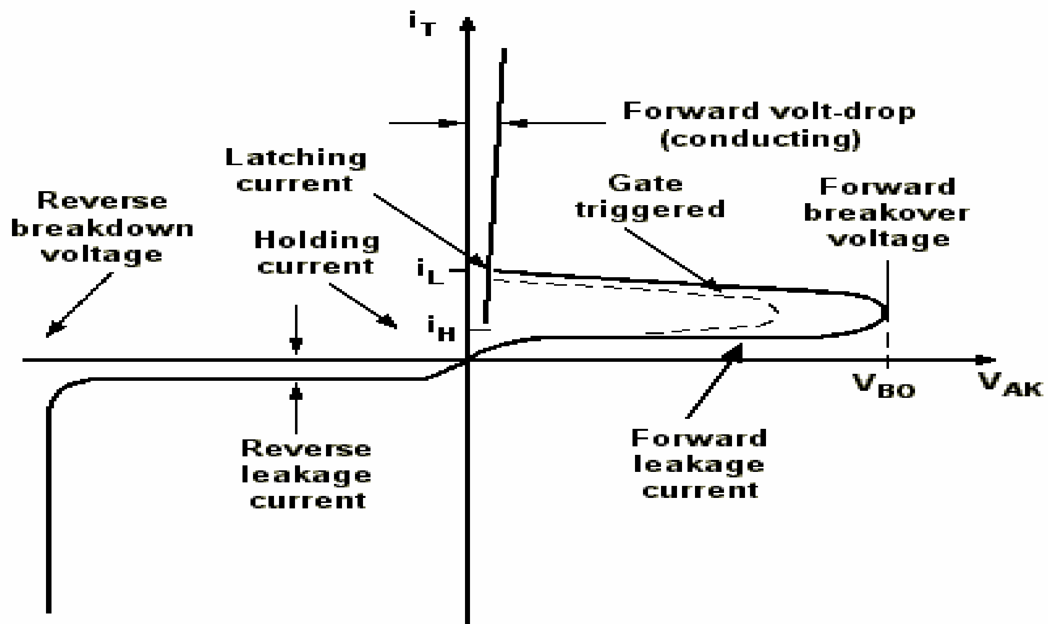

Figure 2.4 I-V Characteristics of the thyristor

On applying a positive voltage across the anode with respect to the cathode, junctions J1 and J3 are forward biased and junction J2 is reverse biased and the thyristor is said to be in the forward blocking state. On further increase of the applied forward voltage the device would turn-on via pnpn regenerative transistor action. This is called the forward breakover voltage V_{BO} and the device is now said to be in forward conducting state or on-state. On applying a negative voltage to the anode with respect to cathode, the device characteristics are similar to the reverse bias characteristics of the PIN diode.

Some important points on the thyristor characteristic shown in Figure 2.4 are as follows:

- Latching Current $\mathbf{I}_{L:}$ The minimum anode current required to maintain the thyristor in the on-state immediately after the thyristor has been turned on and the gate signal has been removed.
- Holding Current $\mathbf{I}_H$: This is the minimum anode current required to maintain the thyristor in the on-state. To turn off a thyristor, the forward anode current must be reduced below its holding current for a sufficient time for mobile charge carriers to vacate the junction. If the anode current is not maintained below $\mathbf{I}_H$ for long enough, the thyristor will not have returned to the fully blocking state by the time the anode-to-cathode voltage rises again. It might then return to the conducting state without an externally-applied gate current.
- Reverse Current $\mathbf{I}_R$: When the cathode voltage is positive with respect to the anode, the junction $\mathbf{J}_2$ is forward biased but junctions $\mathbf{J}_1$ and $\mathbf{J}_3$ are reverse biased. The thyristor is said to be in the reverse blocking state and a reverse leakage current known as reverse current $\mathbf{I}_R$ will flow through the device.

- Forward Breakover Voltage $\mathbf{V}_{BO}$: If the forward voltage $\mathbf{V}_{AK}$ is increased beyond $\mathbf{V}_{BO}$, the thyristor can be turned on. But such a turn-on could be destructive. In practice the forward voltage is maintained below $\mathbf{V}_{BO}$ and the thyristor is turned on by applying a positive gate signal between gate and cathode.
- Reverse Breakdown Voltage $\mathbf{V}_{BD}$: The maximum reverse bias voltage that can be applied to the thyristor is limited by breakdown. Breakdown is characterized by the rapid increase of the current under reverse bias. The corresponding applied voltage is referred to as V_{BD}.

Function of the gate terminal

When the anode is at a positive potential V_{AK} with respect to the cathode with no voltage applied at the gate, junctions J_1 and J_3 are forward biased, while junction J_2 is reverse biased. As J_2 is reverse biased, no conduction takes place (Off state). Now if V_{AK} is increased beyond the breakover voltage V_{BO} of the thyristor, the thyristor then starts conducting (On state). At this stage if we apply a positive potential V_G at the gate terminal with respect to the cathode, the breakover occurs at a lower value of V_{AK}.
By selecting an appropriate value of V_G, the thyristor can be switched into the on-state immediately.

It must be noted that V_G need not be maintained after the device turn-on has occurred. Hence V_G can be voltage pulse, such as the voltage output from a UJT relaxation oscillator.

These gate pulses are characterized in terms of gate trigger voltage (V_{GT}) and gate trigger current (I_{GT}). Gate trigger current varies inversely with gate pulse width in such a way that it is evident that there is a minimum gate charge required to trigger the thyristor.

2.3 Thyristor Types

Many variations on the thyristor structure have been developed in an attempt to match the characteristics of the device to the demands of the different applications. Some of them are the Phase-Control Thyristor which is designed for power frequency applications; the Gate Turn off Thyristor (GTO) , where in typically used in high power applications for voltages over 2500 V and current over 400 A, where the current and voltage handling capabilities of other devices are insufficient to satisfy the requirements; the Asymmetric thyristor; the Gate-Assisted Turn-Off Thyristor; the Triac; the Light-Triggered Thyristor .The Light-Triggered thyristor is of interest in this project.

2.4 Light-Triggered Thyristor

Light-Triggered thyristors, sometimes called opto-thyristors or photo-thyristors, are four-layer structures of the thyristor type specially designed to be triggered by the optical generation of excess carriers.

When a piece of semiconductor is illuminated by light whose photon energy is greater than the band gap energy ($h\upsilon > E_g$) optical generation of electron-hole pairs occurs. Light so incident is absorbed in the P_2 layer of the thyristor (as in a conventional thyristor) in a blocking state, generates electrons that are collected by the space charge region of junction J_2 and transported into layer N_1 as shown in the Figure 2.5. This leads to the injection of excess holes into N_1 from the layer P_1. The effect of the optical carrier generation is similar to that of the electron injection from the n^+ emitter following the application of a positive gate voltage. If enough carriers are generated, the condition for turn-on is fulfilled and the thyristor turns on through the normal positive feedback

mechanism.

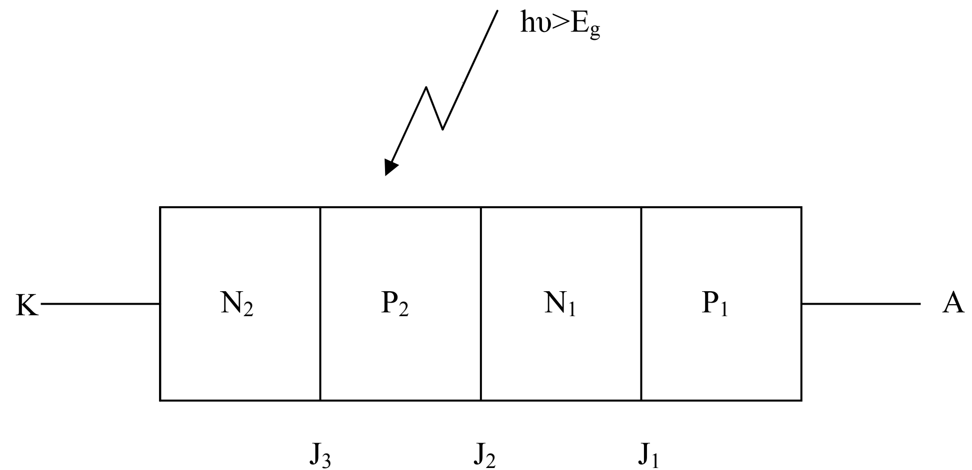

Figure 2.5 Opto-thyristor

The basic problem of the construction of the light-triggered thyristors is solving the contradictory requirements of the thyristor structure. It is necessary to obtain satisfactory turn-on with a reasonably low optical power; on the other hand, high values of the parameters (dv/dt) and (di/dt) are required. The structure and layout of the optical gate region is very important in determining these parameters.

Optical triggering is desirable in high voltage applications, especially where several thyristors are connected in series and the insulation of gate and anode circuits is required to be higher than 10kV.

In 1990, a 115-mm 6-KV 2500A opto-thyristor was developed for high power applications such as static var compensator (SVC) as shown in Figure 2.6 and Figure 2.7 [8]. The design developed included techniques such as aluminium and phosphorous ion implantation technique to form a uniform p-n-p-n four-layer structure; wafer and element treatment techniques such as alloying and packaging; and a design technique for a light–sensitive area structure and amplifying gate pattern .

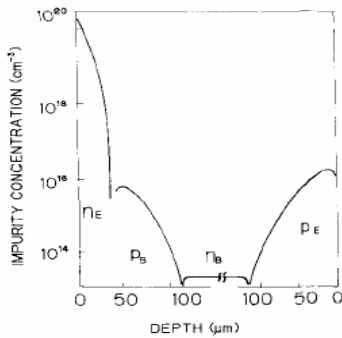

Figure 2.6 Impurity concentration profile [8]

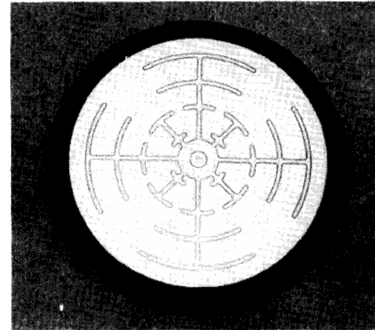

Figure 2.7 Top view of the opto-thyristor [8]

This silicon opto-thyristor had a blocking voltage 6 KV (Figure 2.8), on-state current of 2500A, di/dt more than 300 A/μs (Figure 2.9), minimum light-triggering power of 10mW.

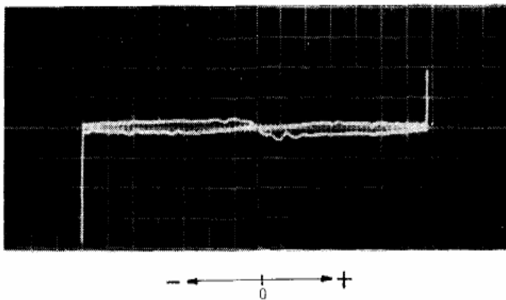

Figure 2.8 Typical off-state and reverse current-voltage characterstic.V:1KV/div;I:10mA/div for the Figure 2.6 [8]

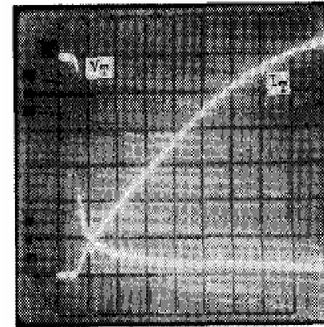

Figure 2.9 Typical turn-on waveform.V:500 V/div, I:500A/div t:2μs/div for the Figure 2.6 [8]

Later devices were developed with an idea to increase the di/dt of the device. Fast rise and fall times and high power are possible with GaAs and InP because these are direct band gap materials which have high resistivity. These materials are readily available in semi-insulating form and have been considered for use in opto-thyristors.

GaAs based opto-thyristors were designed with the intention to increase the di/dt rating so that these thyristors could replace the gas phase switches in high pulsed power

lasers and accelerators [15]. The device is fabricated using the Metal Organic Chemical Vapor Deposition (MOCVD) technique. Cr-doped semi-insulating GaAs was used as a substrate and on either side the $P^{+}N$ and $P\ N^{+}$ layers were grown as shown in the Figure 2.10. An AlGaAs laser diode with peak lasing wavelength of 848 nm was used as an optical triggering source for the thyristor. A laser pulse energy of 1-2 μJ with a pulse width of 100 nsec was used. The experimental set up to test the GaAs opto-thyristor in pulsed mode is as shown in Figure 2.11

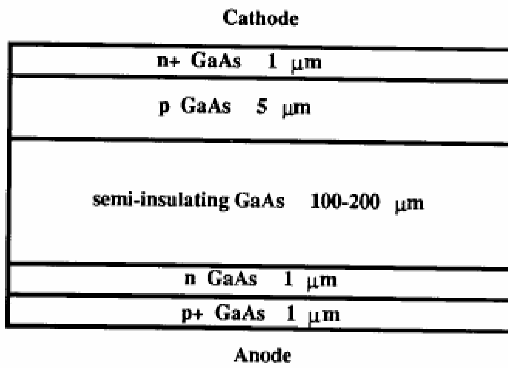

Figure 2.10 GaAs opto-thyristor structure[15]

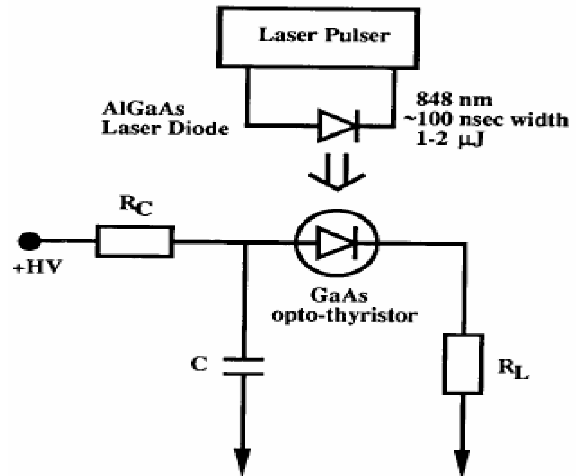

Figure 2.11 Experimental setup to test the opto-thyristor shown in Figure 2.10 [15]

The device was able to block voltages greater than 600 V and conduct a peak current greater than 70 A with turn-on di/dt of 14 kA/μs. The current rise time was less than 50 ns. However, the device had a forward voltage drop of 100 V, which is determined by the lock-on effect occurring in the thick base region of the device. An etchant-treated device was able to block voltages greater than 800 V, as shown in Figure 2.12. The edge breakdown was noticed as the limiting factor for blocking voltages and device lifetime.

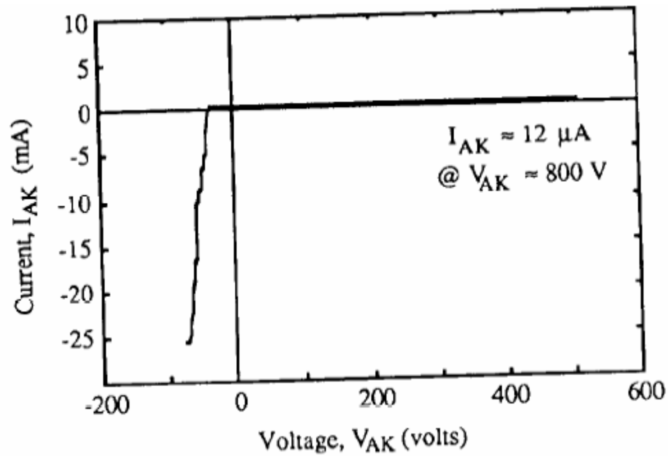

Figure 2.12 Typical I-V characteristics of GaAs opto-thyristor [15]

A novel high power opto-thyristor based on AlGaAs/GaAs has been designed so that it can be triggered with a light pulse energy as low as 0.1 μJ [10], which was not the case for GaAs homojunctions opto-thyristor. Taking advantage of the wider band gap AlGaAs material, which serves as an optical window, makes it possible to trigger with low pulse energy. The fabrication of the device was carried out using undoped LEC grown SI-GaAs as a starting material, on which P^+N and PN^+ AlGaAs layers were grown by MBE. Two circular recessed ohmic contacts were made on either side of the device with an optical aperture as shown in the Figure 2.13. A GaAs Laser diode operated in the mW range was used as a triggering source. The measurements on the device were carried on using the experimental set up as shown in the Figure 2.14.

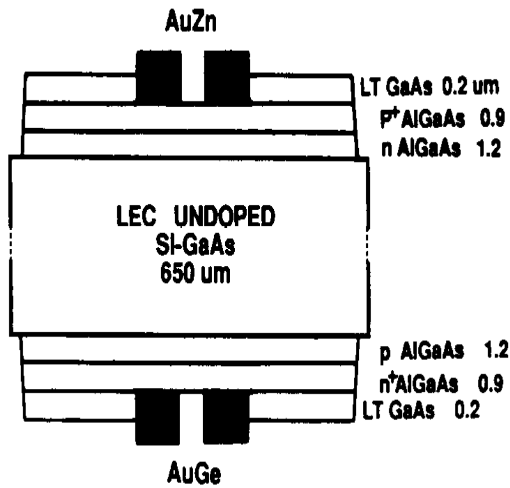

Figure 2.13 AlGaAs/GaAs opto-thyristor [10]

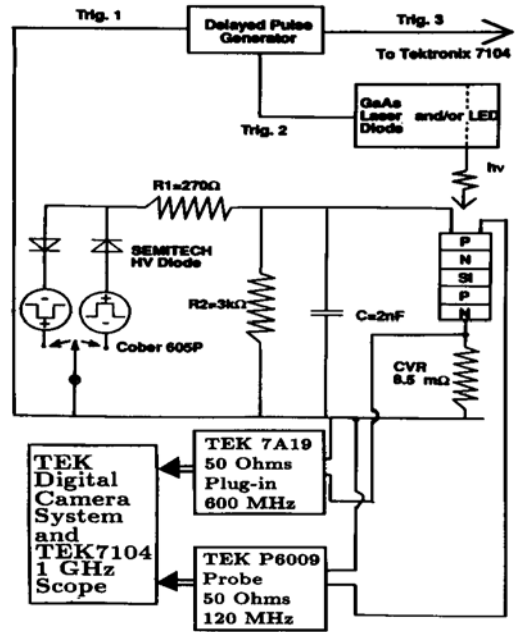

Figure 2.14 Experimental setup to test the device shown in the Figure 2.13 [10]

The device had a breakover voltage of about 2120 V and the di/dt rating was 8.5 kA/μs. The triggering was done separately from both sides of the device and the peak currents varied as shown in Figure 2.15 and Figure 2.16.

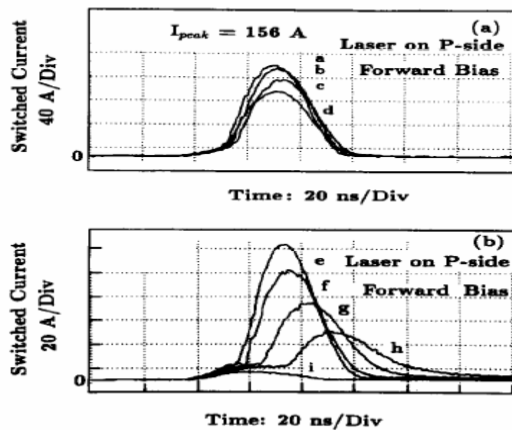

Figure 2.15 Switched-current waveforms with illumination on P side with 2120, 2020, 1940, 1840, 1850, 1780, 1600, 1400 and 950V across the device shown in Figure 2.13 [10]

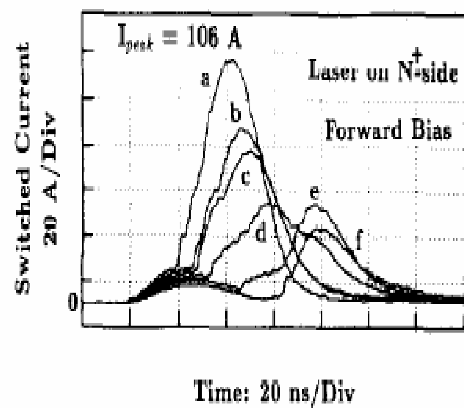

Figure 2.16 Switched-current waveforms with illumination on N side with 1940, 1850, 1780, 1600, 1400 and 1200V across the device shown in Figure 2.13 [10]

In 1994, an InP Based opto-thyristor was designed using the Liquid Phase Epitaxy (LPE) technique [9]. PN-NP InP layers were grown on either side on iron doped semi-insulating InP substrate, thus making a five layer device as shown in Figure 2.17. A 1.064 μm Nd. YAG laser was used to trigger the device. Figure 2.18 shows the circuit used for testing the characteristics of that device.

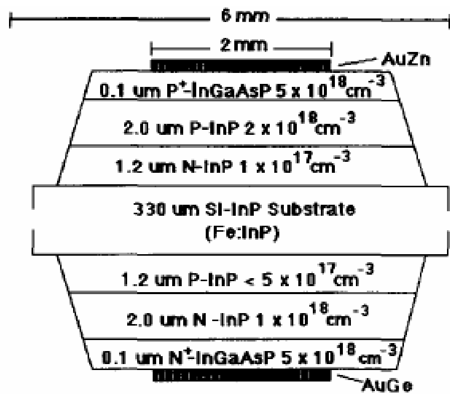

Figure 2.17 InP opto-thyristor structure[9]

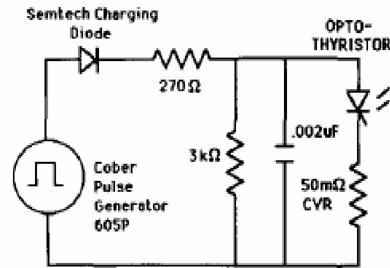

Figure 2.18 Test Circuit for the device shown in Figure 2.17 [9]

The device had a forward blocking voltage at 1400 V. The maximum turn-on current reached 61 A at 1200 V bias, with di/dt of 14 kA/μsec. The turn-on time has been improved and is less than 12 ns and the turn-off time is less than 20 ns. The minimum on-state resistance was found to be around 10-16 ohms. Refer to Figure 2.19 and Figure 2.20

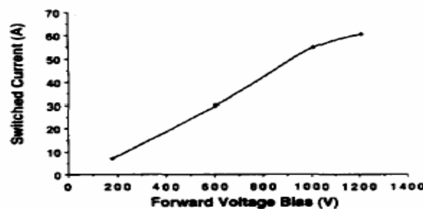

Figure 2.19 Switched current as a function of Forward Voltage bias for the Figure 2.17[9]

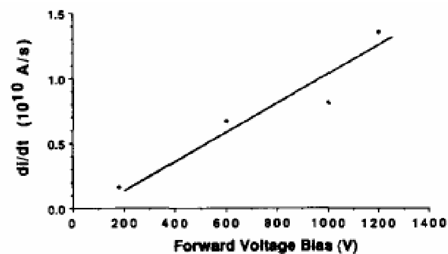

Figure 2.20 di/dt as a function of voltage for the Figure 2.17[9]

After a study through the different opto-thyristors designed using different materials, in view of improving the various parameters like di/dt, peak current or blocking voltages, this project considered to improve the di/dt characteristics in Si opto-thyristor [10].In spite of the advantages of the Compound semiconductor material silicon still has its advantages over them .It is the most abundant material found on earth's crust and cheap to process. Its greater physical strength enables to build larger wafers.

CHAPTER 3: DEVICE SIMULATION USING SILVACO ATLAS

The thesis considers modeling of a silicon four layered opto-thyristor. This device is then placed in a capacitive discharge circuit to simulate the device performance and ratings. All along, the simulations are carried out using Silvaco Atlas. This chapter briefly discusses the simulation tool.

3.1 About Silvaco

Silvaco (Silicon Valley Corporation) enables one to design and predict the performance of semiconductor devices based on physics-based simulation. This tool is helpful in modeling the semiconductor device initially before fabricating it. This is very helpful in many research and development projects. Silvaco, a leading company in the TCAD (Computer Aided Design) products, has included new physical models which use efficient numerical methods and algorithms, new meshing techniques, optimized linear solvers, etc., which helps in getting the simulation results very close to the practical results. TCAD products are used either for:

- Process simulations which use tools like ATHENA, SSupreme4 etc.

- Device Simulations which use the Atlas Framework. Atlas has several simulators like S-Pisces, Luminous, Mixed Mode, TFT, Laser, Blaze etc.
- Virtual Wafer Fab to automate and emulate physical wafer manufacturing.

In this project the Device Simulation is carried out using the ATLAS simulators.

3.2 ATLAS

ATLAS is a physically-based two and three dimensional device simulator. It predicts the electrical behavior of different semiconductor structures, and gives insight into the internal physical mechanisms associated with the device operation. ATLAS is a standalone tool for predicting the impact of process variables on circuit performance. Device simulation fits between process simulation and SPICE model extraction.

ATLAS enables one to choose from the large selection of silicon, III-V, II-VI, IV-VI or polymer/ organic technologies including, CMOS, bipolar, high voltage power device, VCSEL, TFT, optoelectronic, LASER, LED, CCD, sensor, fuse, NVM, ferro-electric, SOI, Fin-FET, HEMT and HBT. Different simulators are used for simulating the above mentioned. S-Pisces is a 2D device simulator for silicon based technologies that has both drift-diffusion and energy balance transport equations. Large selections of physical models are available for DC, AC and time domain simulation. Typical applications include MOS, bipolar and BiCMOS technologies. BLAZE simulates III-V, II-VI materials, and hetero-junction structures. It has built-in models for simulating abrupt and graded hetero-junctions for structures like MESFET, HEMT and HBT. GIGA allows simulation of local thermal effects in the devices. Device3D is a 3D program for simulating the DC, AC and time domain characteristics of silicon and advanced materials

based technologies. MIXED MODE 2D/3D is used to simulate the circuits that contain semiconductor devices for which accurate compact models do not exist. Some of the applications include the power circuits that include diodes, power transistors, IGBT's, GTO's, optoelectronic circuits, and many more. QUANTUM with its models simulates the effects of quantum confinement of carriers in semiconductor devices. TFT 2D/3D with its advanced physical models and numerical techniques simulates amorphous and polysilicon devices, including thin film transistors. LUMINOUS 2D/3D is used to simulate light absorption and photo-generation in semiconductor devices. Luminous, when used with the S-Pisces or Blaze device simulators, calculates the optical intensity within the semiconductor device and converts these profiles into photo-generation rates in the device simulator. This coupling feature helps in simulating the electronic responses to optical signals for a wide range of optoelectronic devices. LED simulates light emitting devices to predict their response with various parameters. It works in conjunction with other ATLAS simulators. LASER is used for simulating semiconductor laser diodes. The other simulators include VCSEL, OTFT, FERRO and NOISE for simulating vertical cavity surface emitting lasers, organic and polymer based devices, static I-V characteristics of ferroelectric films, and accurate characterization of small-signal noise sources, respectively.

3.2.1 ATLAS Inputs and Outputs

Figure 3.1 shows the flow of information to and from the ALTAS simulator.

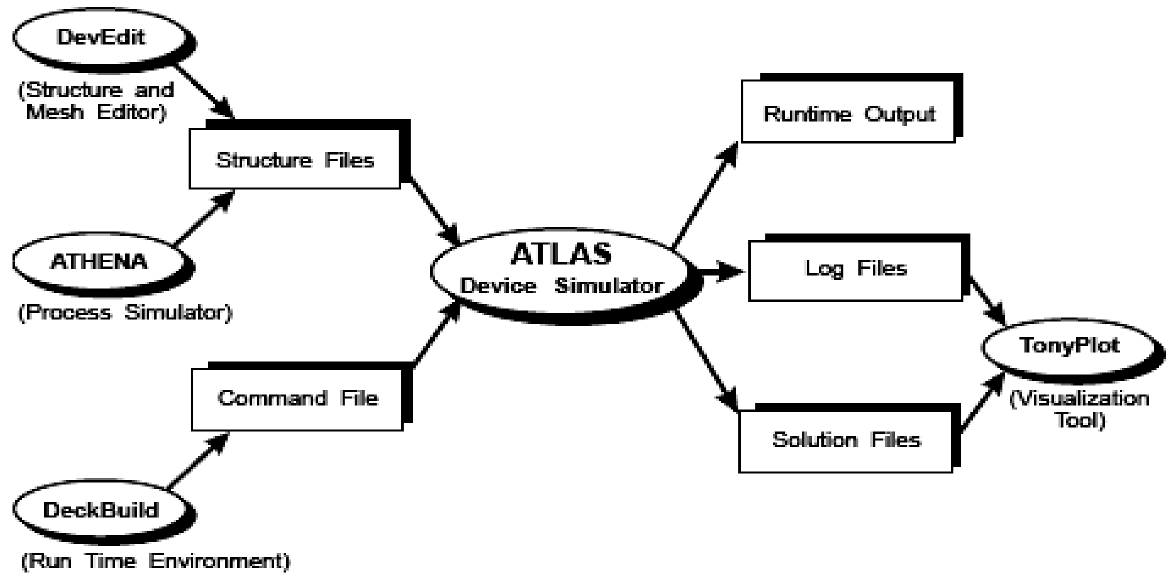

Figure 3.1 ATLAS Inputs and Output [16]

Simulations generally use two inputs which are: a text file that has commands for ATLAS to execute and a structure file that defines the structure of the device. The text file with simulator-specific commands is created with DECKBUILD. Structure files are created with DEVEDIT and ATHENA. ATLAS has three types of output. The progress of the simulation and error or warning messages are called the run-time output. Log files are generated with the currents and terminal voltages applied during device analysis. Finally the solution files store the two and three dimensional data relating to the values of solution variables within the device for a single bias point. The log files and the solution files are visualized using TONYPLOT.

3.2.2 Deckbuild

Deckbuild is a powerful interactive run-time environment tool that allows user to transparently go from process simulation to device simulation to spice model extraction.

It is easy to use run time environment for running core simulators such as ATLAS. Deckbuild helps in creating the input files to ATLAS. Multiple windows provide menu-based or text-based input decks for the information entered. The deck can be modified any time. Multiple decks are also created if there is any information that is being repeated. Mulitple simulators can be called from the input deck, and the transfer of information is transparent to the user. It offers complete control of run, kill, pause, and stop-at, restart, single-step and history initialization operation, i.e., we can back-track to a previous point in the deck and run it from that instance. It also includes a large number of examples for all types of technologies. In simulation it displays runtime output with the errors or warnings and the progress of the simulations. Necessary changes can be made to the input deck according to the run time output. Besides using the interactive mode, one can also give simulator-specific statements. The code also has a provision to incorporate the user-defined functions from the C-interpreter. Other simulator tools, such as TONYPLOT, DEVEDIT and MASKVIEW can also be invoked from Deckbuild. Deckbuild's optimizer helps in optimizing targets like structural dimensions and device parameters after complicated electrical tests and intermediate outputs.

3.2.3 Devedit

Devedit is an interactive tool for defining and altering structures. It uses SILVACO's Master structure file format to communicate with process and device simulators. Analytic functions in Devedit are helpful in defining and altering the doping profiles. It could be a stand-alone for defining structures and later invoked by Deckbuild to perform ATLAS simulation of the device structure. This tool is valuable as a pre-

processor for 2D device simulators. A new mode of DEVEDIT supports the definition and meshing of 3D structures.

3.2.4 Tonyplot

This is the common visualization tool in Silvaco TCAD products. It provides comprehensive capabilities for viewing and analyzing simulator output. The data can be plotted as desired by the user either in 1D x-y data, 2D contour data, Smith charts or polar charts. Measured data can also be imported and plotted in the above-mentioned types. The overlays feature helps in comparing the multiple simulation runs. It annotates plots to create meaningful figures for reports and presentations. It can plot to files, postscript printers, and other printer formats in sharp colors. It enables 2D structure plots to be cut by multiple, independently controlled 1D slices. Tonyplot includes animation features that permit viewing a sequence of plots in a manner showing solutions as a function of some parameter. The parameter can be varied under slider control, or frames can be looped continuously, a feature that is very helpful in developing physical insight. It allows IV (current-voltage) data or 1D plots to be over-layed to examine how process conditions affect electrical results. It supports plotting of user-defined equations with the variables being either electrical data, e.g., drain current, or physical parameters, e.g., electric field.

3.3 Basic Semiconductor Equations

Semiconductor equations are solved by the ATLAS simulator for the analysis of device performance. These equations, which are solved by any general purpose device simulator, have been derived from Maxwell's laws and consist of Poisson's equation, the

continuity equations, and the transport equations. The Poisson's equation relates variations in electrostatic potential to local charge densities and the continuity and transport equations describe the electron and hole densities which evolve as a result of transport processes, generation processes and recombination processes. The basic equations that provide the general framework for the charge transport are discussed next.

Poisson's Equation

Poisson's Equation relates the electrostatic potential to the space charge density

$$div\,(\varepsilon \nabla \psi) = -\rho \qquad (3.1)$$

Carrier Continuity Equations

The continuity equations for electrons and holes are defined as:

$$\frac{\partial n}{\partial t} n = \frac{1}{q}\, div \vec{J}_n + G_n - R_n \qquad (3.2)$$

$$\frac{\partial p}{\partial t} = \frac{1}{q}\, div \vec{J}_p + G_p - R_p \qquad (3.3)$$

where

q = magnitude of the charge on an electron

n and p = electron and hole concentrations, respectively

J_n and J_p = electron and hole current densities, respectively

G_n and G_p = Generation rate of electron and holes, respectively

R_n and R_p = Recombination rates for electrons and holes, respectively

The Transport Equations

Equations 3.1, 3.2 and 3.3 provide the general framework for device simulation. In addition, secondary equations are needed to specify particular physical models for J_n, J_p, G_n, R_n, G_p and R_p. The current density equations, or charge transport models, are usually obtained by applying approximations and simplifications to the Boltzmann Transport Equation. Different transport models such as the drift-diffusion model, the energy balance model, or the hydrodynamic model have been developed due to these assumptions. The choice of the charge transport model will then have a major influence on the choice of generation and recombination models.

Drift-diffusion is the simplest model and has the attractive feature that it does not introduce any independent variables in addition to ψ, n and p. The drift-diffusion model was once adequate for nearly all devices that were technologically feasible. However, the drift-diffusion approximation becomes less accurate for smaller feature sizes. Advanced energy balance and hydrodynamic models are becoming popular for simulating deep submicron devices. ATLAS supplies both drift-diffusion and advanced transport models.

The Drift-Diffusion transport model

Derivations based upon the Boltzmann transport theory have shown that the current densities in the continuity equations may be approximated by a drift-diffusion model. In this case the current densities are expressed in terms of the quasi-Fermi levels φ_p and φ_n as

$$Jn = -q\mu nn \nabla \varphi n \quad (3.4)$$

$$Jp = -q\mu pn \nabla \varphi p \quad (3.5)$$

where μ_p and μ_n are the hole and electron mobilities. The quasi-Fermi levels are then linked to the carrier concentrations and the potential through the Boltzmann approximations:

$$n = n_{ie}\, exp[\frac{q(\Psi - \varphi_n)}{kT_L}] \tag{3.6}$$

$$p = n_{ie}\, exp[\frac{-q(\Psi - \varphi_p)}{kT_L}] \tag{3.7}$$

where n_{ie} is the effective intrinsic concentration and T_L is the lattice temperature. These two equations may then be re-written to define the quasi-Fermi potentials:

$$\varphi_n = \Psi - \frac{kT_L}{q} ln \frac{n}{n_{ie}} \tag{3.8}$$

$$\varphi_p = \Psi + \frac{kT_L}{q} ln \frac{p}{n_{ie}} \tag{3.9}$$

By substituting these equations into the current density expressions, we get the approximate current relationships. Taking into account the effects of band gap narrowing effective electric fields are normally defined as

$$\overrightarrow{E_n} = -\nabla [\Psi + \frac{kT_L}{q} ln\, n_{ie}] \tag{3.10}$$

$$\overrightarrow{E_p} = -\nabla [\Psi - \frac{kT_L}{q} ln\, n_{ie}] \tag{3.11}$$

which then allows the more conventional formulation of drift-diffusion equations to be written :

$$\overrightarrow{J_n} = qn\mu_n \overrightarrow{E_n} + qD_n \nabla n \tag{3.12}$$

$$\overrightarrow{J_p} = qn\mu_p \overrightarrow{E_n} - qD_p \nabla p \tag{3.13}$$

It should be noted that this derivation of the drift-diffusion model has tacitly assumed that the Einstein relationship holds. In the case of Boltzmann statistics, this corresponds to:

$$D_n = \frac{kT_L}{q}\mu_n \tag{3.14}$$

$$D_p = \frac{kT_L}{q}\mu_p \tag{3.15}$$

If Fermi-Dirac Statistics are assumed for electrons, equation 3.14 becomes

$$D_n = \frac{(\frac{kT_L}{q})F_{1/2}\{\frac{1}{kT_L}[\varepsilon_{F_n} - \varepsilon_C]\}}{F_{1/2}\{\frac{1}{kT_L}[\varepsilon_{F_n} - \varepsilon_C]\}} \tag{3.16}$$

where F_α is the Fermi-Dirac integral of order α, and ε_{F_n} is given by -qφ_n. An analogous expression is used for holes with Fermi-Dirac statistics.

Energy Balance Transport Model

An additional coupling of the current density to the carrier temperature or energy takes place in the higher order solution of the general Boltzmann Transport Equation. The current density expressions from the drift-diffusion model are modified to include this additional physical relationship. The electron current and energy flux densities are then expressed as:

$$\overrightarrow{J_n} = qD_n\nabla_n - \mu_n n\nabla\Psi + qnD_n^T\nabla T_n \tag{3.17}$$

$$\overrightarrow{S_n} = -K_n\nabla T_n - (\frac{k\delta_n}{q})\overrightarrow{J_n}T_n \tag{3.18}$$

$$\overrightarrow{J_p} = qD_p\nabla_p - \mu_p p\nabla\Psi - qpD_p^T\nabla T_p \tag{3.19}$$

$$\overrightarrow{S_p} = -K_p\nabla T_p - (\frac{k\delta_p}{q})\overrightarrow{J_p}T_p \tag{3.20}$$

where T_n and T_p represent the electron and hole carrier temperatures and S_n and S_p are the flux of energy(or heat) from the carrier to the lattice. The energy balance transport model includes a number of very complex relationships and therefore a later section of this chapter has been devoted to this model.

Displacement Current Equation

For the time domain simulations, the displacement current is calculated and included in the structure, log file and the run time outputs. The expression for displacement current is given as

$$\overrightarrow{J_{dis}} = \varepsilon\left(\frac{\delta \overline{E}}{\delta t}\right) \tag{3.21}$$

These equations from 3.1 to 3.21 are basic equations that are solved in the analysis of semiconductor devices. These different models can be implemented in Silvaco ATLAS, and these equations are modified in accordance with the mentioned models. Further information about the software is found in reference [16].

In our thesis to model a silicon optothyristor, we have used the simulators S-Pisces for simulating Si devices, Luminous for defining the ray trace and calculating the optical intensity, and Mixed Mode for circuit analysis when using the device in the capacitive discharge circuit and obtaining its circuit behavior.

Before simulating an opto-thyristor and observing its behavioral response in the capacitive discharge circuit, a general thyristor was taken from the PSPICE library, placed in a capacitive discharge circuit using a Schematic Capture, and simulated using PSPICE.

3.4 PSPICE Simulations

3.4.1 Thyristor as a Switch

Initially the switching performance of a thyristor simulated using PSPICE. Figure 3.2 shows the Schematic Capture result of the test circuit. Thyristor 2N6405 was used here as this device is the available in the PSPICE library. It has a maximum blocking voltage of 800V. The values for circuit elements were determined using limits mentioned in the datasheet of the thyristor 2N6405.

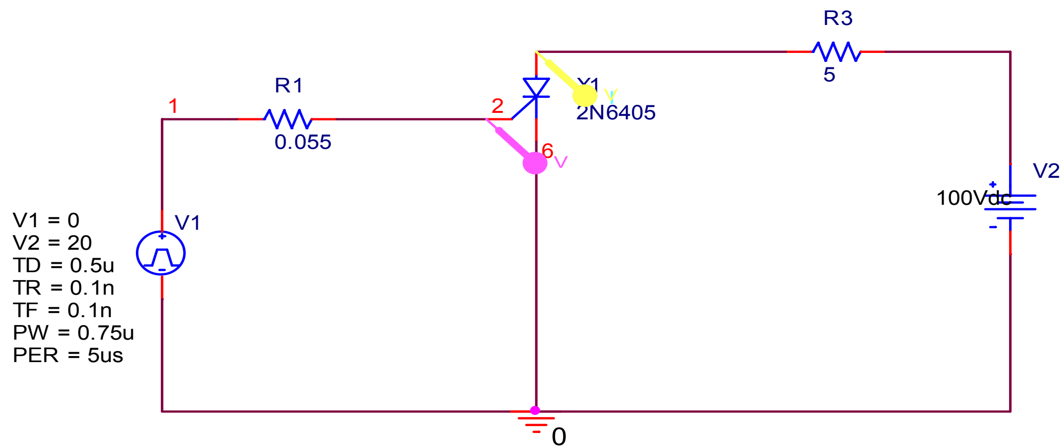

Figure 3.2 Schematic diagram for analysis of a thyristor as a switch

Figure 3.3 and Figure 3.4 are the simulation results of the above circuit with V_{cc} of 100 V and 400 V, respectively. The current and voltage waveforms of the thyristor are plotted along with the applied gate voltage

From the results we can observe that once the thyristor has acquired the required amount of charge in the gate pulse it turns on and stays on even after the removal of the gate pulse.

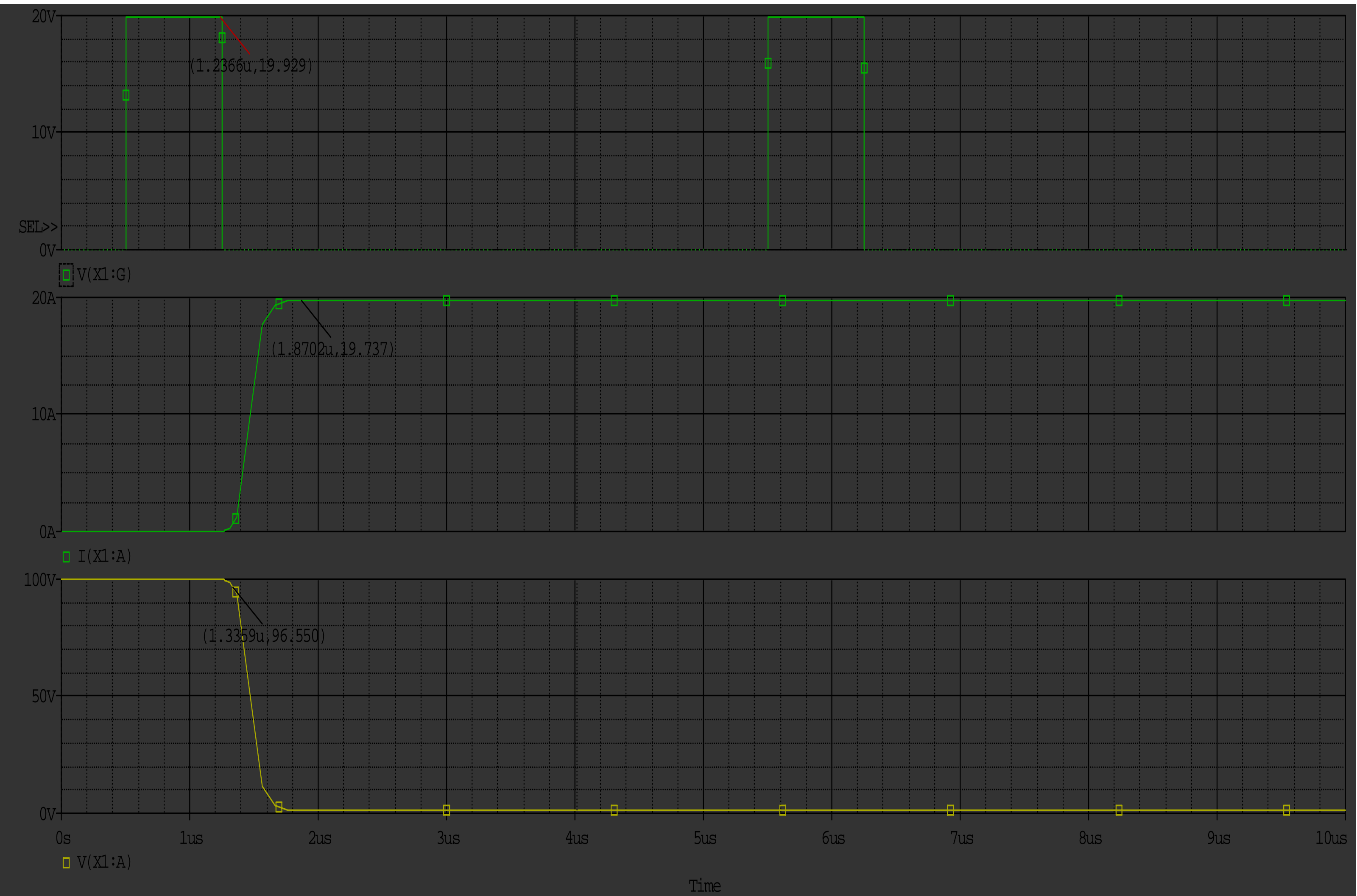

Figure 3.3 Thyristor turn-on with V_{AK}=100 V for the circuit shown in Figure 3.2

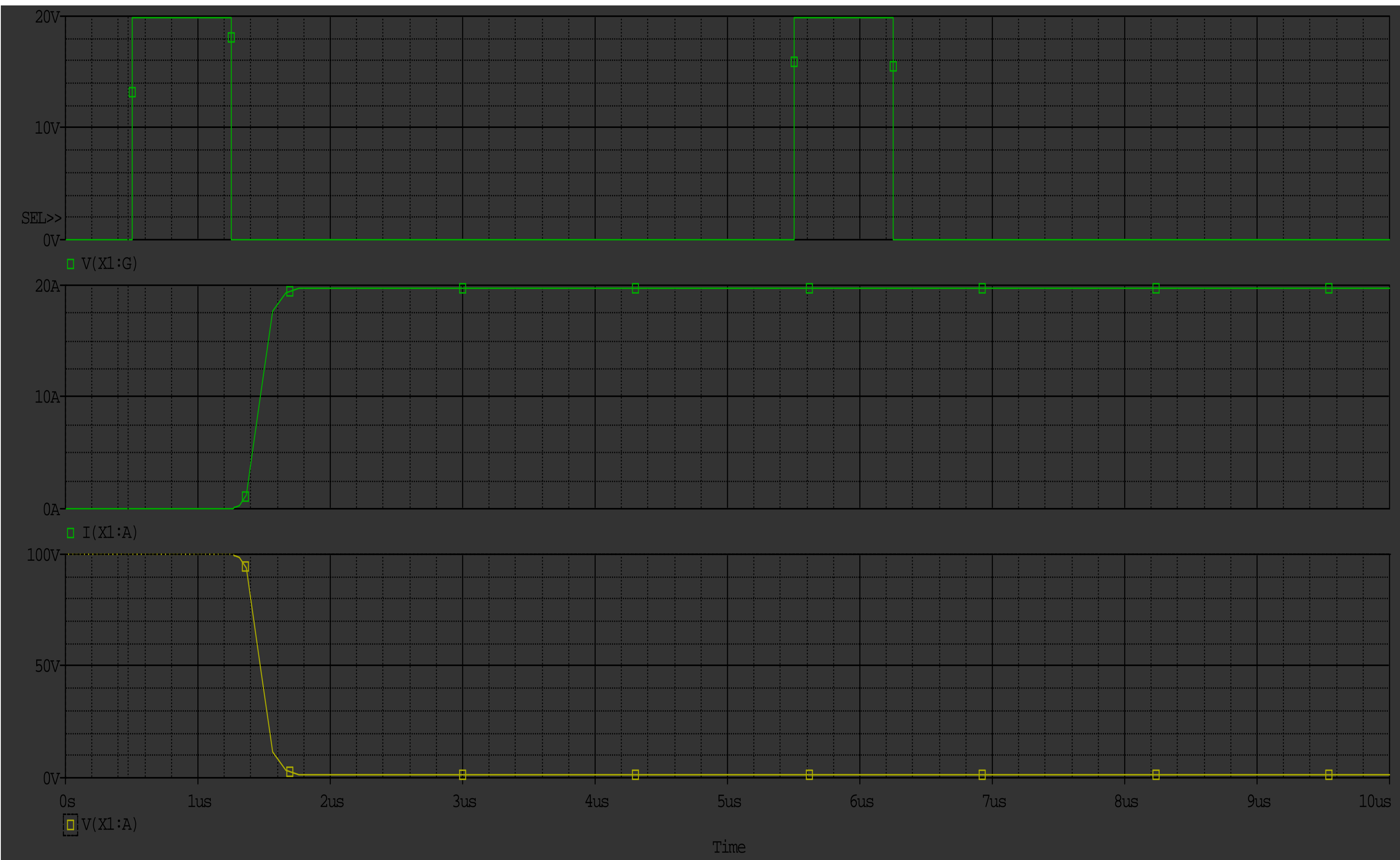

Figure 3.4 Thyristor turn-on with V_{cc}=400 V for the circuit shown in Figure 3.2

3.4.2 Thyristor in a Capacitor Discharge Circuit

Using the same thyristor 2N6405, its behavior in the capacitive discharge circuit shown in Figure 3.5 was simulated using PSPICE.. The resonant frequency is calculated using the equation

$$f = \frac{1}{2\pi\sqrt{LC}} \text{ Hz} \tag{3.22}$$

For the circuit shown in Figure 3.5 with stray inductance 7 nH and capacitor 0.2 μF the resonant frequency is 4.25 MHz.

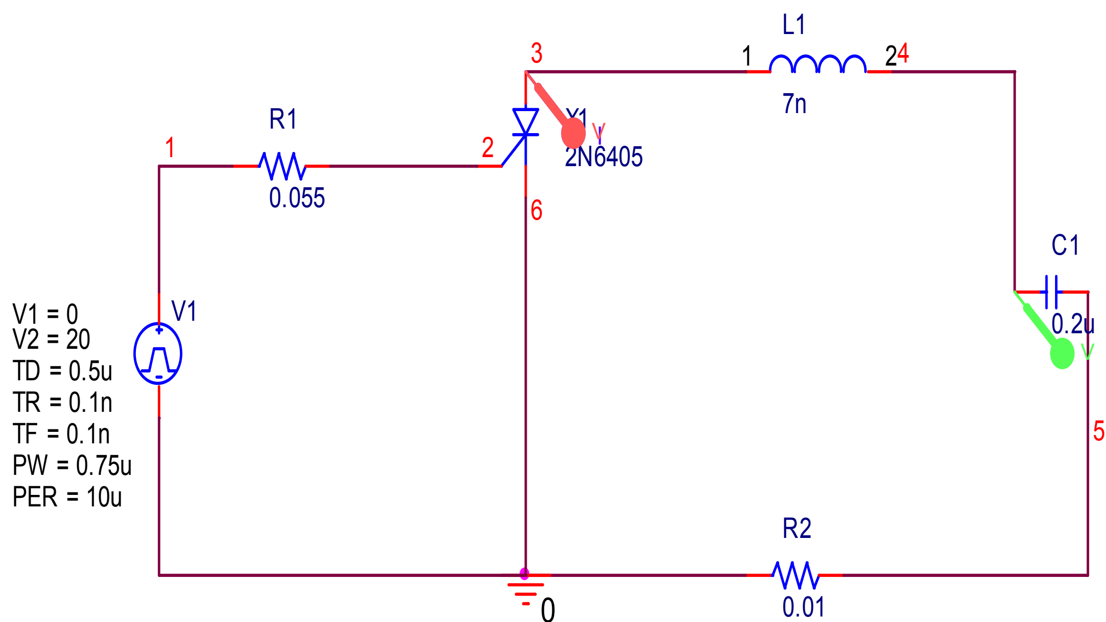

Figure 3.5Thyristor in a capacitive discharge circuit

To find the resonant frequency of the circuit a slight modification was made to Figure 3.5. The modified circuit is shown in Figure 3.6. The results of PSPICE frequency

analysis to check the resonant frequency of the circuit are shown in Figure 3.7, as can be seen the resonant frequency from the simulation is 4.217 MHz.

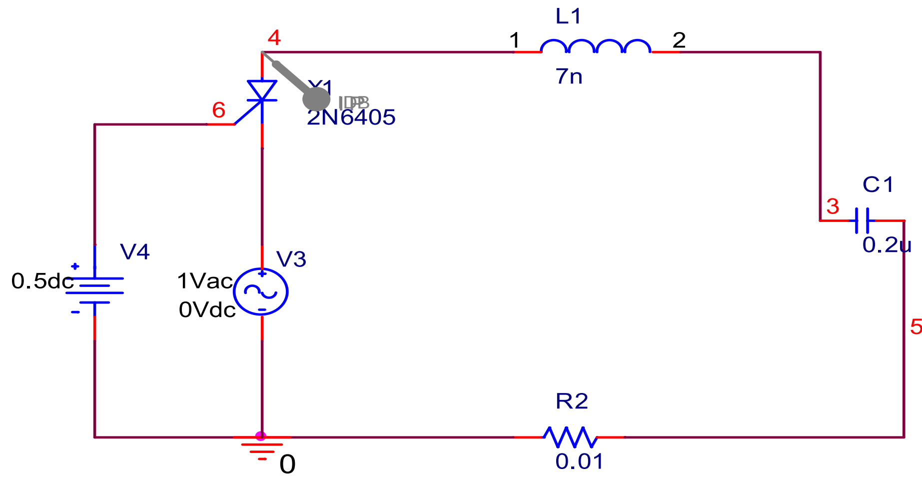

Figure 3.6 Circuit to find the resonant frequency

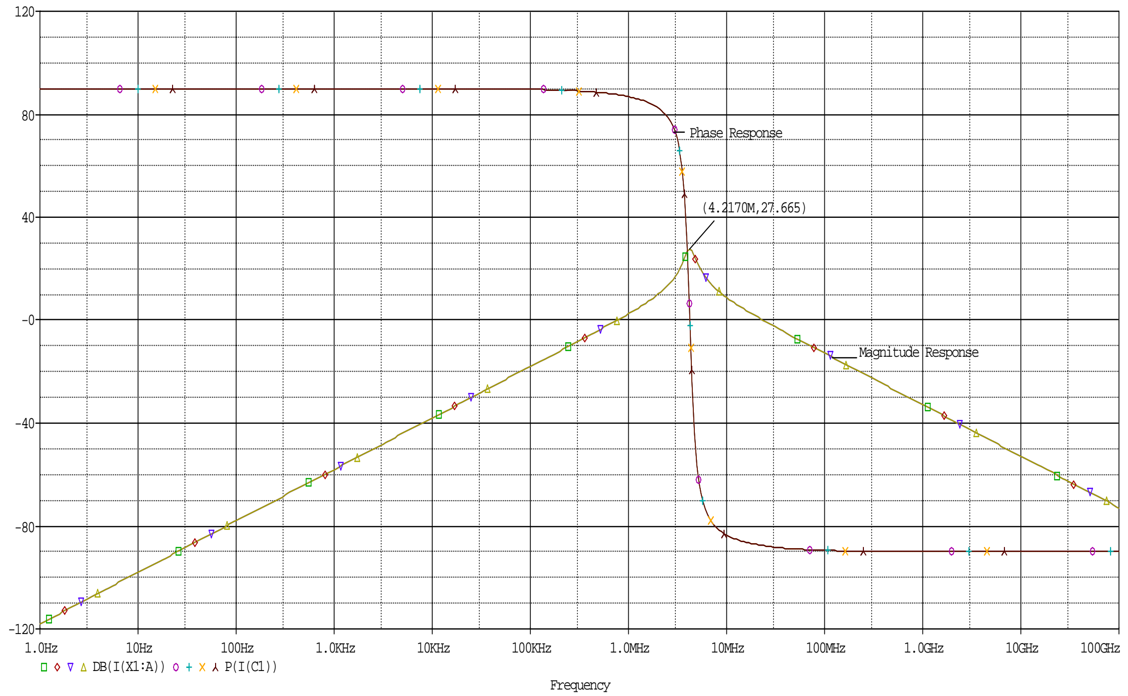

Figure 3.7 PSPICE frequency response of the circuit to determine the resonant frequency of the circuit

Simulation Results

The simulation results for an initial condition of 800 V on the capacitor are shown in Figure 3.8. The maximum anode thyristor current is which is also the capacitor current is 1.0557 kA, and the current rate of rise, di/dt (10% to 90% of the first rising edge of capacitor current) is 5.529 kA/µs.

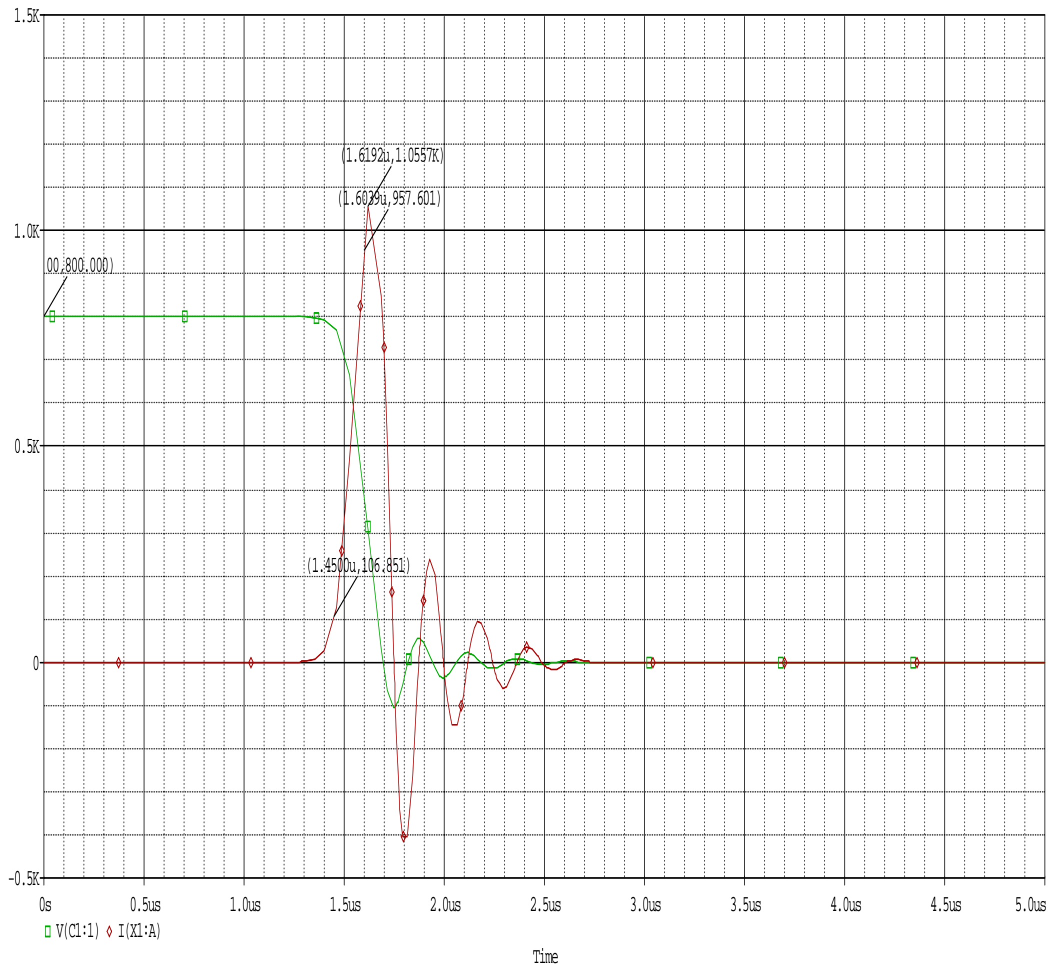

Figure 3.8 Capacitor current and switch voltage for the circuit shown in Figure 3.5. Initial capacitor voltage is 800 V.

The simulation results for an initial condition of 400 V on the capacitor are shown in Figure 3.9. Here the maximum anode current is 524.93 A and the di/dt is 2.825 kA/μs.

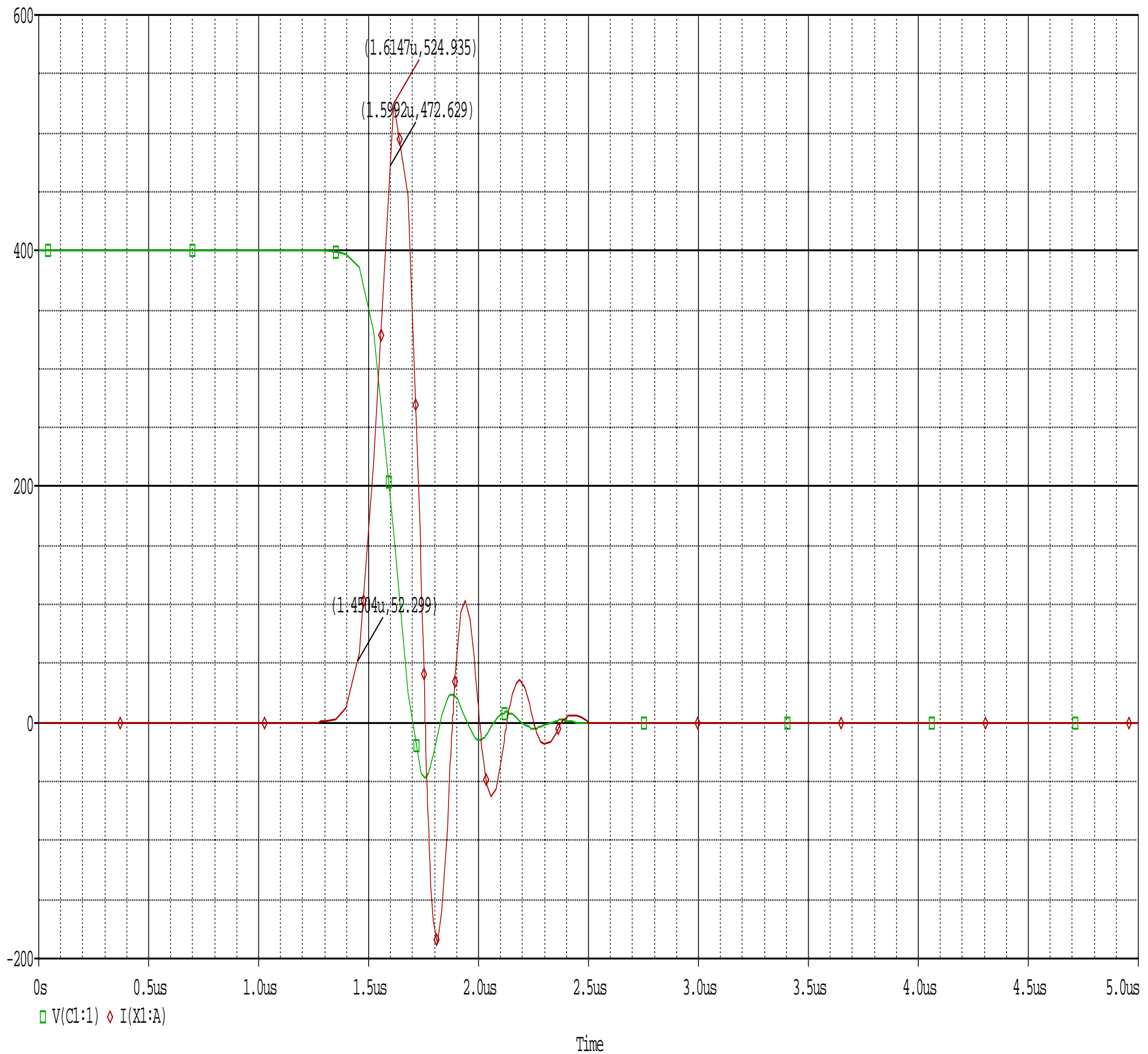

Figure 3.9 Capacitor current and switch voltage for the circuit shown in Figure 3.5. Initial capacitor voltage is 400 V

Figure 3.10 shows a comparison of the capacitor current in the circuit of Figure 3.5 with four different initial capacitor voltages.

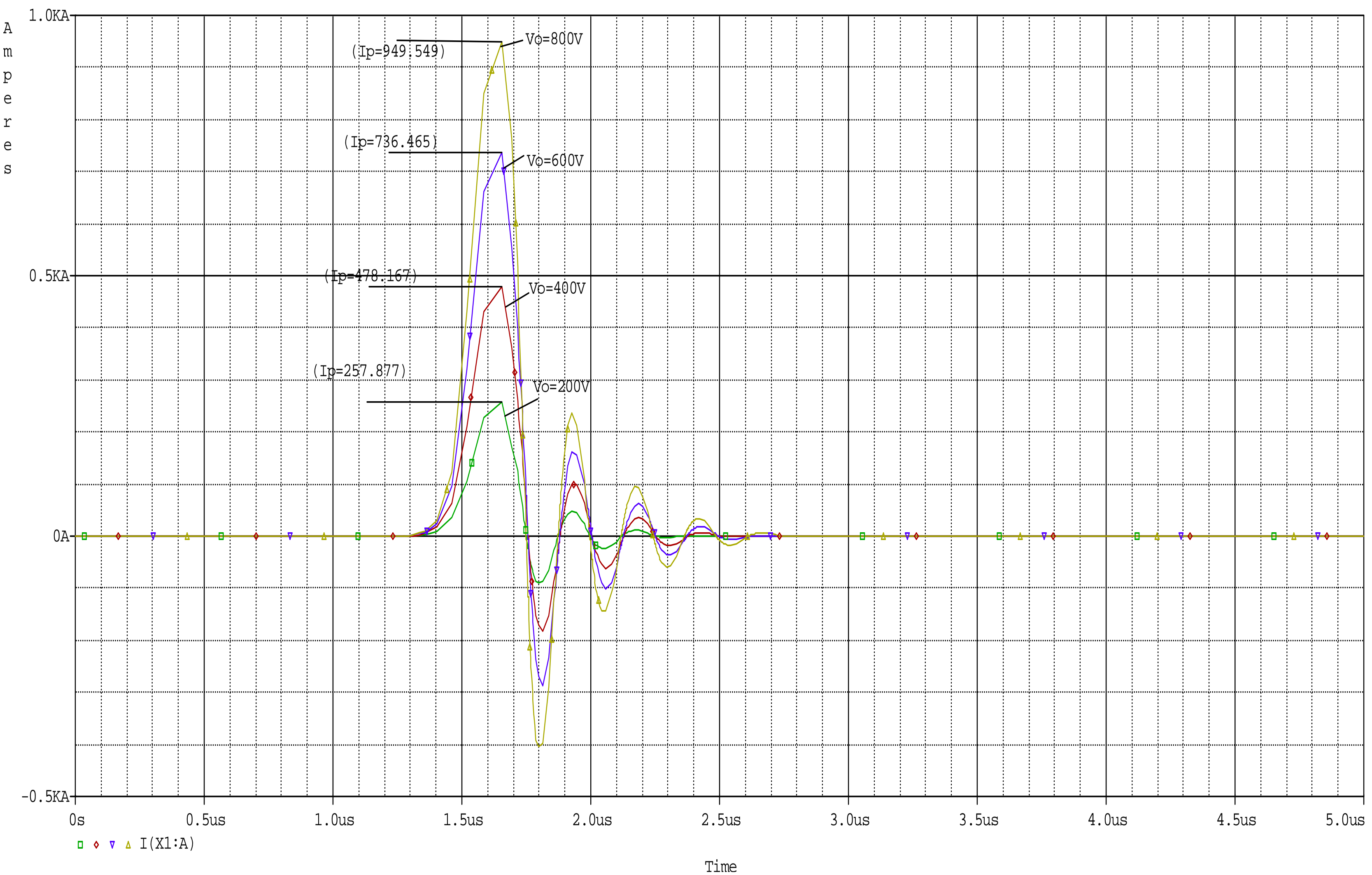

Figure 3.10 Comparison of capacitor discharge circuit current with initial conditions of 200 V, 400 V, 600 V, and 800 V on thecapacitor

After analyzing the performance of the thyristor in a capacitive discharge circuit with PSPICE, an opto-thyristor was designed using SILVACO Atlas. The reason for interest in a light-triggered thyristor is that it provides isolation of gate circuitry from the rest of the circuit. The advantage of isolation includes protection of devices from high voltages and human safety.

CHAPTER 4: SILVACO SIMULATION RESULTS

In this chapter we shall discuss the approach to modeling an opto-thyristor, and observe its characteristics and performance in a capacitive discharge circuit using SILVACO Atlas.

4.1 Approach to Design

The optically triggered thyristor has an advantage in high-voltage power circuits; there is perfect electrical separation between power and trigger circuits. The optical triggering is either indirect or direct. In indirect optical triggering of thyristors in HVDC systems, the trigger signal is transmitted to the high voltage valve via glass fibers and it is converted there into electrical signals[18],[19]. Direct light-triggering supersedes the complex procedure of having to convert optical pulses into electrical trigger pulses when the thyristors' voltage goes high. Eliminating this reduces the number of electrical and electronic components in the thyristor valve by around 80 percent in all, increasing the static converter valves' reliability and electromagnetic compatibility. To achieve this,

improvements and developments in light sources are required and modifications to the thyristor. The thyristor should be made sensitive to light sources of practical light levels while retaining the thyristor specifications [6]. Keeping in mind these requirements, a GaAs light emitter whose emission wavelength lies between 800-950 nm and has a mean penetration depth in silicon of about 10-50 μm was considered [17]. And also the thyristor gate structure was made light sensitive retaining the thyristor performance specification.

Here a dual amplifying gate structure is used where the gate of the first amplifying structure is made light sensitive. It is called the optical gate. Then, an amplifying gate acts to provide increased current to gate the following stages. This is to prevent the small gating stage from dissipating excessive power during its turn-on, short-conduction period and turn off [7]. Considering an electrically triggered thyristor with amplifying gate as shown in Figure 4.1 (i), the hole current from the gate is driven toward the cathode emitter. Along its path the hole current is separated into three components, one lateral component controlled by the p-base resistance and two-vertical components, displacement current and conduction current flowing through the p-base-n^+ emitter junction. Once this junction is forward biased the vertical resistive component becomes large enough to cause a return injection of holes from the p+ anode emitter. This fourth component of current determines the onset of turn-on and along with the injected electron current the device anode-cathode impedance varies. This first occurs in the inner edge of the pilot emitter from where the turn-on spreads. These current components now add up and appear as gate current to the next thyristor stage which turn-on the same way, as explained.

Now consider the case of the light-triggered thyristor as shown in Figure 4.1 (ii). The light sensitive region is illuminated by an optical pulse of laser or a led. This generates the necessary electron-hole pairs [16]. The hole current in this case also follows the same path as in the electrically triggered thyristor. However, when the electron from the photon caused electron-hole pair reaches the anode it causes the injection of the holes. Thus the hole injection does not have to wait until the n^+ emitter-pbase junction reaches the threshold voltage but begins instantaneously unlike in the case of the electrically triggered thyristor. This bonus of additional component plus an equal number of electrons being collected by the anode allows the anode junction to inject carriers sooner than in a conventional electrically gated thyristor [7]. With these points in view, we have modeled an opto-thyristor as shown in Figure 4.2.

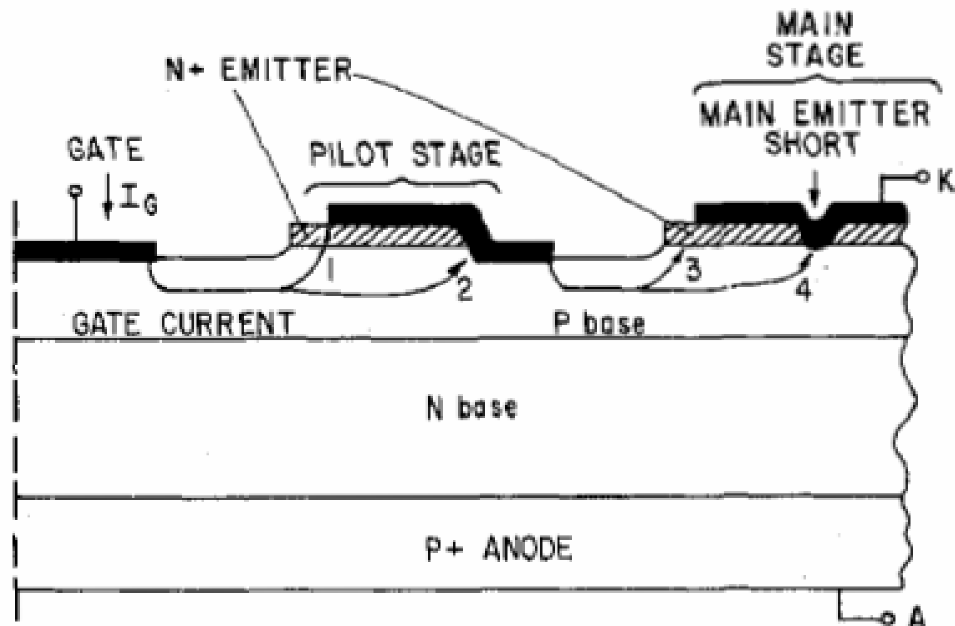

Figure 4.1 i) Electrically gated thyristor with amplifying gate

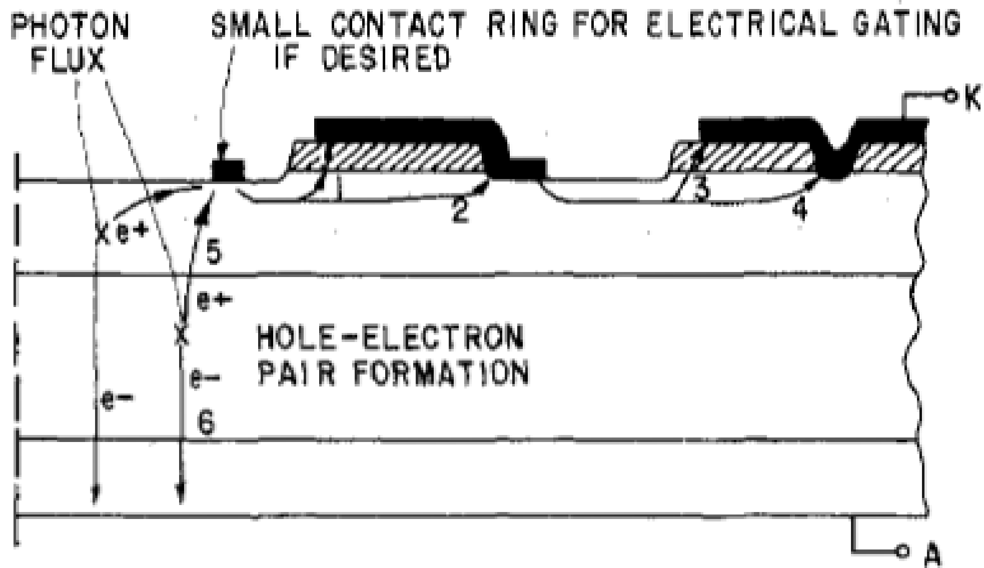

Figure 4.1 ii) Light triggered thyristor with amplifying gate.

Current components (hole) 1 and 2 bias and charge the main emitter junction, 3 and 4 do the same but for the main emitter junction. Components 1 and 3 are each composed of a capacitive component which charges up the n+ emitter-p base junction capacitance-resistive component whose relative size depends on the p-n junction voltage. Components 5 (hole) and 6 (electron) are composed of photon generated electron-hole pairs separated in the field of reverse biased n base- p base junction.

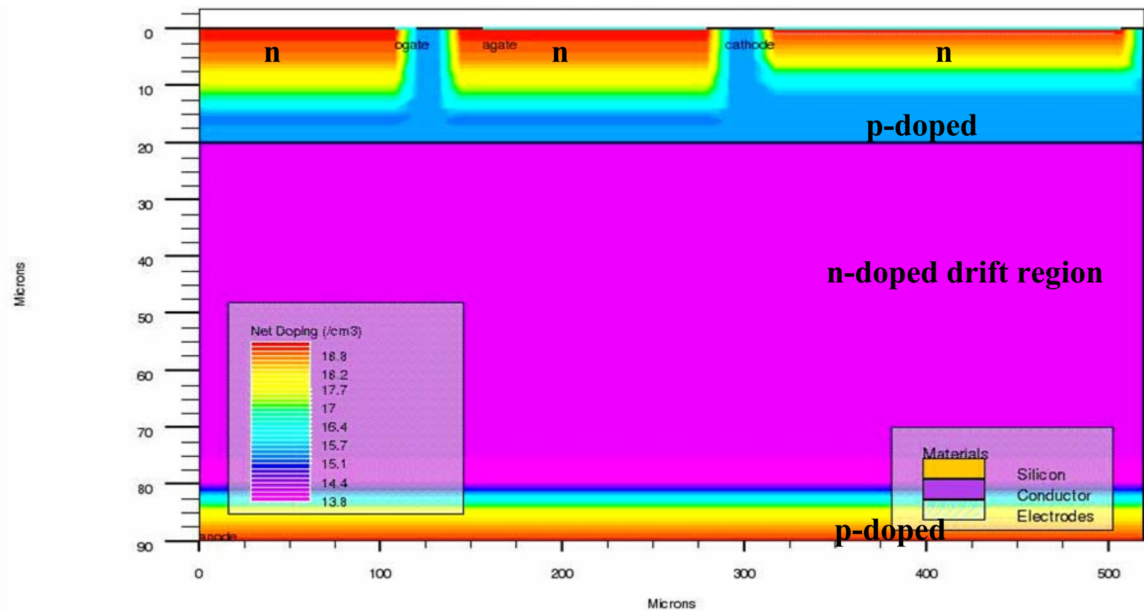

Figure 4.2 Structure of an opto-thyristor for simulation study

4.2 ATLAS approach in designing the opto-thyristor

Each input file to ATLAS must contain the five groups of information shown in Figure 4.3. The order of statements in which they occur are important or else it would lead to incorrect operation of the program.

Group	Statements
1. Structure Specification	MESH REGION ELECTRODE DOPING
2. Material Models Specification	MATERIAL MODELS CONTACT INTERFACE
3. Numerical Method Selection	METHOD
4. Solution Specification	LOG SOLVE LOAD SAVE
5. Results Analysis	EXTRACT TONYPLOT

Figure 4.3 ATLAS Command Groups with man statements in each group

4.2.1 Structure Specifications

Structure specification includes generation of mesh, defining regions and electrodes, and doping for the device.

Mesh Generation

Mesh generation plays an important role in obtaining good simulations for the process in a semiconductor device. If we don't take proper care it leads to incorrect measurements. A finer mesh should be placed at the p-n junctions of the device where the carrier activity takes place. Avoid formation of obtuse triangles in current paths or high field areas. Simulations carried on with finer mesh take a longer time and making the mesh coarse leads to slight deviations from actual values. An optimal mesh is to be designed where we can get a compromise with speed and accuracy. The mesh that we have considered for our device is as shown in the Figure 4.4.

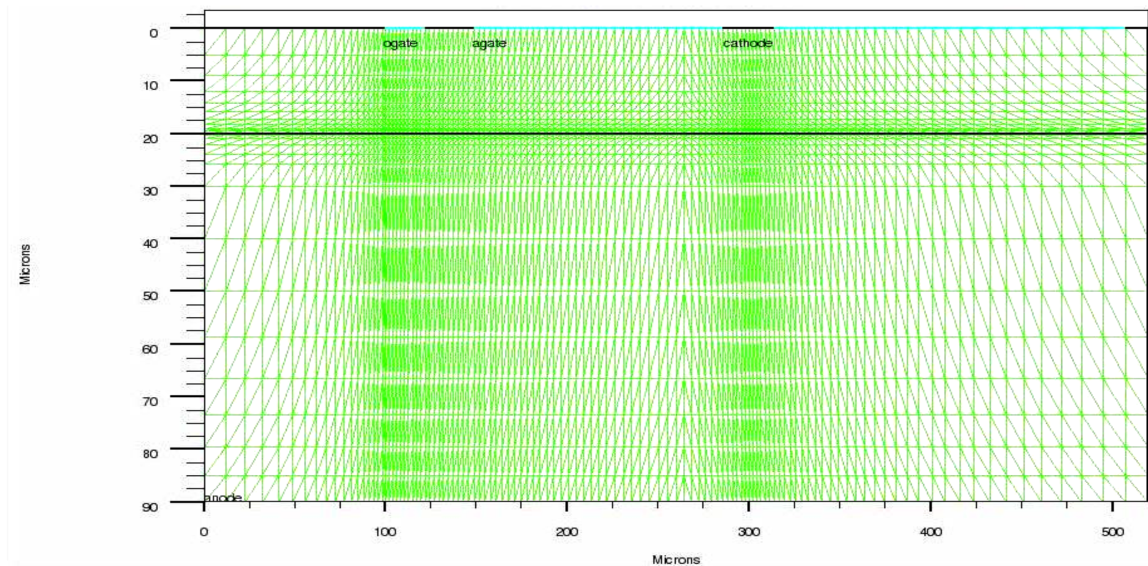

Figure 4.4 Simulation mesh of opto-thyristor

Device Generation

The initial design of the opto-thyristor is a rectangular silicon structure 520 μm wide and 90 μm deep. The radial structure of the thyristor has an optical gate area in its center. An amplifying gate is placed in between the optical gate and the cathode.

The anode is in contact with the diffused p-doped region. The peak concentration is $1x10^{19}$ cm^{-3} and the junction depth is 10 μm. The uniformly n-doped drift region is 60 μm thick and the doping concentration is $1x\ 10^{14}$ cm^{-3}. The top region features a 20 μm thick area with a constant p-doping level of $2x10^{15}$ cm^{-3}. In this region, three implanted n-gaussian regions with peak concentrations of $1x10^{19}$ cm^{-3} are found. From left to right, they are the optical gate, the amplifying gate, and the cathode regions. The optothyristor has electrodes connected to the optical gate and the amplifying gate for the option of observing electrical triggering. The gate region depth is about 15 μm and the cathode depth is 10 μm. Figure 4.2 shows the structure of the opto-thyristor and Figure 4.5 shows the position of light incidence on the structure.

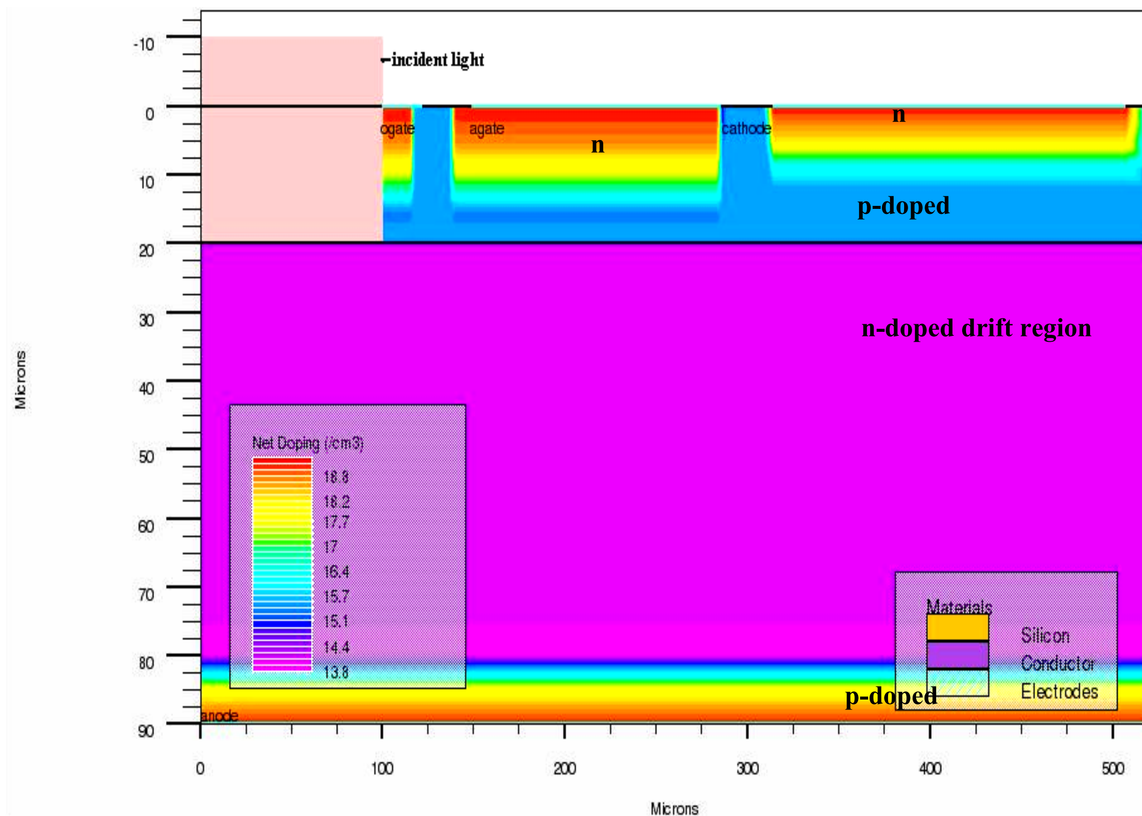

Figure 4.5 Structure showing the incidence of light

4.2.2 Material Model Selection

As stated earlier we have used silicon as the basic material in the design of the opto-thyristor. The models that are used during this simulation are as follows:

Carrier generation and Recombination Models

Carrier generation and recombination are the processes by which the semiconductor material is moved away from thermal equilibrium and returned to equilibrium after being disturbed from it. In our case, the generation is by light shining on the p-base of the semiconductor, which causes disturbance of equilibrium by the creation of excess holes and electrons, and recombination is by the *Auger* and *SRH* (Shockley-Read-Hall) processes.

Auger recombination is described by the following expression

$$R_{auger} = AUGN(pn^2 - nn_{ie}^2) + AUGP(np^2 - pn_{ie}^2) \quad (4.1)$$

where the model parameters AUGN and AUGP are user definable.

The Shockley-Read-Hall recombination is modeled as follows:

$$R_{SRH} = \frac{pn - n_{ie}^2}{TAUP0[n + n_{ie}\exp(\frac{ETRAP}{kT_L})] + TAUN0[p + n_{ie}\exp(\frac{-ETRAP}{kT_L})]} \quad (4.2)$$

where ETRAP is the difference between the trap energy level and the intrinsic Fermi level, T_L is the lattice temperature in degrees Kelvin and TAUN0 and TAUP0 are the respective electron and hole lifetimes, which are user definable.

Mobility Modeling

Electrons and holes accelerate by electric fields but lose momentum due to various scattering processes like lattice vibrations (phonons), impurity ions or other carriers, surfaces and other material imperfections. The microscopic phenomena effect the mobilities introduced by the transport equation and therefore these mobilities are a function of the local electrical field, doping concentration, lattice temperature and more. Mobility models like *analytic,* which is used to specify the doping and temperature-dependent low field mobilities, and *fldmob* (parallel electric field dependence) which is required for modeling Si devices to model any velocity saturation effect, were used in our simulations.

Carrier statistics

In the presence of heavy doping (greater than 10^{18} cm^{-3}) the pn product in silicon becomes doping dependent [16]. As doping increases the band gap decreases where the conduction band decreases the same amount as the valence band is raised. This feature is considered by using the model *bgn* (band gap narrowing).In ATLAS this is simulated by spatially varying the intrinsic concentration n_{ie} defined according to

$$n_{ie}^2 = n_i^2 \exp(\frac{\Delta E_g}{kT}) \tag{4.3}$$

All these variation in ΔE_g to the doping concentration is solved by ATLAS on mentioning the bgn mode

4.2.3 Numerical Method and Solution Specification and Results analysis

Numerical Method: A numeric method is used to obtain the numerical solution for the overall process. The Newton 2 method was used here to solve the non-linear equations.

This is the default method for solving the drift-diffusion calculations and for performing the curve tracing, DC, and transient calculations.

Solution Specifications: The DC, curve-tracing or transient are solved and the solutions are saved in the log files which can later be either used in other programs by using the commands load and save.

Result Analysis: Tonyplot a visualistion tool helps to view these results. The log and the structure files can be viewed and analysed.

4.3 Opto-thyristor Dark Current Analysis

Initially the I-V characteristics of the prototype thyristor are obtained by applying forward bias voltage across the device. The breakover voltage V_{BO} of the device is found to be 274.5 V. Next by applying a reverse bias across the device we found the breakdown voltage to be 312 V. Figure 4.6 and Figure 4.7 shows the I-V characteristics of the device.

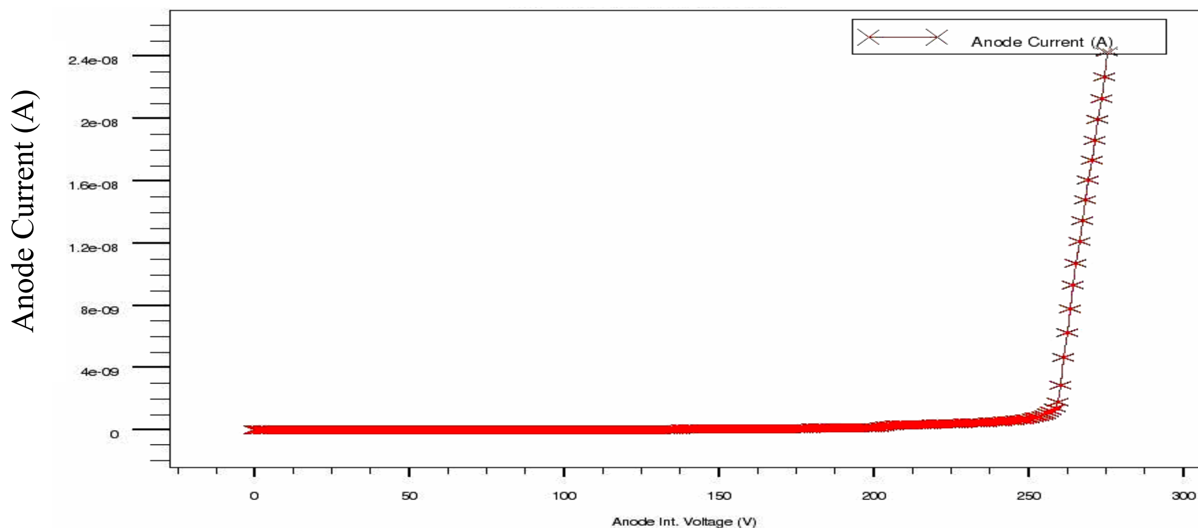

Figure 4.6 Forward characteristics of an Opto-thyristor with drift region concentration 1*10^{-14} cm^{-3} and length 60µm

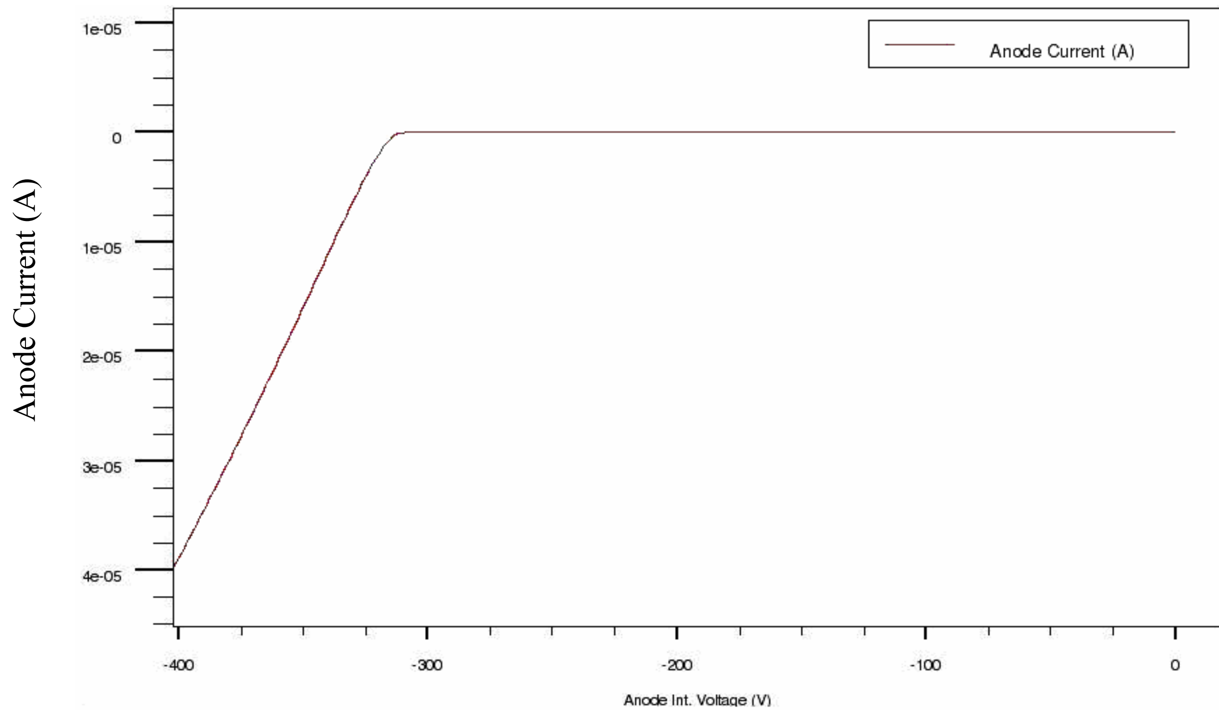

Figure 4.7 Reverse characteristics of an Opto-thyristor with drift region concentration $1*10^{-14}$ cm $^{-3}$ and length 60µm

To observe the dependence of the I-V characteristics on the drift region doping concentration, the same procedure as above was repeated with drift concentrations of $1*10^{-13}$ cm^{-3} and $1*10^{-15}$ cm^{-3}. Figure 4.8 and Figure 4.9 shows the forward and reverse characteristics of the optothyristor with drift region concentration $1*10^{-13}$ cm $^{-3}$. The breakover and breakdown voltages for this device are found to be 25.2 V and 27.2 V, respectively.

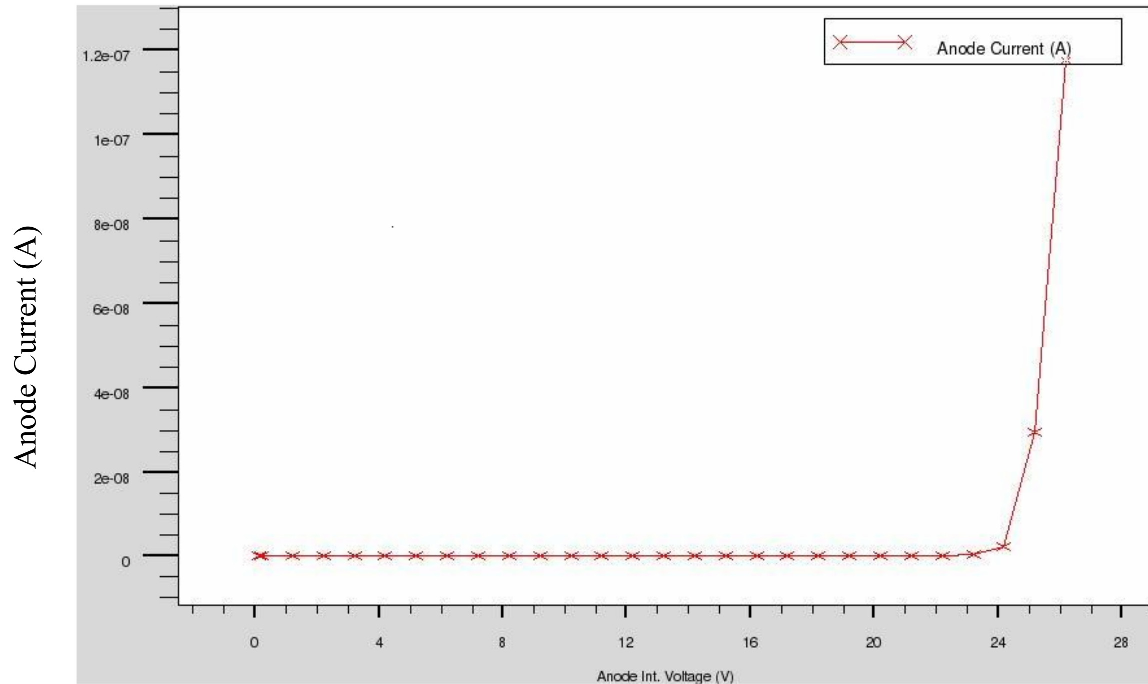

Figure 4.8 Forward characteristics of an Opto-thyristor with drift region concentration $1*10^{-13}$ cm^{-3} and length 60µm

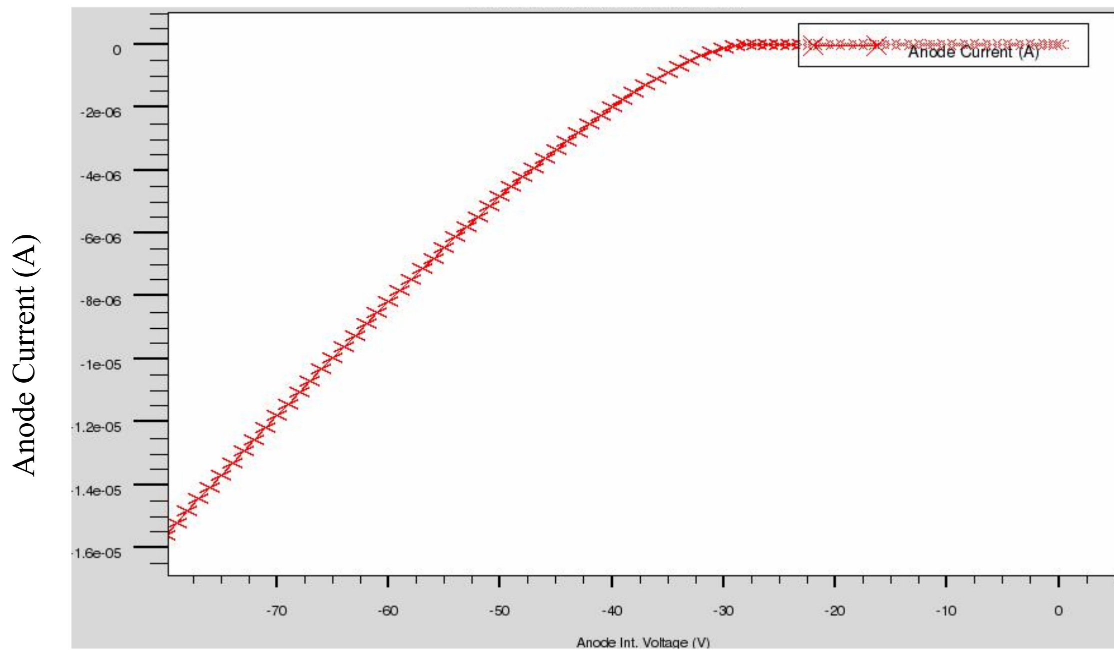

Figure 4.9 Reverse characteristics of an Opto-thyristor with drift region concentration $1*10^{-13}$ cm^{-3} and length 60µm

Figure 4.10 and Figure 4.11 show the forward and reverse characteristics of the opto-thyristor with drift region concentration $1*10^{-15}$ cm $^{-3}$. The breakover and breakdown voltages for this device are found to be 72 V and 294 V, respectively.

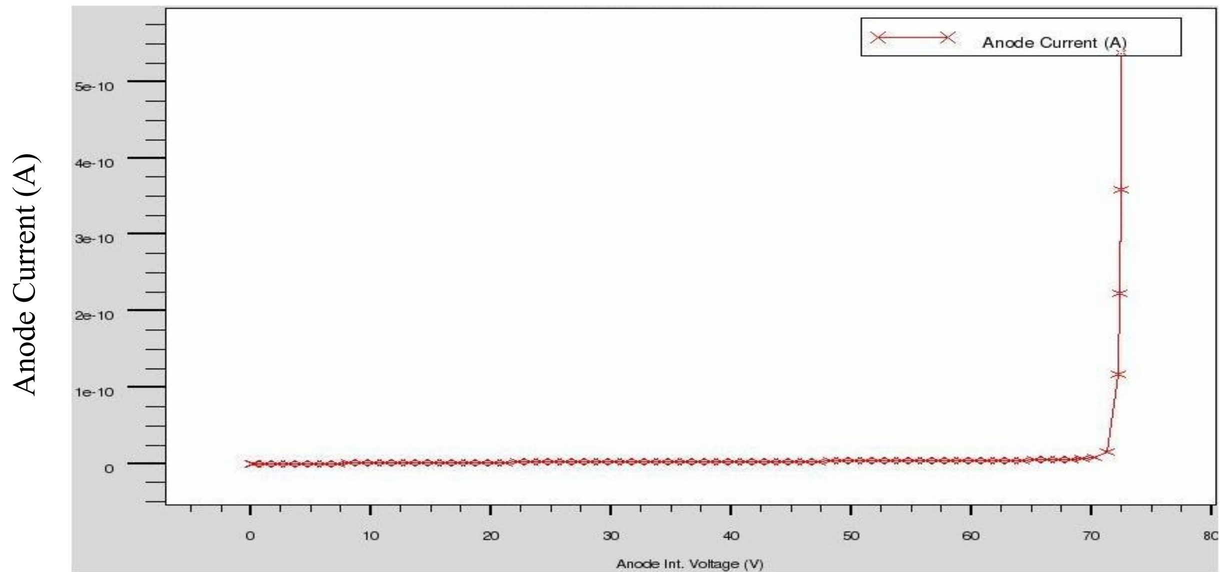

Figure 4.10 Forward characteristics of an Opto-thyristor with drift region concentration $1*10^{-15}$ cm $^{-3}$ and length 60µm

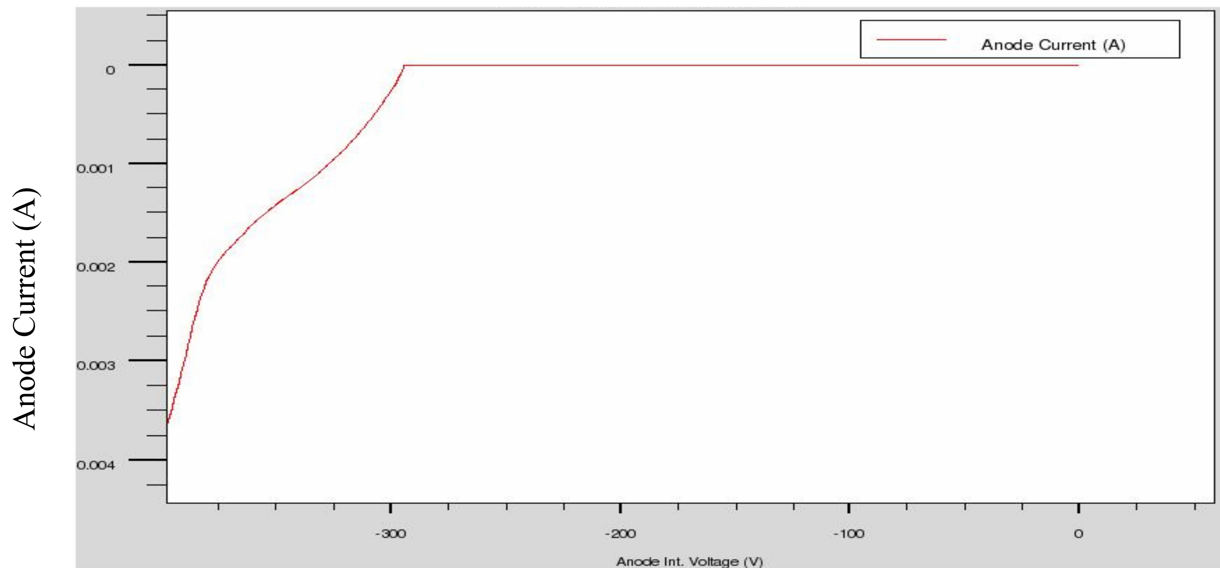

Figure 4.11 Reverse characteristics of an Opto-thyristor with drift region concentration $1*10^{-15}$ cm $^{-3}$ and length 60µm.

To observe the dependence of the IV characteristics of the device on the length of the drift region, we doubled the length of the drift region to 120 µm and reran the program to observe the IV characteristics for different drift region concentrations. Figure 4.12 and Figure 4.13 shows the forward and reverse characteristics of the opto-thyristor with concentration $1*10^{-13}$ cm $^{-3}$ and the drift region length being 120 µm. The breakover and breakdown voltages for this device were found to be 100 V and 110 V, respectively.

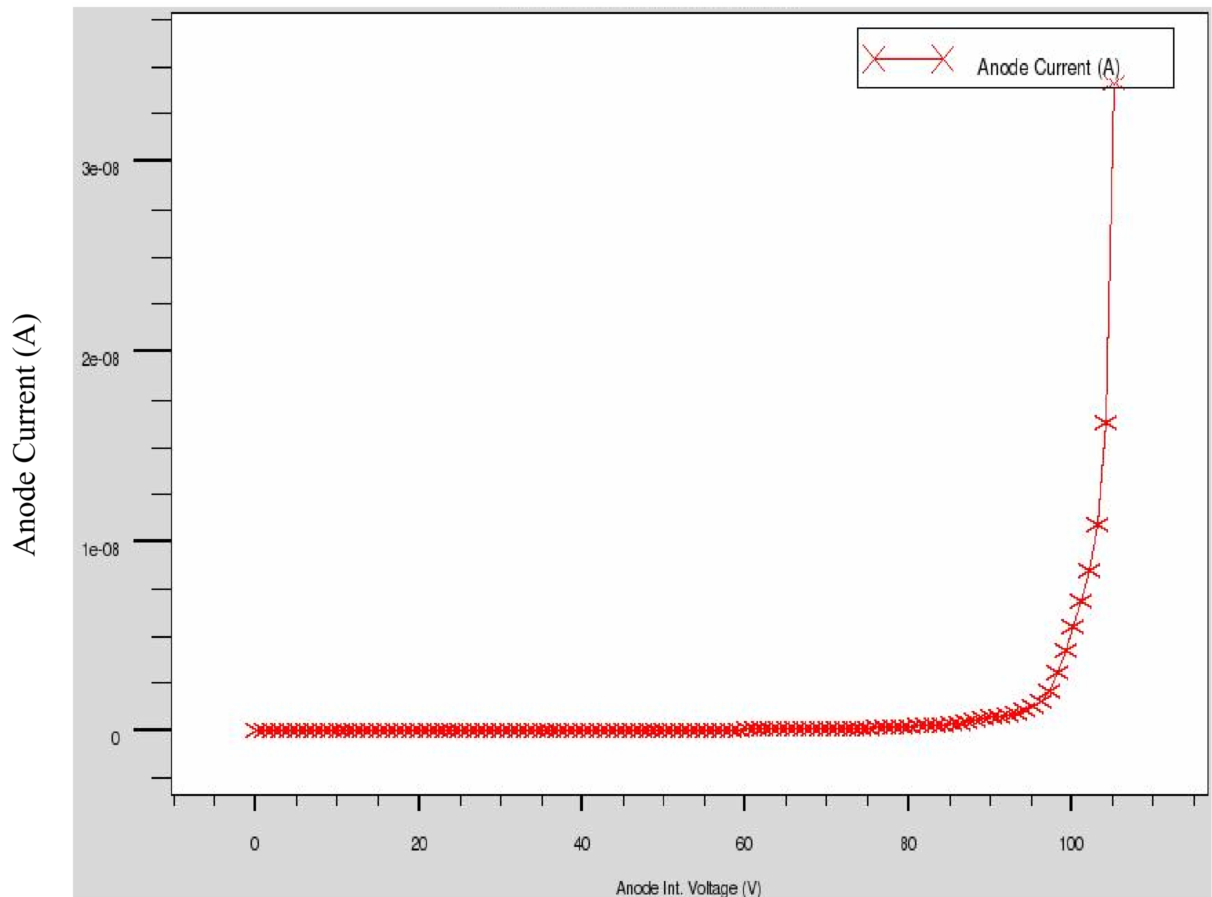

Figure 4.12 Forward characteristics of an Opto-thyristor with drift region concentration $1*10^{-13}$ cm $^{-3}$ and length 120µm

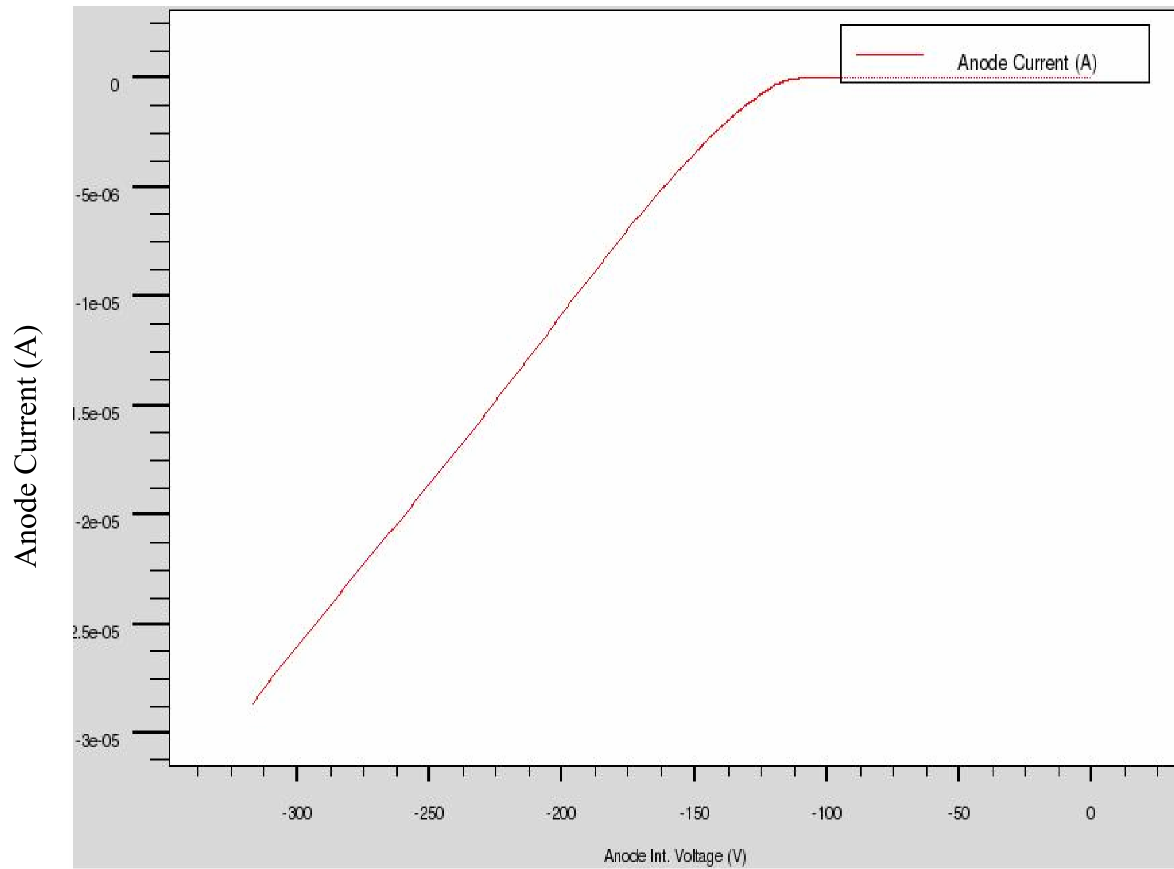

Figure 4.13 Reverse characteristics of an Opto-thyristor with drift region concentration $1*10^{-13}$ cm $^{-3}$ and length 120 µm

On repeating the same the forward and reverse characteristics of the opto-thyristor with concentration $1*10^{-14}$ cm $^{-3}$ and the drift region length 120 µm the breakover and breakdown voltages were found to be 522 V and 1150 V, respectively. Finally with concentration $1*10^{-15}$ cm $^{-3}$ and the drift region length being 120 µm, the breakover and breakdown voltages for this device were found to be 75 V and 337 V, respectively. Figure 4.14 and Figure 4.15 shows, respectively the forward and reverse characteristics of all the concentrations with drift region length 120 µm. The results of this section are summarized in Table 4-1 and Table 4-2.

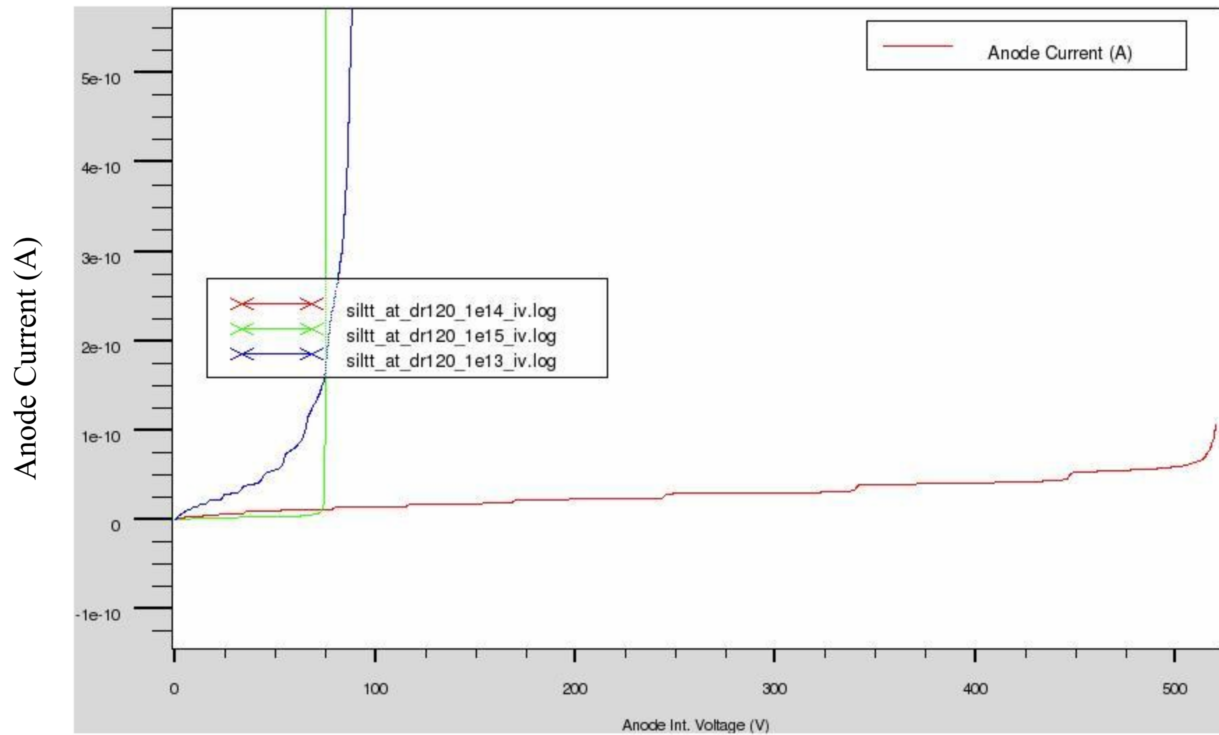

Figure 4.14 Overlay of forward characteristics of an opto-thyristor with drift region concentrations $1*10^{-13}$ cm $^{-3}$, $1*10^{-14}$ cm $^{-3}$and $1*10^{-15}$ cm $^{-3}$ and length 120 µm

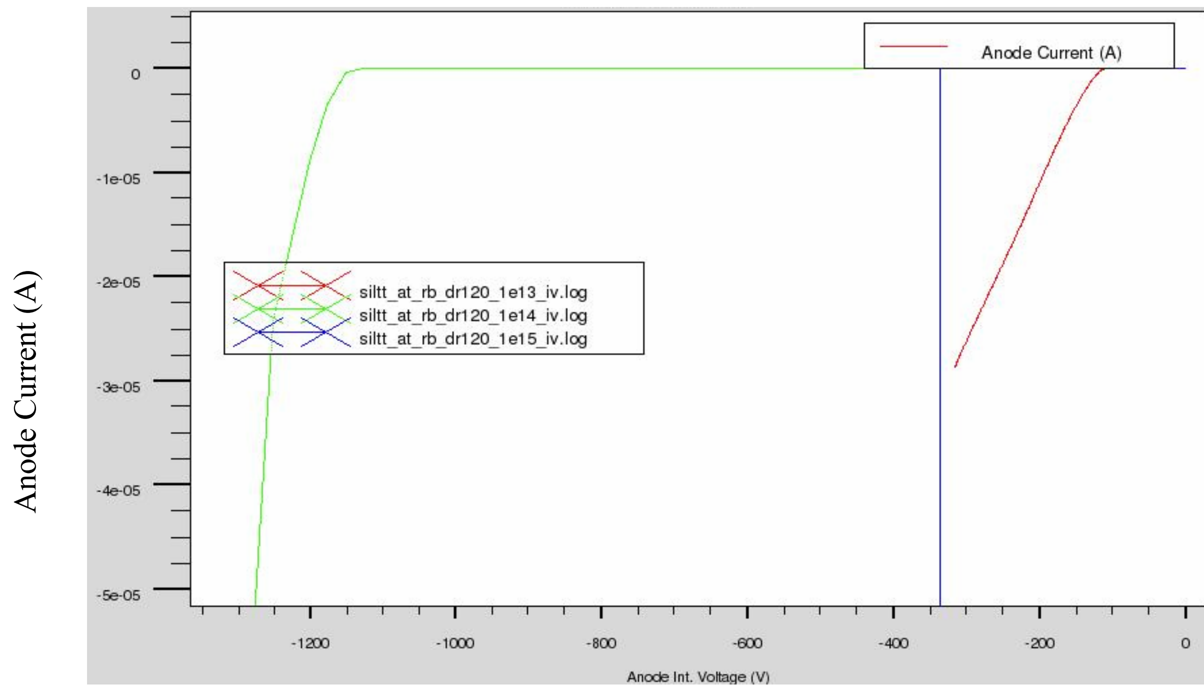

Figure 4.15 Overlay of reverse characteristics of an Opto-thyristor with drift region concentrations $1*10^{-13}$ cm $^{-3}$, $1*10^{-14}$ cm $^{-3}$and $1*10^{-15}$ cm $^{-3}$ and length 120 µm

Drift Region Concentration / **Width**	**1e13**	**1e14**	**1e15**
60 µm	*25.2*	*274.5*	72
120 µm	*100*	*522*	*75*

Table 4-1 Breakover voltages of the different opto-thyristors

Drift Region Concentration / **Width**	**1e13**	**1e14**	**1e15**
60 µm	*27*	*312*	294
120 µm	*110*	*1150*	*337*

Table 4-2 Breakdown voltages of the different opto-thyristors

The obtained results are compared with theoretical silicon thyristor break-down voltages as per Figure 4.16[22]. These theoretical results are tabulated in Table 4.3.3.

Drift Region Concentration / **Width**	**1e13**	**1e14**	**1e15**
60 µm	*22*	*360*	220
120 µm	*130*	*1300*	*220*

Table 4-3 Theoritical values of Break down Voltages of the Si- thyristors

The simulated breakdown voltage values of the opto-thyristors are in reasonable agreement with the theoretical values of the breakdown voltages of silicon thyristors. This shows that the simulations taken into account both the punch-through and the non-punch through conditions.

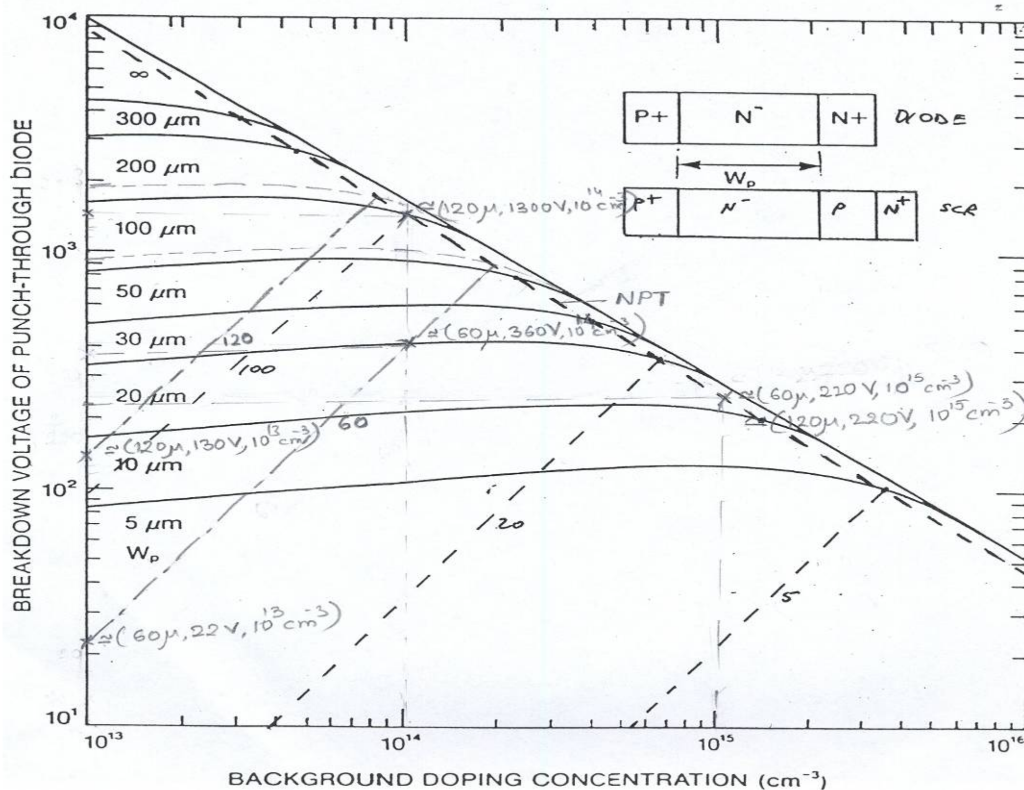

Figure 4.16 Breakdown voltages of punch-through diodes and thyristors (dashed-line)

Now, categorizing these into six models and naming them as:

Model 1: Opto-thyristor with drift region length 60 μm and concentration $1*10^{-13}$ cm $^{-3}$

Model 2: Opto-thyristor with drift region length 60 μm and concentration $1*10^{-14}$ cm $^{-3}$

Model 3: Opto-thyristor with drift region length 60 μm and concentration $1*10^{-15}$ cm $^{-3}$

Model 4: Opto-thyristor with drift region length 120 μm and concentration $1*10^{-13}$ cm $^{-3}$

Model 5: Opto-thyristor with drift region length 120 μm and concentration $1*10^{-14}$ cm $^{-3}$

Model 6: Opto-thyristor with drift region length 120 μm and concentration $1*10^{-15}$ cm $^{-3}$

We notice that the Models 1, 2, and 4 on application of reverse bias voltage reach the state of punch-through whereas the other models lie in the region of non-punch through.

4.4 Optothyristor Turn on Transient

Optical Absorption in Silicon

For good use of optically generated carriers, the photons should be absorbed where the electron-hole pairs are needed. As Figure 4.17 shows this could be from 10 – 20 μm into the silicon. In our simulation we used light of wavelength 0.9 um, for which the optical absorption depth is as shown in Figure 4.17.

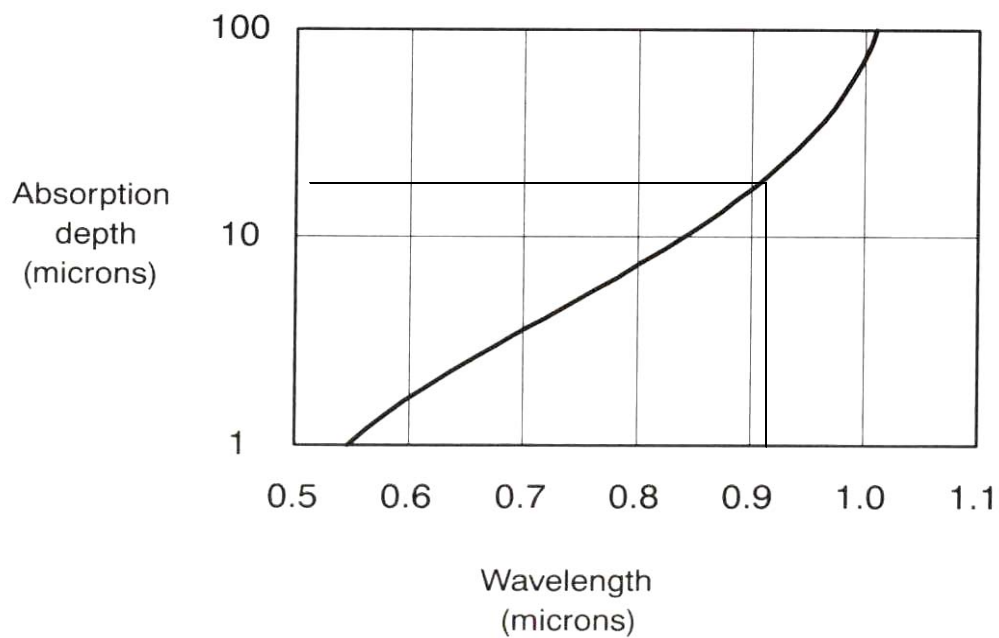

Figure 4.17 Optical Absorption depth vs Wavelength is Silicon

Model 1

The opto-thyristor that was modeled was then tested for its optically gated turn on behavior. The general test circuit for the thyristor is as shown in Figure 4.18**.** The applied light source is a pulse to observe the transient behavior of the device. All these simulations used the ATLAS Mixed mode simulator, in which the third dimension of the device was set to 520 μm.

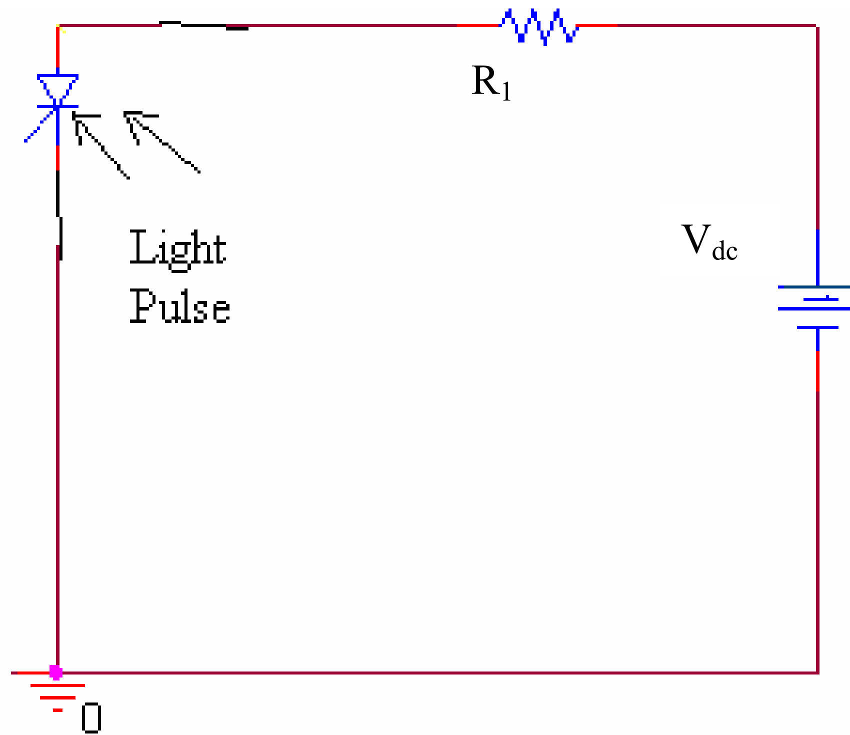

Figure 4.18 General test circuit for the simulation of turn-on transient for the opto-thyristor

In the circuit of Figure 4.4.2 V_{dc} is 20 V and R_1 is 8 ohms. The light pulse, whose wavelength is 0.9 μm, is ramped to 9 Watts/cm^2 intensity with pulse width of 0.01 μs with the initial delay (t_d) of 1μs and rise time (t_r) of 1 ns and fall time(t_f) of 1 ns . The pulse period is 10 μs. V_{dc} is limited to the blocking voltage of the opto-thyristor. If this value is greater than V_{bo} the opto-thyristor will turn on even without the application of light. On maintaining V_{dc} less than or equal to V_{bo}, the voltage across the thyristor and current through the thyristor were observed. After going through the pnpn regenerative action, the device latches on and the voltage across it falls, and the current rises to a value

approximately equal to V_{dc}/R_1. These results are shown in Figure 4.19. The on-state current I_{on} = 2.38 A and the on-state voltage V_{on} = 0.98 V. Also, di/dt = 5.9 A/µsec.

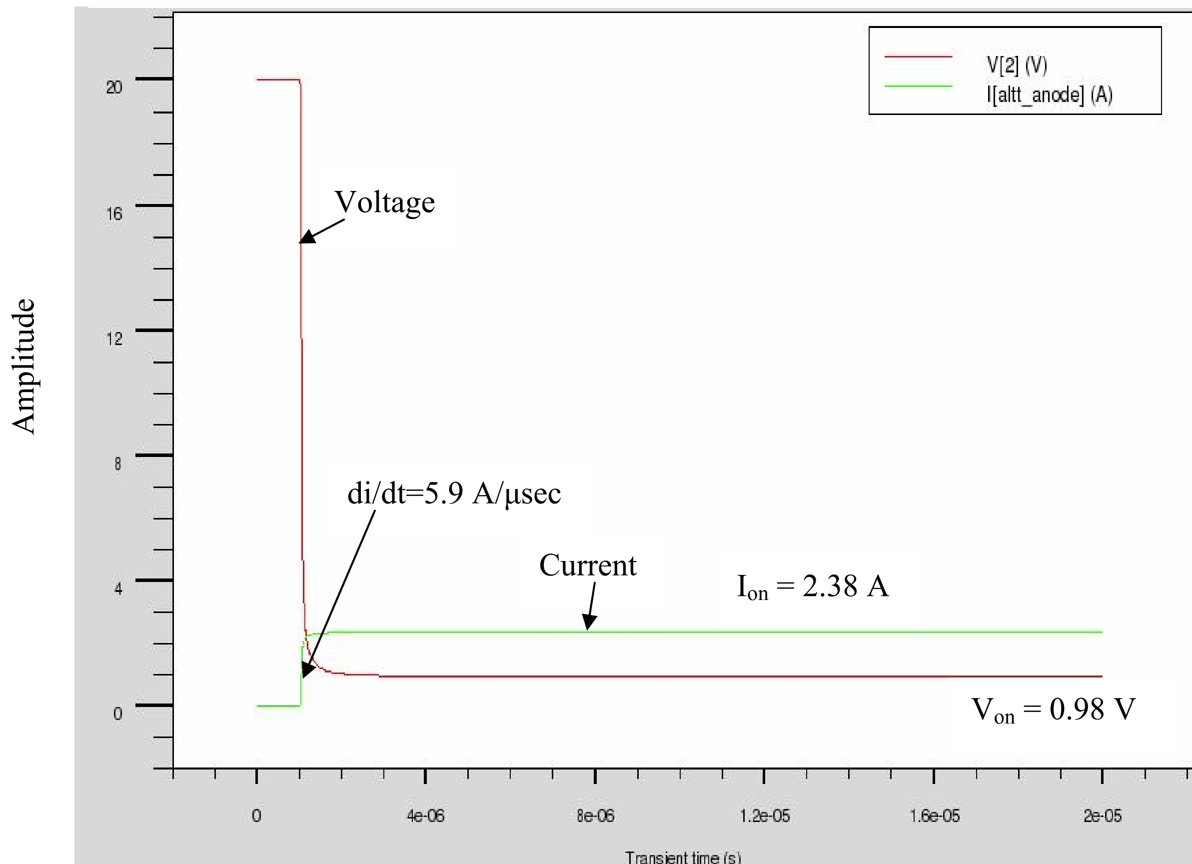

Figure 4.19 Turn-on characteristics of the Model 1 optothyristor.

Model 2

Here V_{dc} is 100 V and R_1 is 8 ohms. Again, the light pulse is ramped to 9 Watts/cm^2 intensity with pulse width of 0.01 µs, and initially there is a delay of 1 µs. The voltage across the thyristor and current through the thyristor were observed. These results are shown in Figure 4.20. The on-state current I_{on} = 12.35 A and the on-state voltage V_{on} = 1.18 V. Also, di/dt = 380 A/µsec.

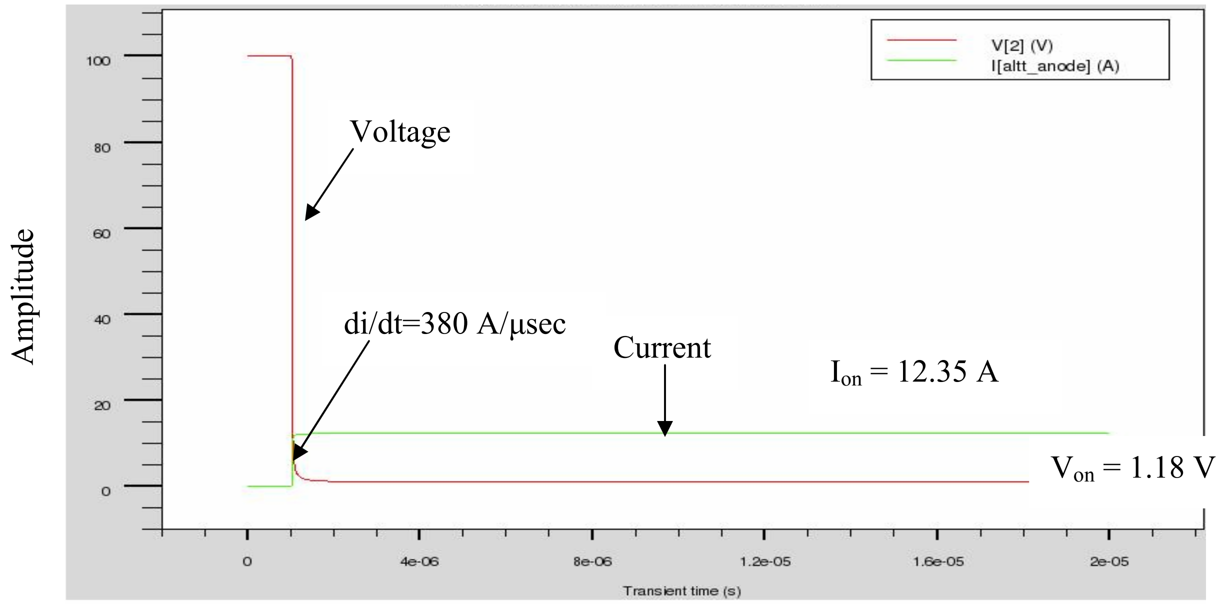

Figure 4.20 Turn-on characteristics of the Model 2 optothyristor

Model 3

Similarly, we followed the same procedure as above with the same light pulse and resistance but with V_{dc} equal to 70 V. The observed results are shown in Figure 4.21.

The on-state current I_{on} = 8.61 A and the on-state voltage V_{on} = 1.11 V. Also, di/dt = 227 A/µsec.

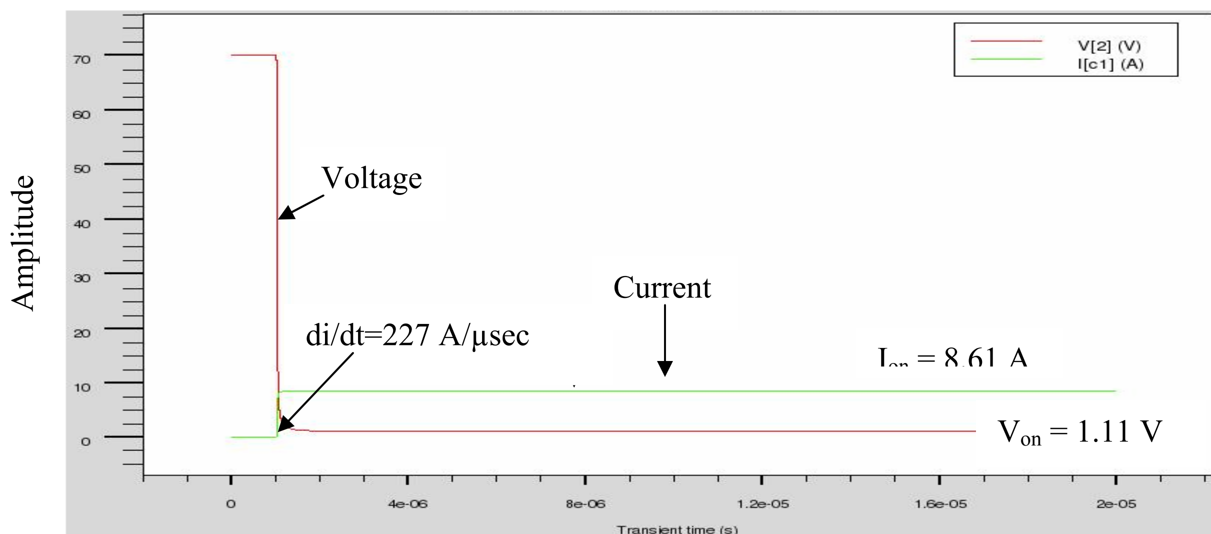

Figure 4.21 Turn-on characteristics of the Model 3 optothyristor.

Model 4

Here, V_{dc} = 100 V. The voltage across and current through the device are as shown in Figure 4.22. The on-state current I_{on} = 12.32 A and the on-state voltage V_{on} = 1.4 V. Also, di/dt = 78 A/µsec.

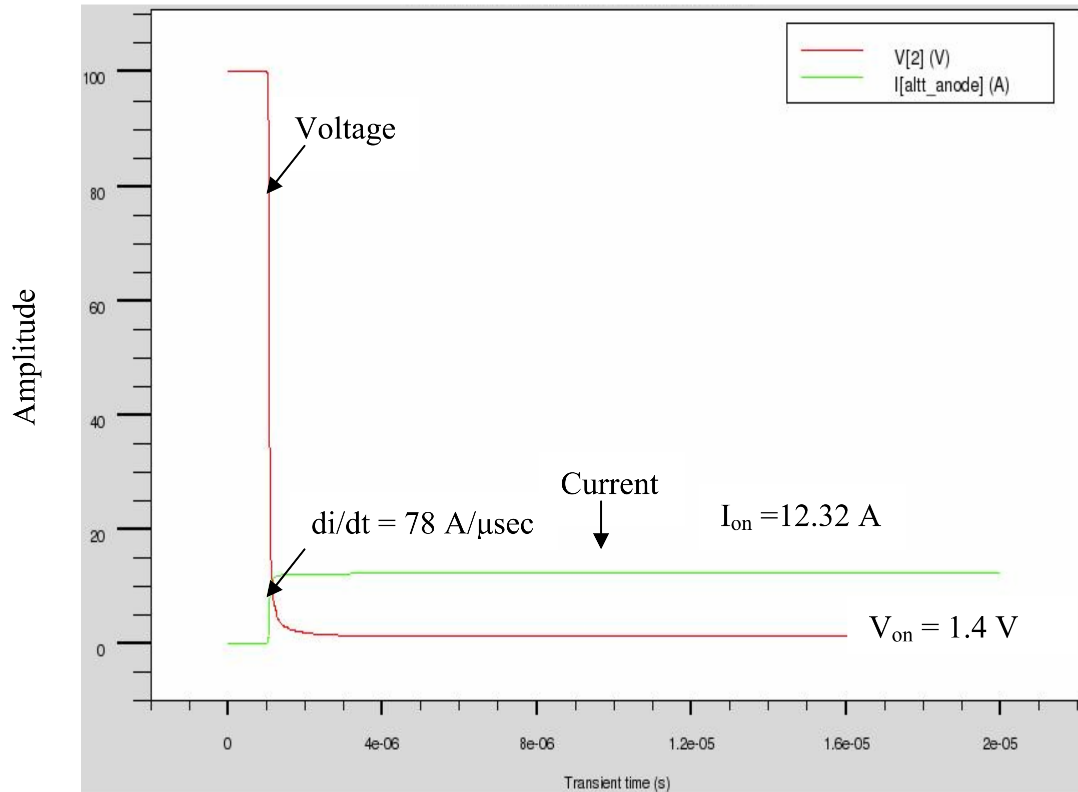

Figure 4.22 Turn-on characteristics of the Model 4 optothyristor.

Model 5

Here V_{dc} = 500 V. The voltage across and current through the device are as shown in Figure 4.23. The on-state current I_{on} = 62.2 A and the on-state voltage V_{on} = 2.42 V. Also, di/dt = 3554.2 A/µsec.

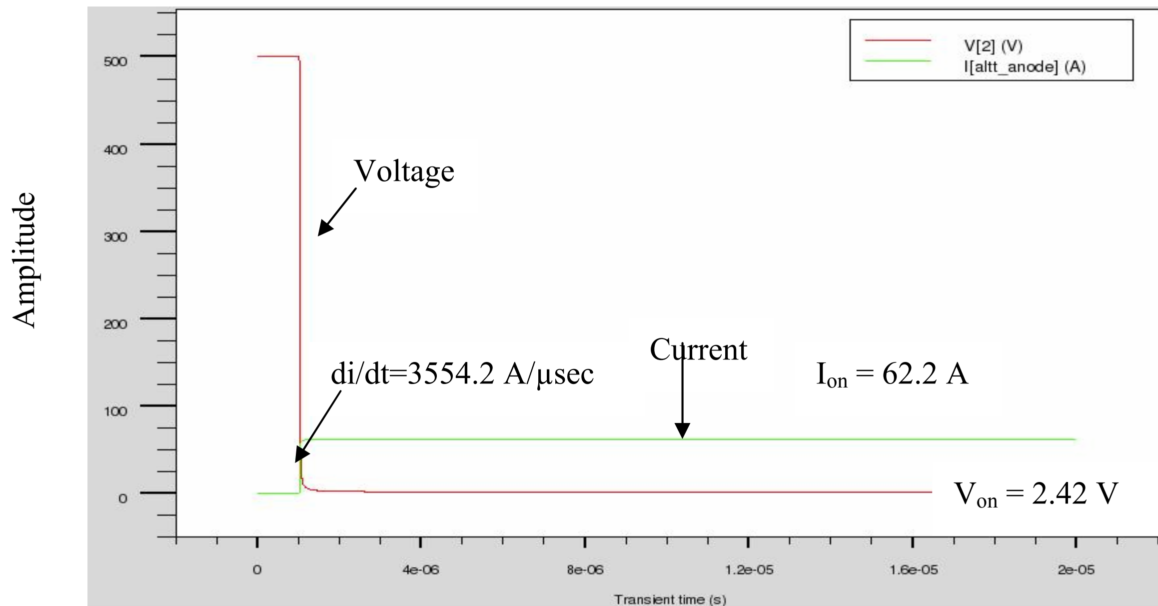

Figure 4.23 Turn-on characteristics of the Model 5 opto-thyristor

Model 6

Here, Vdc is 50 V. The voltage across and current through the device are as shown in Figure 4.24. The on-state current I_{on} = 6.09 A and the on-state voltage V_{on} = 1.26 V. Also, di/dt = 31.43 A/µsec.

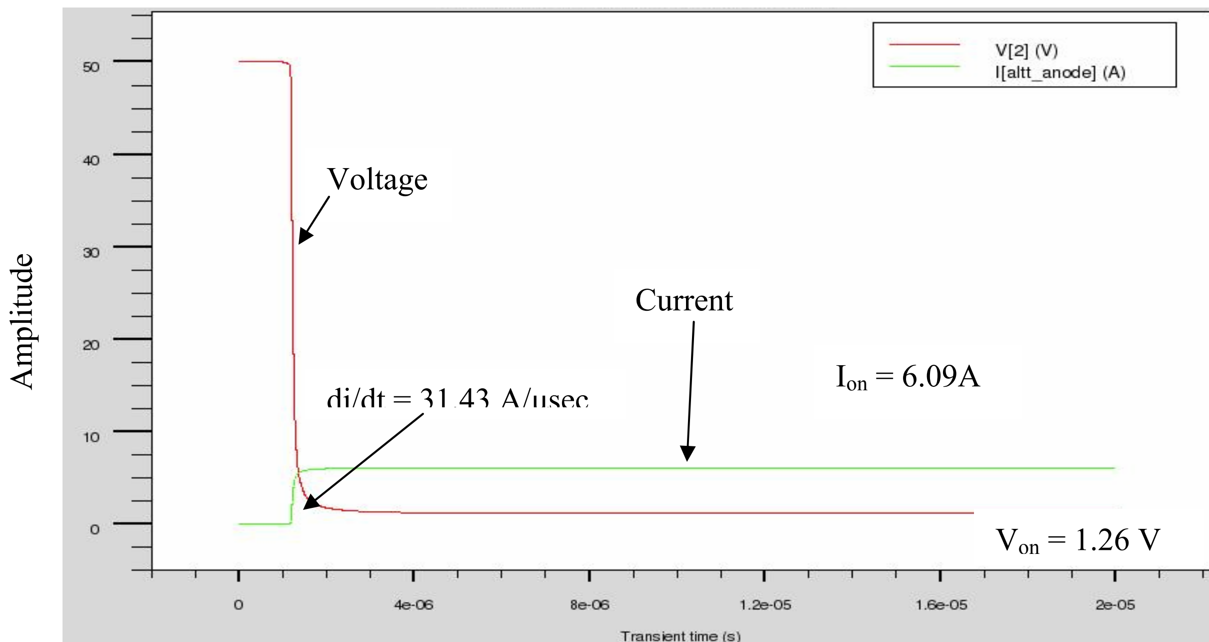

Figure 4.24 Turn-on characteristics of the Model 6 opto-thyristor.
The results are summarized in

Table 4-4and the on-resistance of all the models are calculated using the equation 4.4, which is obtained from Figure 4.18.

$$R_{on} = \frac{V_{dc}}{I_{on}} - R_1 \qquad (4.4)$$

In all these cases the width of the device is 520 µm and the optical energy in the pulse is $9*10^{-8}$ J/cm^2, other light pulse parameters are kept constant.

Model	**V_{dc} V**	**I_{on} A**	**R_1 Ω**	**R_{on} Ω**
Model 1	20	2.38	8	0.403
Model 2	100	12.35	8	0.097
Model 3	70	8.61	8	0.130
Model 4	100	12.32	8	0.116
Model 5	500	62.2	8	0.038
Model 6	50	6.09	8	0.210

Table 4-4 On-state resistance of the all the device models

Having observed the optical turn-on behavior of the opto-thyristor, we varied the intensity of the light pulse to observe its affect on the rise time of the current and the fall time of the voltage. The optical power intensity was set in turn to the three values 9 Watts/cm^2, 90 Watts/cm^2 and 900 Watts/cm^2. The results for Model 2 are as shown in Figure 4.25. We can observe that with more optical intensity the turn-on is faster.

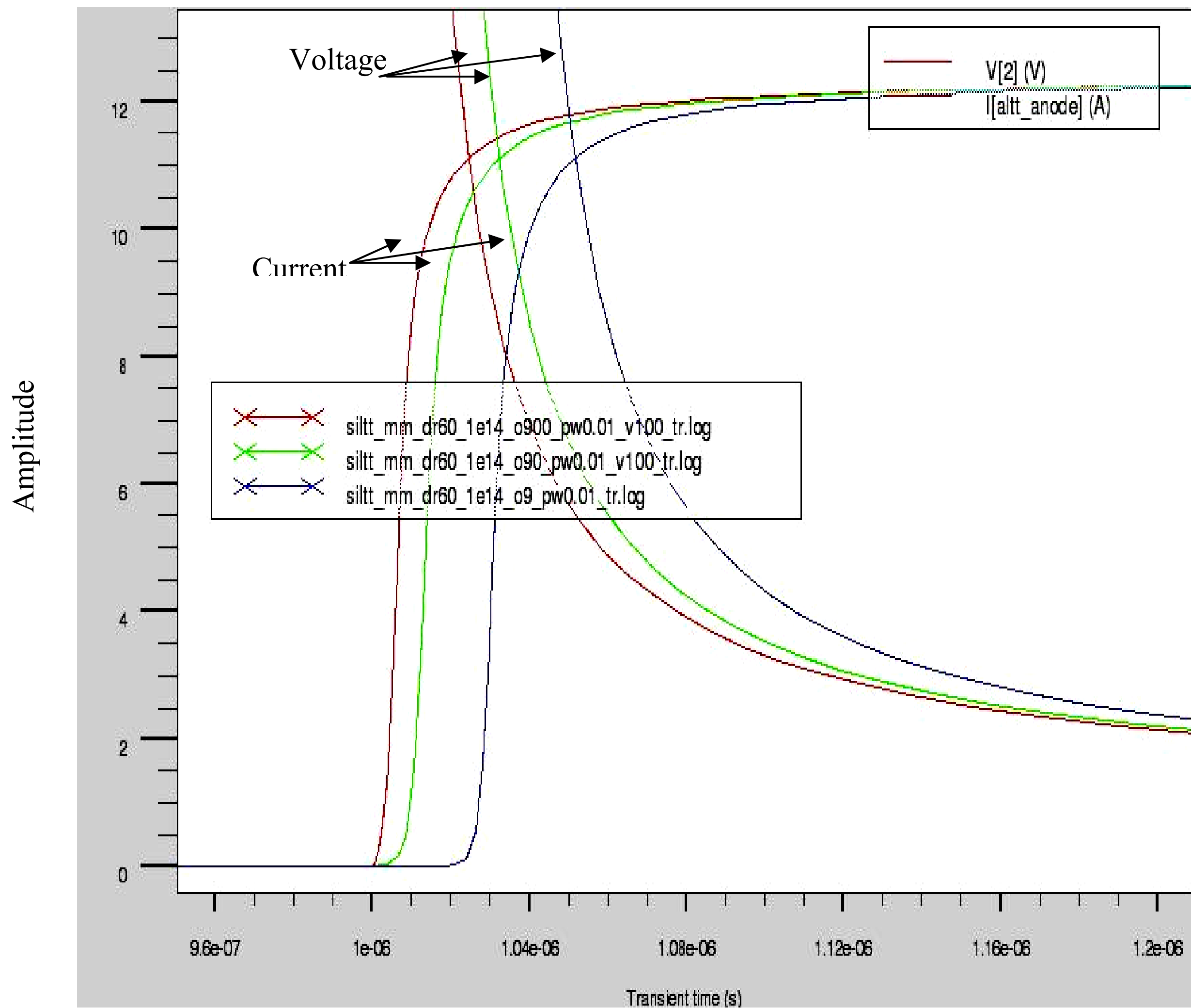

Figure 4.25 Turn-on characteristics of the Model 2 opto-thyristor with optical power intensities 9, 90, 900 Watts/cm^2

Several simulations were then run to determine the minimum amount of optical energy that is required to turn on the opto-thyristor. First, the optical intensity was decreased, and then the pulse width of the light pulse, was decreased. For optical intensity 8 Watts/cm^2 and pulse width 0.01 µs, turn-on occurred but on further reducing either the intensity or the pulse width the device failed to turn-on. Therefore, the minimum optical energy required to turn on the thyristor is E= P*t which equals to $8*10^{-8}$ J/cm^2.

Effect of the on-state resistance on the device performance with respect to third dimension

This study was performed on device Model 2. Here the V_{dc} is 100 V, R_1 is 8 ohms and the optical energy is $9*10^{-8}$ J/cm^2. Figure 4.26 shows the variations in I_{on} and V_{on} as the device width changes. We observe that with increase in width both I_{on} and R_{on} decrease. This is because the opto-thyristors are assumed connected in parallel in Silvaco Mixed mode, on including the third device dimension. The variations are tabulated in Table 4-5.

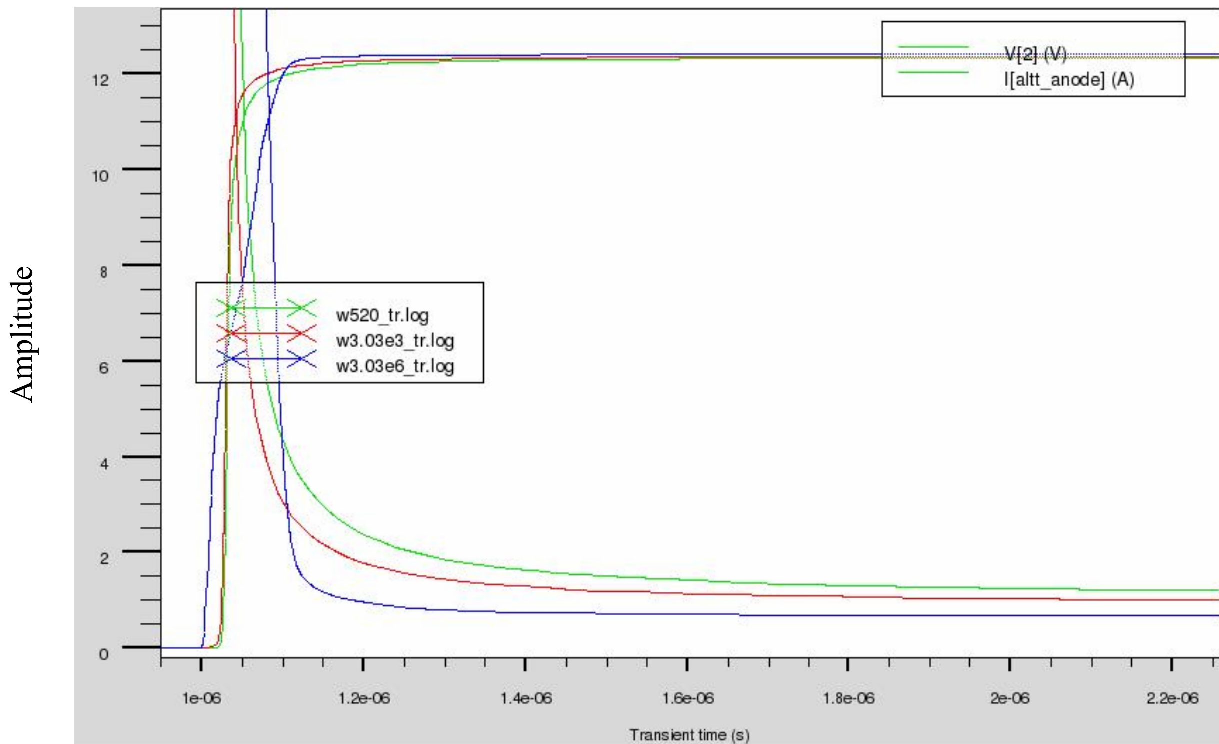

Figure 4.26 Effect of the on-state resistance on the device performance with respect to third dimension (Model 2)

Width µm	I_{on} A	R_{on} Ω
520	12.32	0.116
$3*10^3$	12.35	0.097
$3*10^6$	12.42	0.051

Table 4-5 Variations of on-state resistances with respect to width (Model 2)

4.5 Opto-Thyristor in a Capacitive Discharge Circuit

The modeled opto-thyristor (Model 2) was placed in a capacitive discharge circuit as shown in Figure 4.27. ATLAS Mixed mode was used in this circuit simulation.

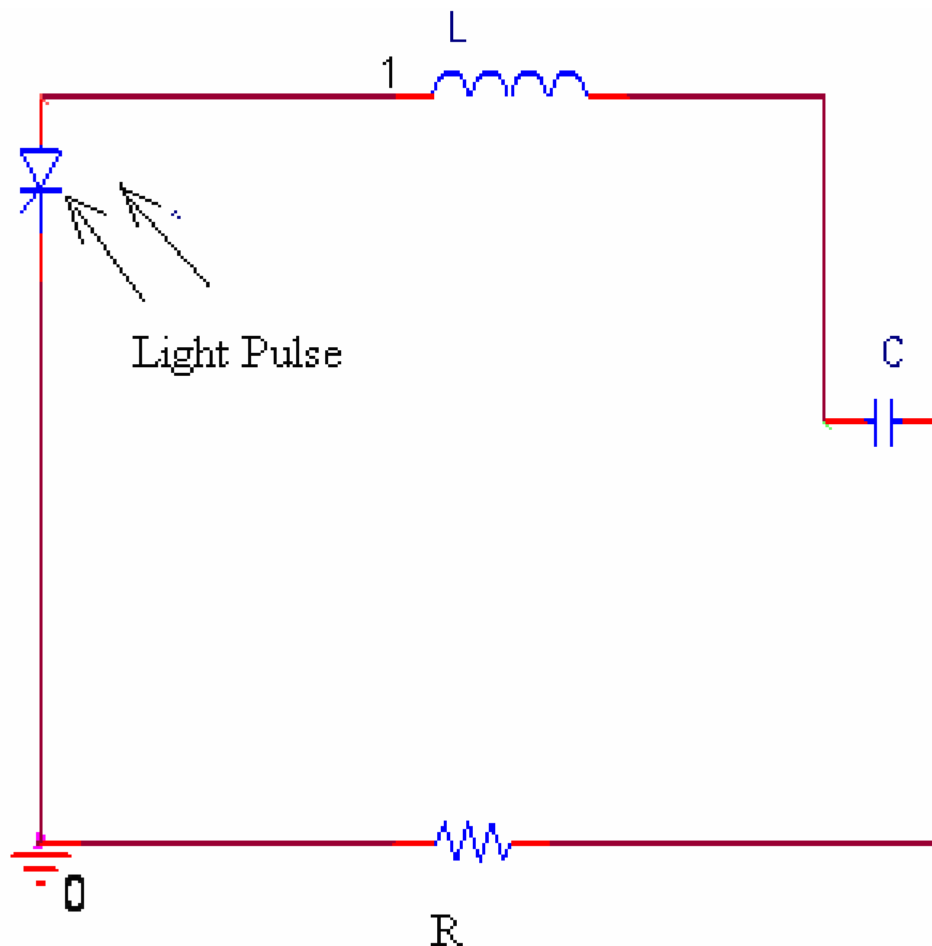

Figure 4.27 Opto-thyristor in capacitive discharge circuit

The response of the circuit was obtained with inductor L = 30 pH, R = 0.01 ohms, and C = 0.2 μF. The initial voltage across the capacitor was 250 V. The width of the device is 520 μm. The resonant frequency of the circuit is found using equation 4.5, as follows

$$f = \frac{1}{2\pi\sqrt{LC}}\ \text{Hz} \tag{4.5}$$

On substituting the values of L and C the calculated resonant frequency was obtained as 65 MHz. Figure 4.28 shows the voltage and current at the anode of the optothyristor. The peak current is found to be 4.372 kA and the di/dt is 437 kA/μs.

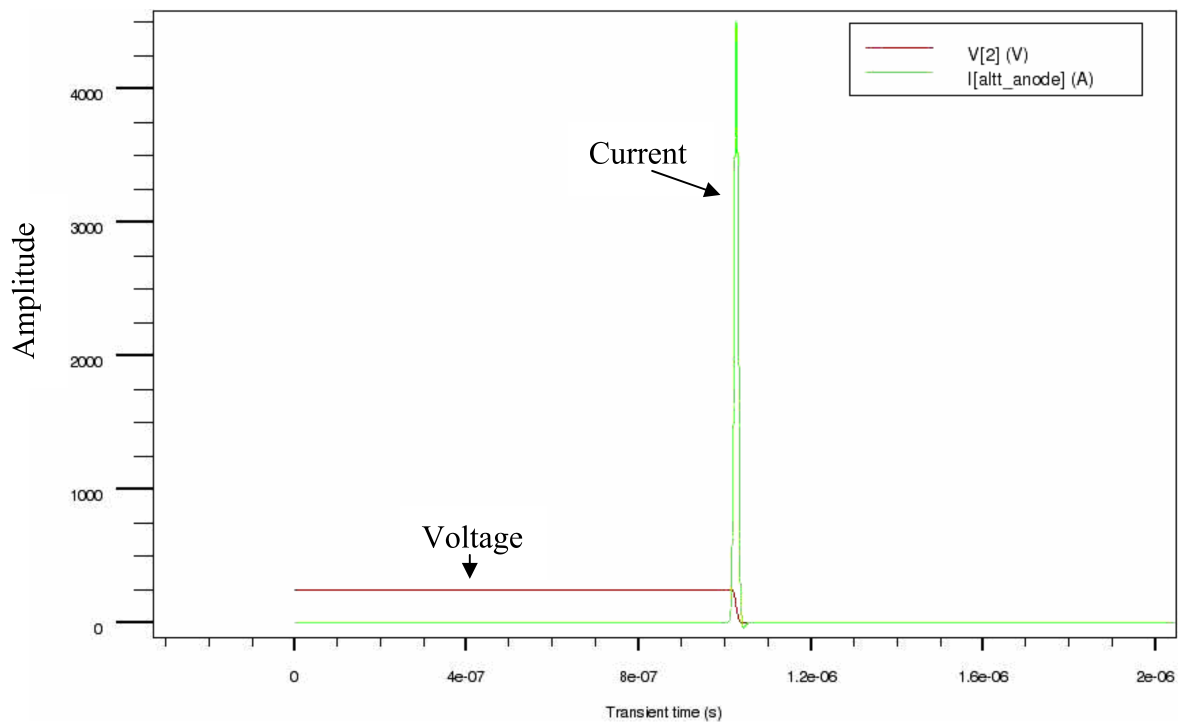

Figure 4.28 Opto-thyristor (Model 2) in capacitive discharge circuit

Figure 4.29 shows the response of the Model 5 opto-thyristor in the capacitive discharge circuit with the same values of L, C, and R. The peak current is 6277 A and di/dt is 3347.73 kA/μs with initial capacitor voltage 500 V. The width of the device is 520 μm.

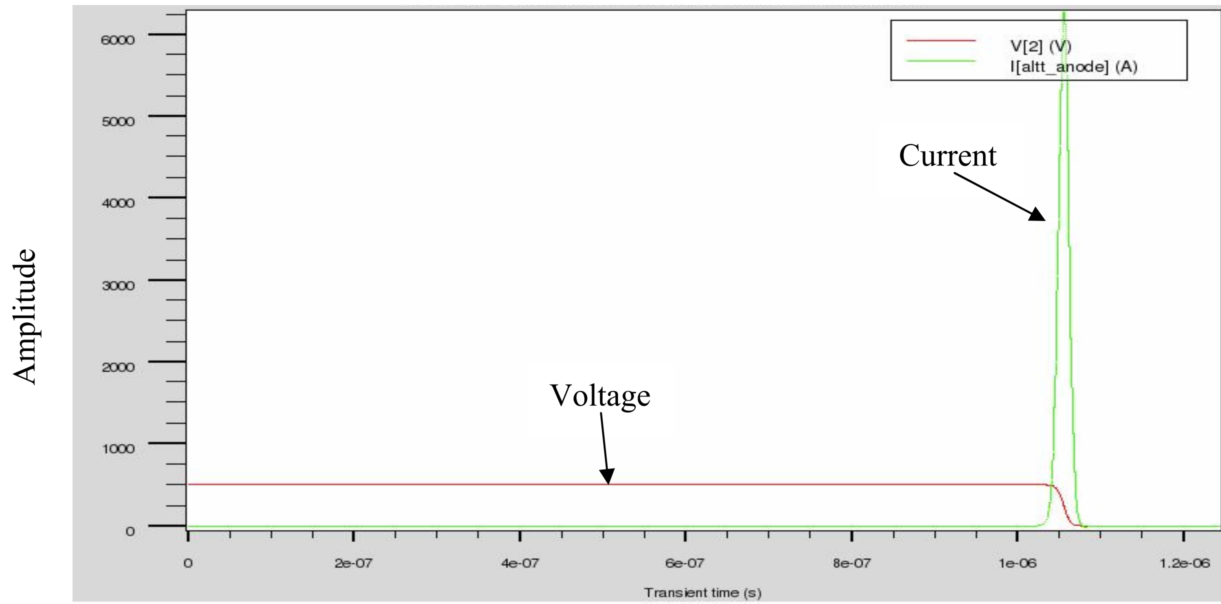

Figure 4.29 Opto-thyristor (Model 5) in capacitor discharge circuit

Figure 4.30 shows the dependence of the parameters di/dt and maximum peak current on the initial capacitor voltage for the Model 2 opto-thyristor, whose width is 520 μm.

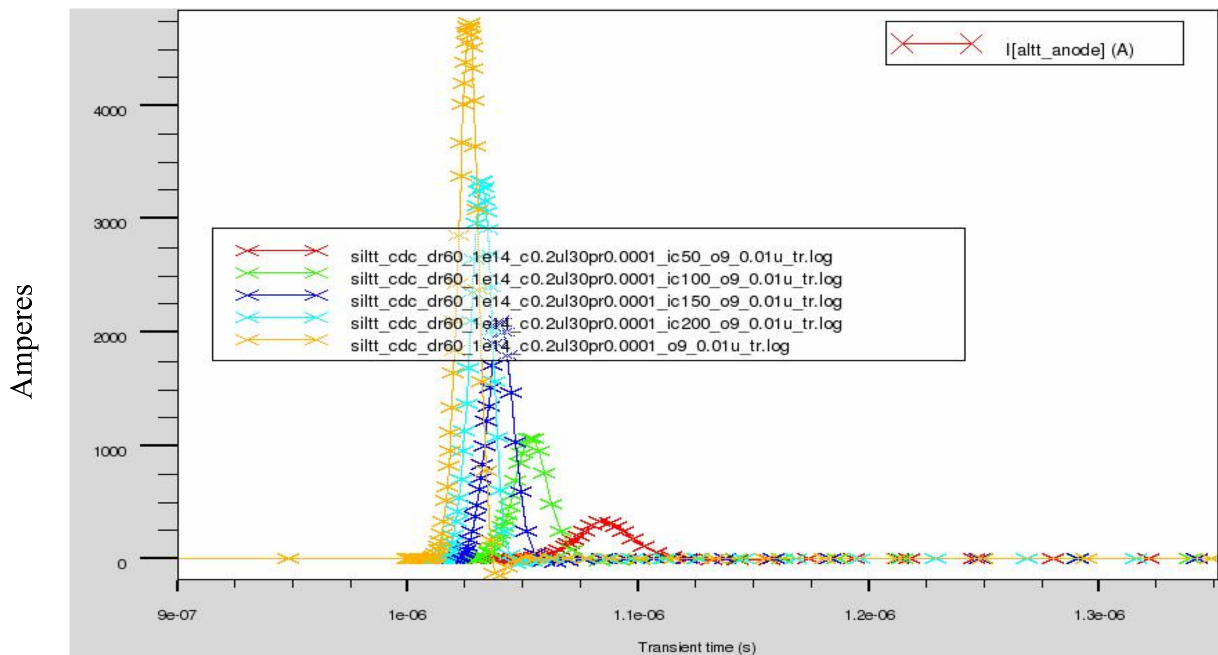

Figure 4.30 Performance of capacitor discharge circuit with initial conditions of 50 V, 100 V, 150 V, 200 V and 250 V on the capacitor (Model 2 opto-thyristor)

Model 2 device performance in a capacitive discharge circuit by varying the width of the device

Here the width of the device is $3.03*10^3$ µm. Figure 4.31 shows the variation of capacitor current for inductor L values 30 pH, 70 pH, 100 pH, 200 pH and 700 pH. Capacitance C is 0.2 µF, R = 0.01 ohms and the optical pulse energy is $9*10^{-8}$ J/cm^2.

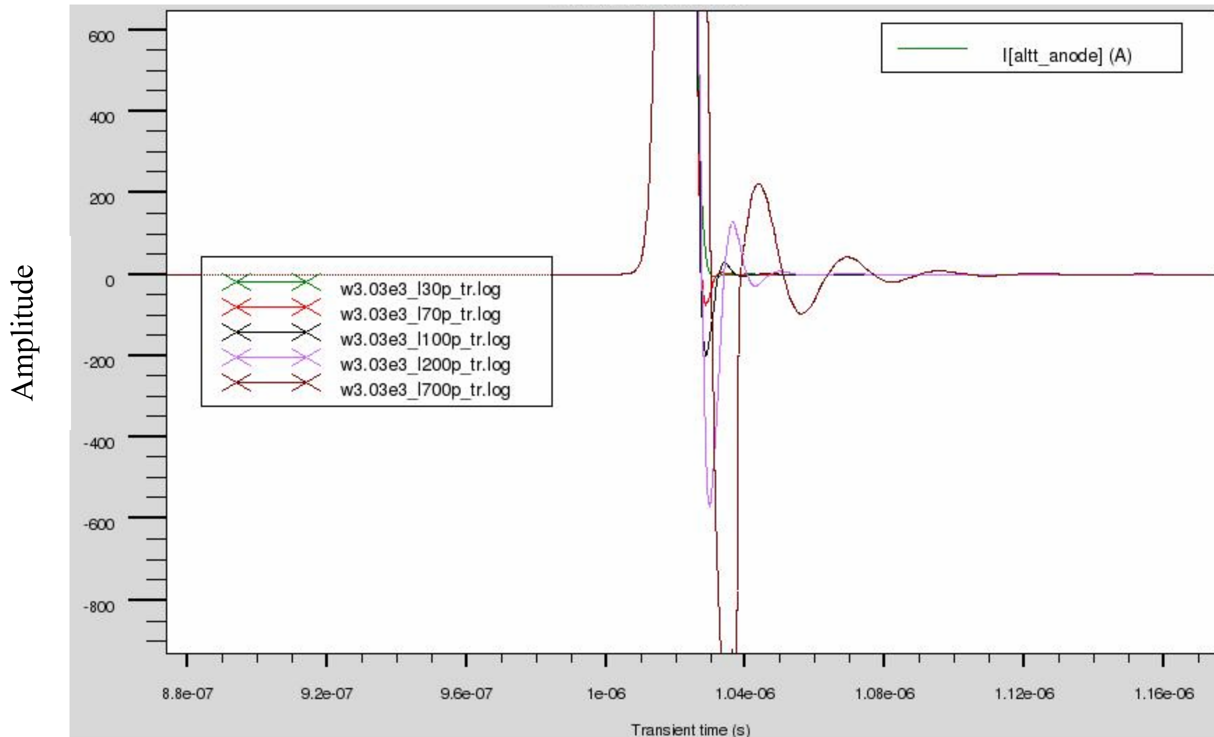

Figure 4.31 Capacitor current variations in Model 2 opto-thyristor whose width=3.03 mm

Next, the simulations were re-run by changing the width to 520 µm. The other parameters are kept the same. Figure 4.32 shows the variation of capacitor current for L values from 30 pH, 70 pH, 100 pH, 200 pH and 700 pH.

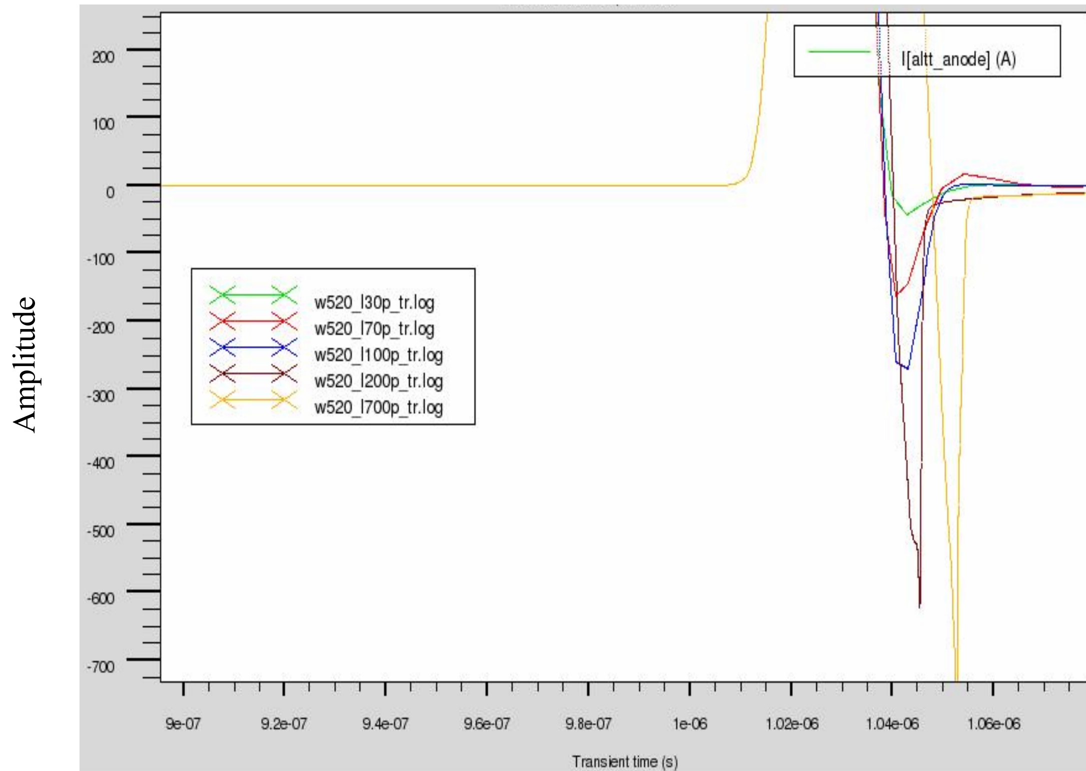

Figure 4.32 Capacitor current variations with inductance in Model 2 opto-thyristor, whose width = 3.03 mm

We observe from Figure 4.31 and Figure 4.32 that by increasing the third device dimension from 520µm to $3.03*10^3$ µm, the ringing was more evident.

To analyse the effect of resistance on the capacitor current

Here, in a Model 2 opto-thyristor, whose width is $3.03*10^3$ µm , L = 700 pH, and C = 0.2 µF, the value of the resistance is set to 0.01, 0.001 and 0.0001 ohms. Figure 4.33 shows the effect on the device performance. The effect of resistance on the circuit performance is very small because from Table 4-5 we see that the on-state resistance of the device is 0.09 ohms. Since the device resistance is higher than the resistance of the circuit, the device resistance is dominating in its performance in the circuit.

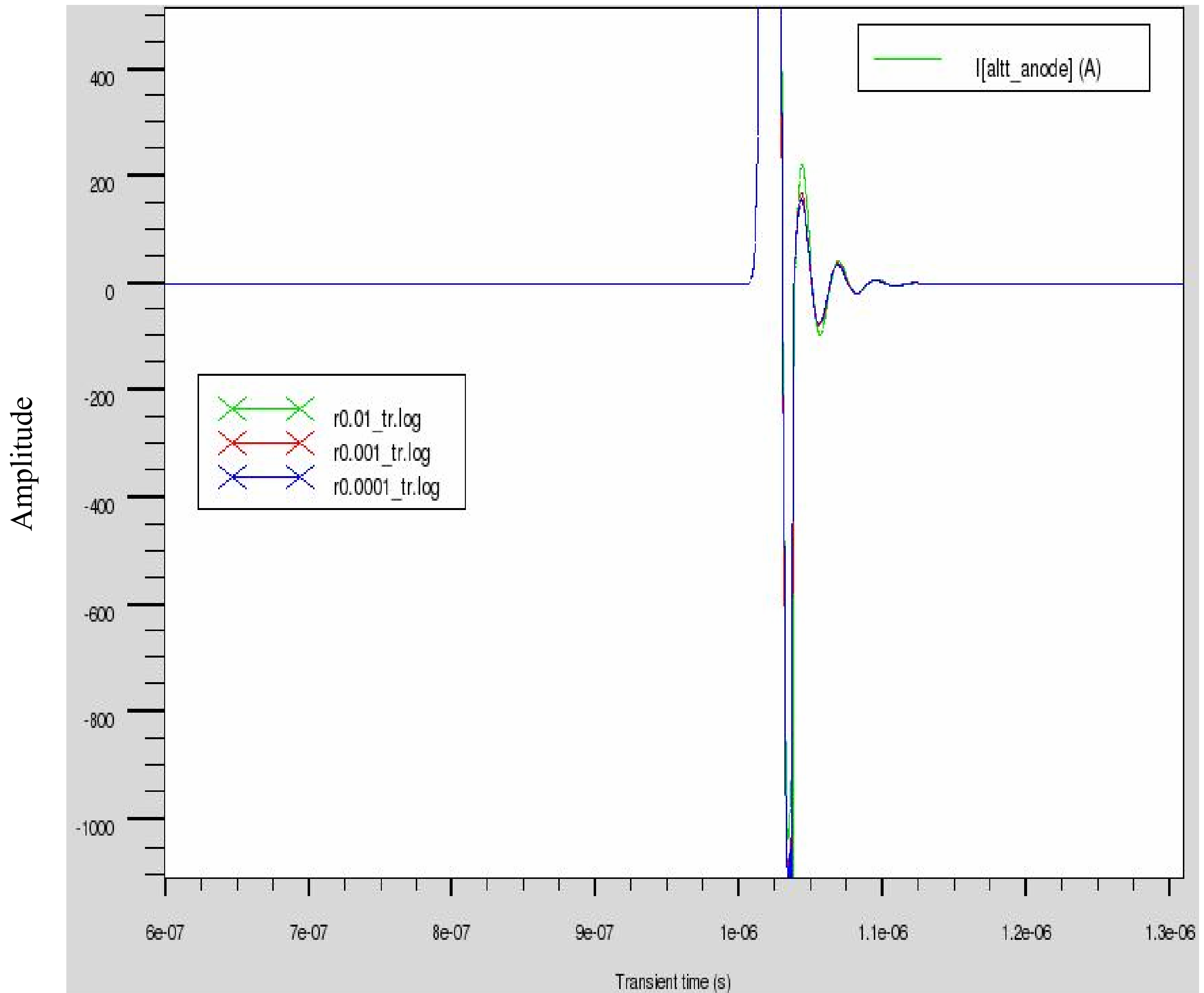

Figure 4.33 Effect of resistance in the capacitior discharge circuit (Model2)

For width $3.03*10^3$ μm, L = 200 pH , C = 0.2 μF, and R=0.01 ohms, Figure 4.34 and Figure 4.35 for Model 2 opto-thyristor show that the peak current is 6793 A, and the di/dt is 905.73 kA/μs, and the resonant frequency of the circuit is 25 MHz, using equation (4.5)

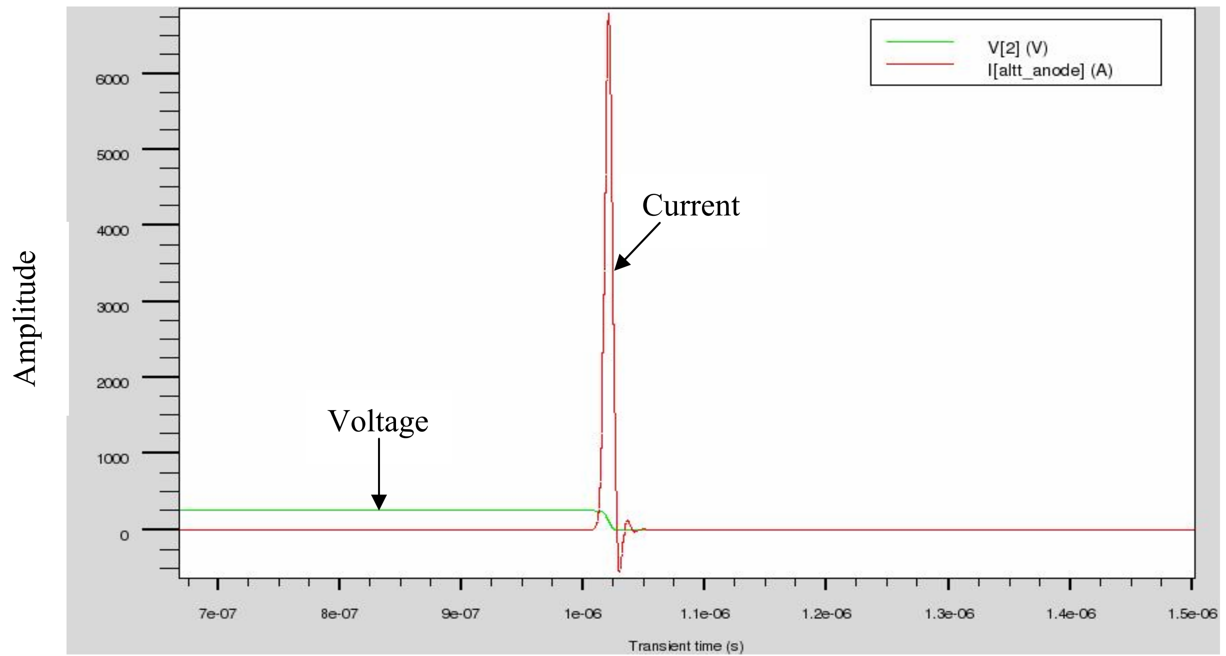

Figure 4.34 Model 2 opto-thyristor with width=3.03 mm

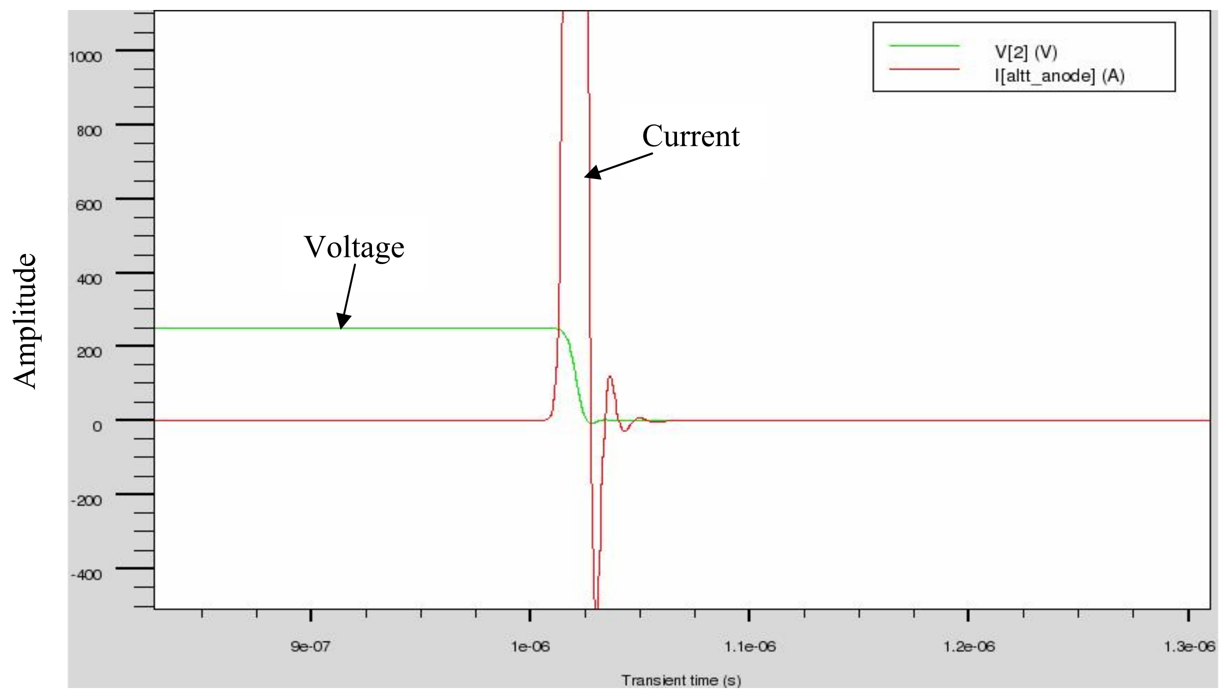

Figure 4.35 Figure 4.34 magnified to observe the ringing

With the same test conditions but with Model 5 opto-thyristor Figure 4.36 shows the effect of capacitor current in capacitor discharge circuit. Here the peak current is 9440 A and di/dt is 1005 kA/μs.

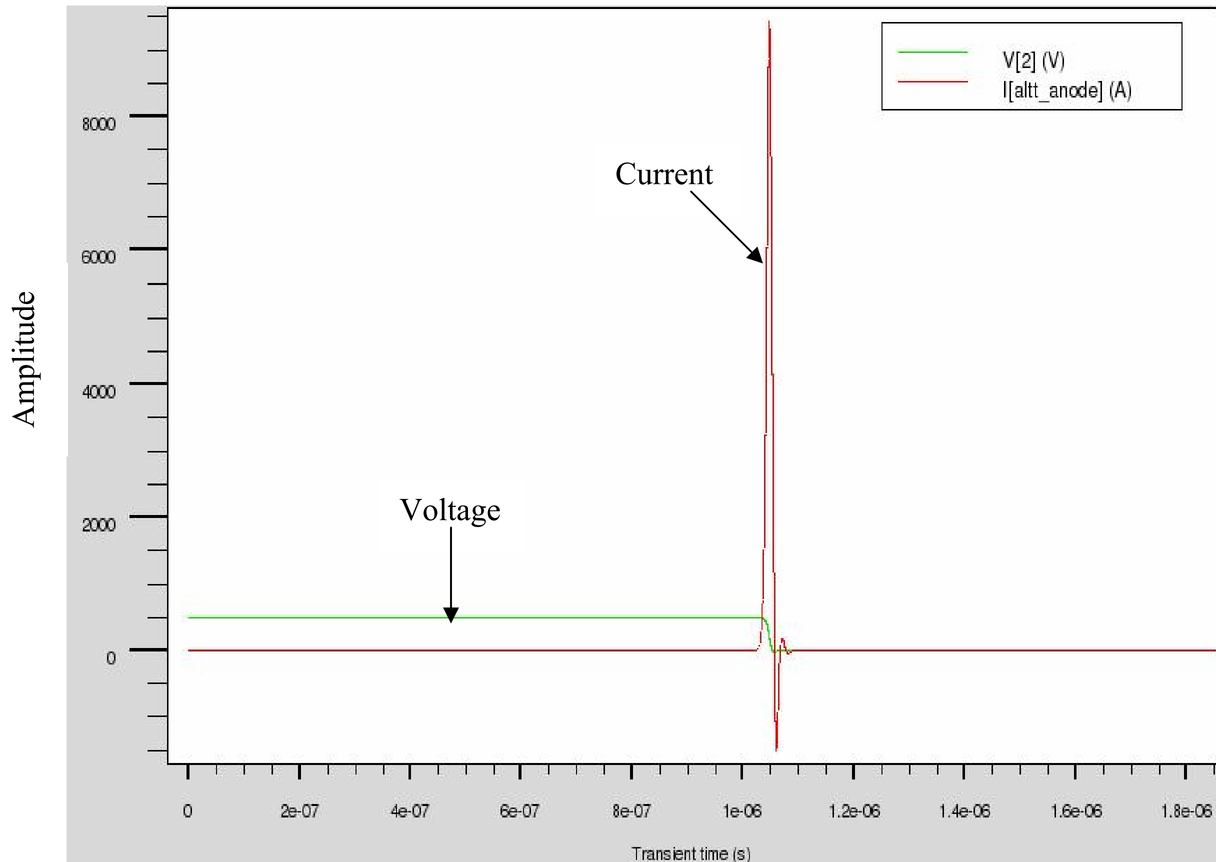

Figure 4.36 Capacitor current and Anode voltage for Model 5 opto-thyristor.

To observe the effects of initial capacitor voltages on the capacitor current

Here a Model 2 opto-thyristor of width 3.03 mm was considered. L = 700 pH, C = 0.2 μF and R = 0.01 ohms. The initial conditions on the capacitor are 250 V, 200 V and 150 V. Figure 4.37 shows the effect on the capacitor current.

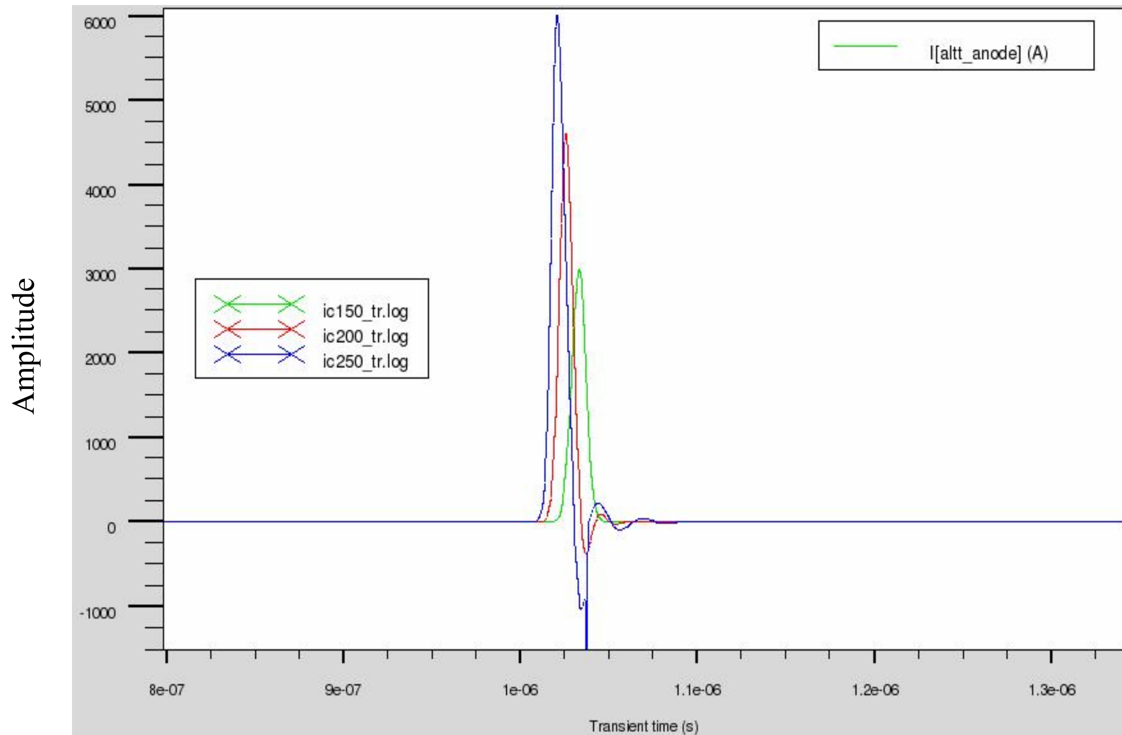

Figure 4.37 Performance of capacitor discharge circuit with initial conditions of 150 V, 200 V and 250 V on the capacitor (Model 2 opto-thyristor with width 3.03 mm)

From the Figure 4.30 and Figure 4.37, we see that the effects of initial capacitor voltages that we observed in PSPICE and the results obtained by using Silvaco ATLAS are quite similar, which suggests that the device modeled behaves as expected.

The quality factor Q of a series RLC circuit is as shown in equation 4.6

$$Q = \frac{1}{R}\sqrt{\frac{L}{C}} \tag{4.6}$$

This Q factor should be greater than 0.5 to observe the oscillation. If this value is greater than 0.5, the system is over-damped and if it is equal to 0.5, it is critically damped [23]. We have chosen all values L, R and C such that we were able to observe the oscillations.

Additional results

For practical values of L = 7 nH, C = 0.2 μF and R = 0.01, Figure 4.38 shows the circuit current for Model 2 opto-thyristor whose width is 520 μm in a capactive discharge circuit. The peak current is 1440 A, the di/dt is 187 kA/μs, and the resonant frequency of the circuit is 4.25 MHz, found using equation (4.5).

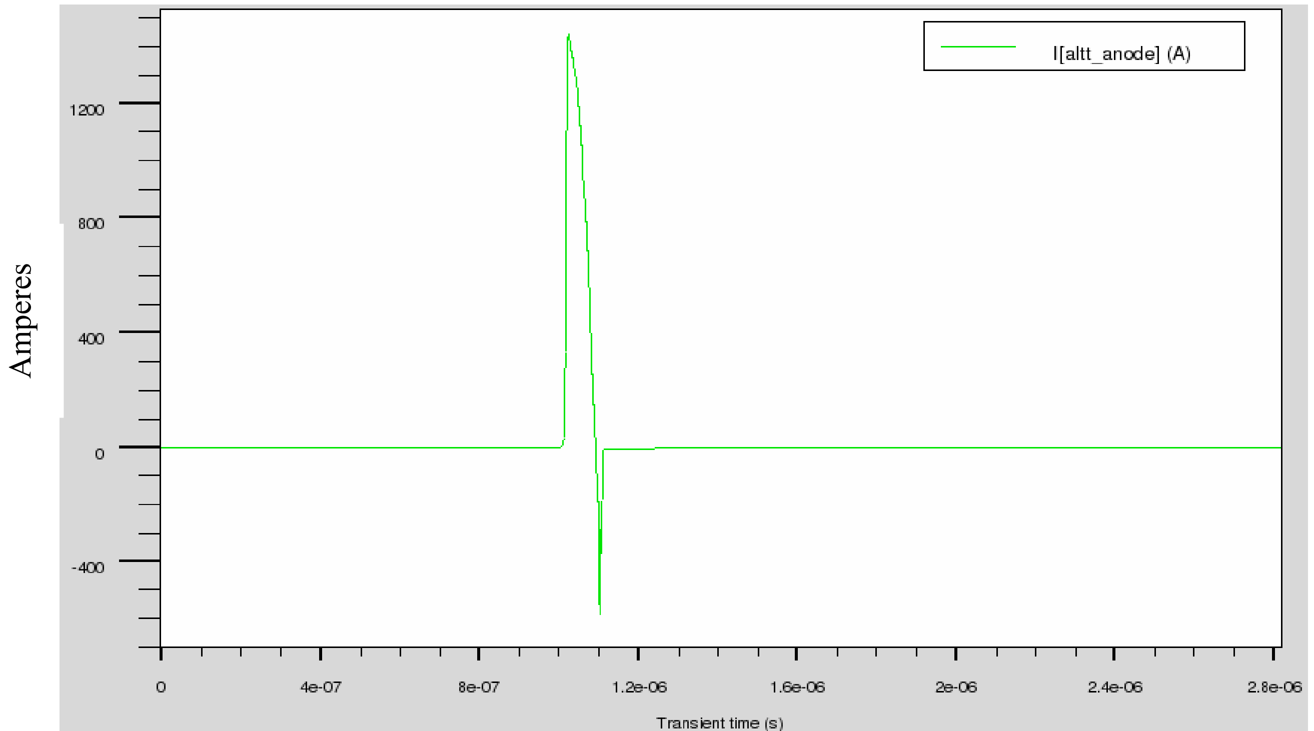

Figure 4.38 Circuit Current for Model 2 opto-thyristor whose width is 520 μm in a capacitive discharge circuit

Using the same values for the circuit elements, device Model 5 opto-thyristor was simulated in a capacitive discharge circuit. Figure 4.39 shows the peak current is 2500 A, and the di/dt is 103.6 kA/μs.

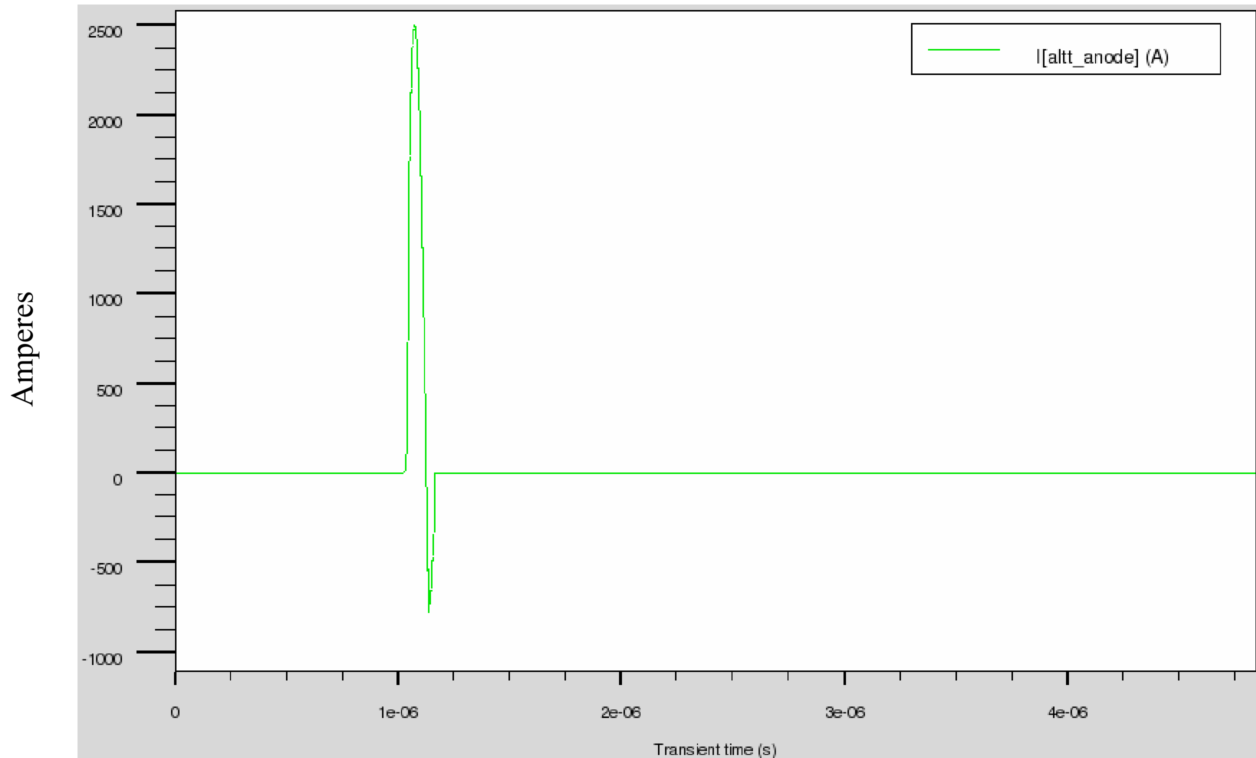

Figure 4.39 Circuit Current for Model 5 opto-thyristor whose width is 520 µm in a capacitive discharge circuit

Finally, we changed the width of the device to 3.03 mm, retaining the circuit element values, L = 7 nH, C = 0.2 µF and R = 0.01 ohms.

Figure 4.40 shows the circuit current and switch voltage for device model 2 opto-thyristor. The peak current is 3944 A, and the di/dt is 664 kA/µs.

Figure 4.41 shows the circuit current and switch voltage for device model 5 opto-thyristor. The peak current is 4000 A, and the di/dt is 266.22 kA/µs.

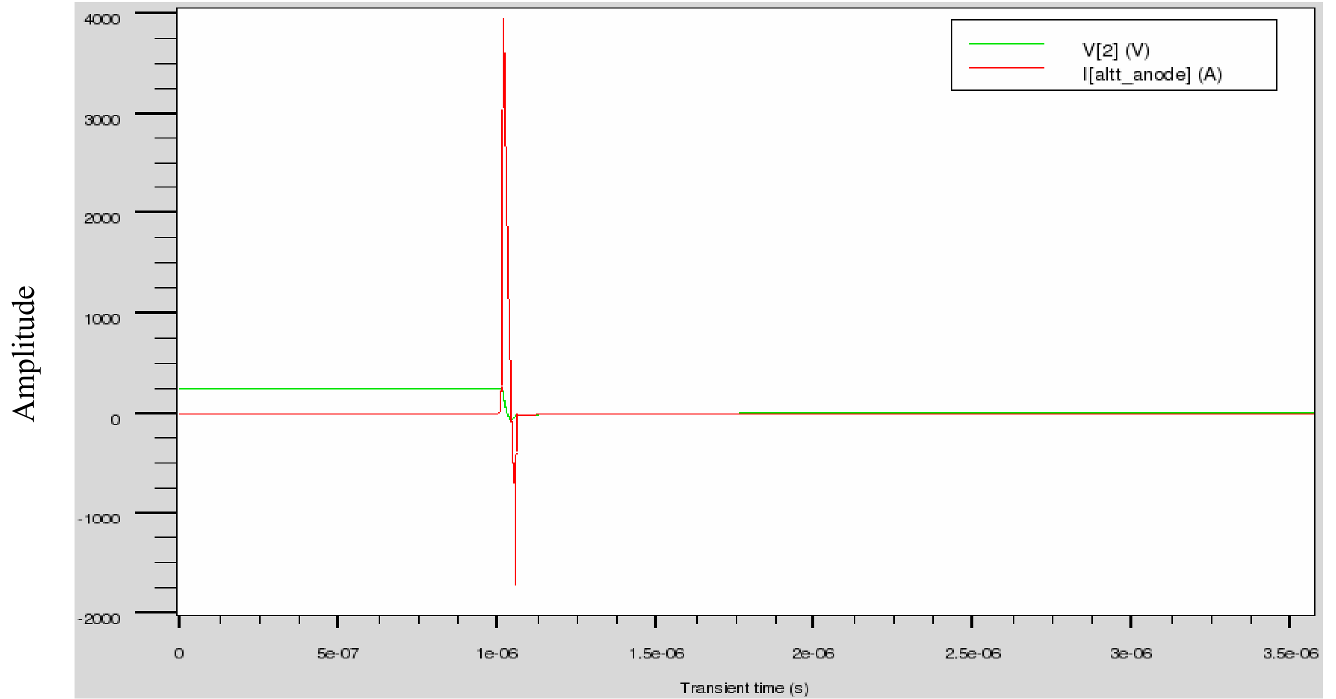

Figure 4.40 Circuit Current and Anode voltage for Model 2 opto-thyristor whose width is 3.03 mm in a capacitive discharge circuit

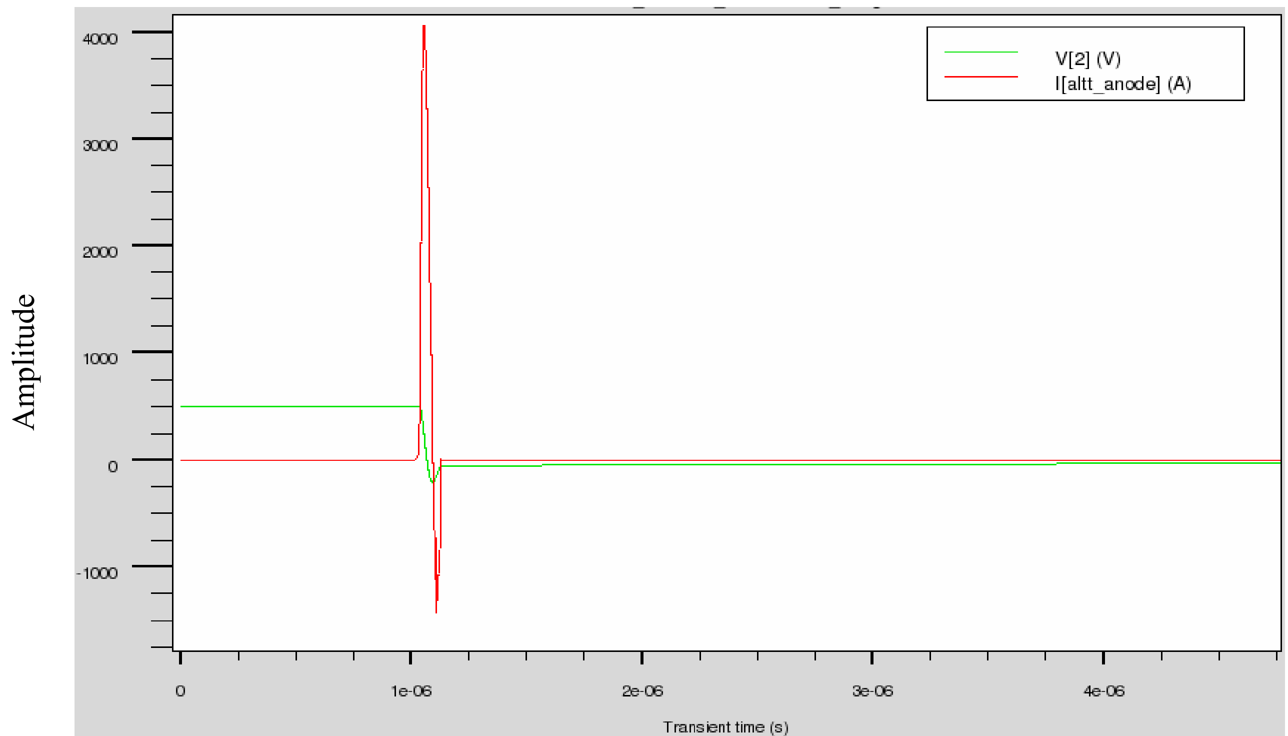

Figure 4.41 Circuit Current and Anode voltage for Model 5 opto-thyristor whose width is 3.03 mm in a capacitive discharge circuit

CHAPTER 5: SUMMARY, FUTURE WORK AND CONCLUSION

5.1 Summary

In summary, we have designed a silicon opto-thyristor using an amplifying gate structure for capacitive discharge circuit applications using Silvaco ATLAS. The Silvaco ATLAS simulator, which takes into account the device physics, was also used to test the opto-thyristor performance in a capacitor discharge circuit.

Having tested the opto-thyristor dark IV characteristics we could determine the blocking voltages of the opto-thyristor. By varying the drift region concentration and drift region dimension we observed that break-over voltages are highly dependent on these parameters.

Next, the transient turn-on for this device was tested to determine the minimum optical power, intensity, and energy required for its turn-on. Also we observed the effect of varying optical intensity on the turn-on time. The higher the optical intensity the faster was the turn-on of the device. On considering the third dimension of the device we observed the effect of the on-state resistance on device performance.

Finally, the device was simulated in a capacitor discharge circuit. Since this is a series RLC oscillator circuit the quality factor should be greater than 0.5 to observe

oscillations. We have chosen the values for L, R and C to be able to observe oscillations. In order to have a good Q-factor the resistance should be as small as possible. We could observe the effect on capacitor current due to the variation of the resistance of the circuit. Also we observed that large oscillations are caused by increasing the third dimension of the device.

From the device models we have observed the following best performances: Model 2 opto-thyristor with width 3.03 mm had a peak current of 3944 A and di/dt of 664 kA/μs and Model 5 opto-thyristor width 3.03 mm had a peak current of 4060 A and di/dt of 266.22 kA/μs, when placed in a capacitive discharge circuit of L = 7 nH, C = 0.2 μF, R = 0.01 ohms.

5.2 Future Work

Follow-on work should include continuing the simulations by modifying the amplifying gate dimensions and concentrations to observe its effect on di/dt. Also layer by layer dimensions and concentrations could be varied to observe their effects on the performance of the capacitive discharge circuit.

Silicon offers multiple advantages to power electronic designers, but at the same time suffers from limitations that are inherent to silicon material properties, such as low bandgap energy, low thermal conductivity, and switching frequency limitations. Wide bandgap semiconductors, such as silicon carbide (SiC) and gallium nitride (GaN), provide higher breakdown electric field and higher thermal conductivity than silicon. SiC is the most advanced material of the two and, hence, is the subject of attention from power electronics and systems designers. Opto-thyristors made of SiC should be studied.

5.3 Conclusion

We designed an opto-thyristor using Silvaco ATLAS. Later using Silvaco Atlas Mixed Mode simulator the silicon opto-thyristor was simulated in a capacitive discharge circuit. Dependence of the drift region's concentration and doping on the device performance was studied. Tabulated are the devices which exhibited good performance in a capacitive discharge circuit.

Device	Width	Inductor (H)	Blocking voltage (V)	Peak Current (A)	di/dt (kA/µs)
Model 2	520 µm	7 n	274.5	1440	187
Model 5	520 µm	7 n	522	2500	103.6
Model 2	3.03 mm	7 n	274.5	3944	664
Model 5	3.03 mm	7 n	522	4060	266.22

APPENDIX

```
# Opto-thyristor in Capacitive Discharge Circuit

go atlas

#
# Mesh Specification
#
mesh
x.mesh loc=0.0   spac=12.0
x.mesh loc=100   spac=2.0
x.mesh loc=150  spac=5.0
x.mesh loc=300   spac=2.0
x.mesh loc=520   spac=13.0

y.mesh loc=0.0   spac=5.0
y.mesh loc=20.0  spac=0.4
y.mesh loc=24.0  spac=2.0
y.mesh loc=40.0  spac=10.0
y.mesh loc=90.0 spac=5.0

#
# Region Specification
#
region     num=1 silicon   x.min=0 x.max=520 y.min=0 y.max=20
region     num=2 silicon   x.min=0 x.max=520 y.min=20 y.max=90
region     num=3 insulator x.min=0 x.max=520 y.max=0  material=vacuum

#
# 1- Optical gate; 2- Amplifying gate; 3-Anode; 4- Cathode
#
elec       num=1 x.min=100 x.max=122.5  name=ogate
elec       num=2 x.min=147.5 x.max=287  name=gate
elec       num=3 bottom name=anode
elec       num=4 x.min=312 x.max=510  name=cathode

#
#  Impurity profile
#
doping reg=1 uniform conc=2.e15    p.type
doping reg=1 gauss conc=1.e19 n.type peak=0  junc=15 x.l=0 x.r=115 rat=0.1
doping reg=1 gauss conc=1.e19 n.type peak=0  junc=15 x.l=140  x.r=284 rat=0.1
doping reg=1 gauss conc=1.e19 n.type peak=0  junc=10 x.l=312 x.r=510 rat=0.1
```

```
doping reg=2 uniform conc=1.e14    n.type
doping reg=2 gauss conc=1.e19 p.type peak=90 junc=80 x.l=0 x.r=520 rat=0.1


contact name =anode
contact name=cathode

save outfile=optothyristor.str
tonyplot optothyristor.str -set optothyristor.set


go atlas
.begin
#
#   Opto-thyristor in Capacitive Discharge Circuit
#
#    Part 1: Steady state solution
#
#

altt 1=cathode 2=anode   width=3.03e3 infile= optothyristor.str

l1 1 3 7n
c1 2 0 200n
r1 3  0 .01
O1 1 9

.ic v(2)=250  v(1)=0. v(3)=0.
.numeric toldc=6.e-6 vchange=1.1 imaxdc=300
.save outfile= optothyristor
.options m2ln relpot print debug
.end

material device=altt reg=1 taun0=2.4e-6 taup0=0.6e-6
material device=altt reg=2 taun0=2.4e-6 taup0=0.6e-6
models device=altt reg=1 analytic fldmob srh auger bgn
models device=altt reg=2 analytic fldmob srh auger bgn
impact device=altt selb reg=1
impact device=altt selb reg=2

go atlas
.begin
#
#    Part 1: Transient solution
#
altt 1=cathode 2=anode   width=3.03e3 infile= optothyristor.str
```

```
l1  1 3 7n
c1 2 0 200n
r1  3  0 .01
O1 1 0 pulse 0 9 1us 1ns 1ns 0.01us 20us

.ic  v(2)=250.  v(1)=0  v(3)=0
.numeric lte=100. vchange=1.1 dtmin=1.e-18 toltr=1.e-3
.tran 2.e-17 20us
.load infile= optothyristor
.log outfile= optothyristor
.options print relpot
.end


material device=altt reg=1 taun0=2.4e-6 taup0=0.6e-6
material device=altt reg=2 taun0=2.4e-6 taup0=0.6e-6
models device=altt reg=1 analytic fldmob srh auger bgn
models device=altt reg=2 analytic fldmob srh auger bgn
impact device=altt selb reg=1
impact device=altt selb reg=2
method quasi

beam num=1 x.origin=10.0 y.origin=-10.0 angle=90.0 wavelength=.9 x.min=-10
x.max=90


go atlas
tonyplot optothyristor_tr.log -set optothyristor.set
quit
```

REFERENCES

1. T.F. Podlesak et al., “Solid state switches for electric gun applications,” IEEE Trans. Magnetics, pp. 491-494, January 1997.

2. T.F. Podlesak et al., “Demonstration of compact solid-state opening and closing switch utilizing GTOs in series,” IEEE Trans. Electron Devices, pp.706-711, April 1991.

3. S. Schneider et al., “Reverse switching dynistor pulsers,” IEEE Trans. Plasma Science, pp. 1520-1523, October 2000.

4. T.F. Podlesak et al., “Single-shot and burst repetitive operation of involute gate symmetric thyristors,” IEEE Trans. Plasma Science, pp. 1528-1532, October 2000.

5. E.Ramezani et.al., “High peak current ,high di/dt thyristors for closing Switch Applications” IEEE Conference on Pulse Power, pp. 680-683, June 1993.

6. V.A.K. Temple et al., “High-power dual amplifying gate light triggered thyristors,” IEEE Trans. Electron Devices, pp. 893-898, August 1976.

7. V.A.K. Temple, “Comparison of light triggered and electrically triggered thyristor turn on,” IEEE Trans. Electron Devices, pp. 860-865, July 1981.

8. M. Watanabe et al., “A 115-mm, 6-kV, 2500-A light triggered thyristor,” IEEE Trans. Electron Devices, pp. 285-289, January 1990.

9. R.J. Lis et al., “An LPE grown InP based optothyristor for power switching applications,” IEEE Trans. Electron Devices, pp. 809-813, May 1994.

10. J.H. Zhao et al., “A novel high power optothyristor based on AlGaAs/GaAs for pulsed power switching applications,” IEEE Trans. Electron Devices, pp.819-825, May 1994.

11. D.M.Giorgi et.al .,“A High Current ,High di/dt,Light Activated Thyristor,”

IEEE Symposium on Electromagnetic Launch Technology, pp. 186-190, 2004.

12. H.G. Wisken et al., “Light activated semiconductors for ETC pulsed power applications,” pp. 403-405, January 2001.

13. Th.H.G.G. Weise et al., “Performance spectrum of optical triggered thyristor switches for electric weapon systems,” IEEE Symposium on Electromagnetic Launch Technology, pp.252-254, 2004.

14. V.A.K. Temple, “MOS-controlled thyristors, a new class of power devices,” IEEE Trans. Electron Devices, pp. 1609-1618, October 1986.

15. J.H. Hur et al., “GaAs Opto-Thyristor for Pulsed Power Applications,” IEEE Trans. Electron Devices, pp. 325-329, June 1990.

16. Silvaco Int., Atlas User’s Manual [online], Available: www.silvaco.com

17. D.Silber et al., “Progress in Light Activated Thyristors,” IEEE Trans. Electron Devices , pp. 899-904, August 1976.

18. J.J.L. Weaver et at., “Development of a Thyristor Valve for H.D.V.C. Transmission,” IEE Conf. Power Thyristors and their Applications, pp. 339-346, May 1969.

19. T.Horigome et al., “A 100 kV Thyristor Converter for High Voltage DC Transmission,” IEEE Trans. Electron Devices, pp. 809-815, June 1970.

20. I.Boban et al., “Design and Testing if the CABORA BASSA Thyristor valves,” IEEE Trans. Power Apparatus and Systems, pp 1061-1071, June 1975.

21. D. Silber et al., “Improved Gate Concept for Light Activated Power Thyristors,” in 1975 IEDM Conf. Rec., pp.371-374.

22. S. M. Sze, “Physics of Semiconductor Device 2nd Edition,” pp.194

23. Q-factor[online], Available: http://en.wikipedia.org/wiki/Q-factor